Master's Thesis

Development of a Surface Magneto-Optic Kerr Effect Setup

September 2nd 2010-July 1st 2011

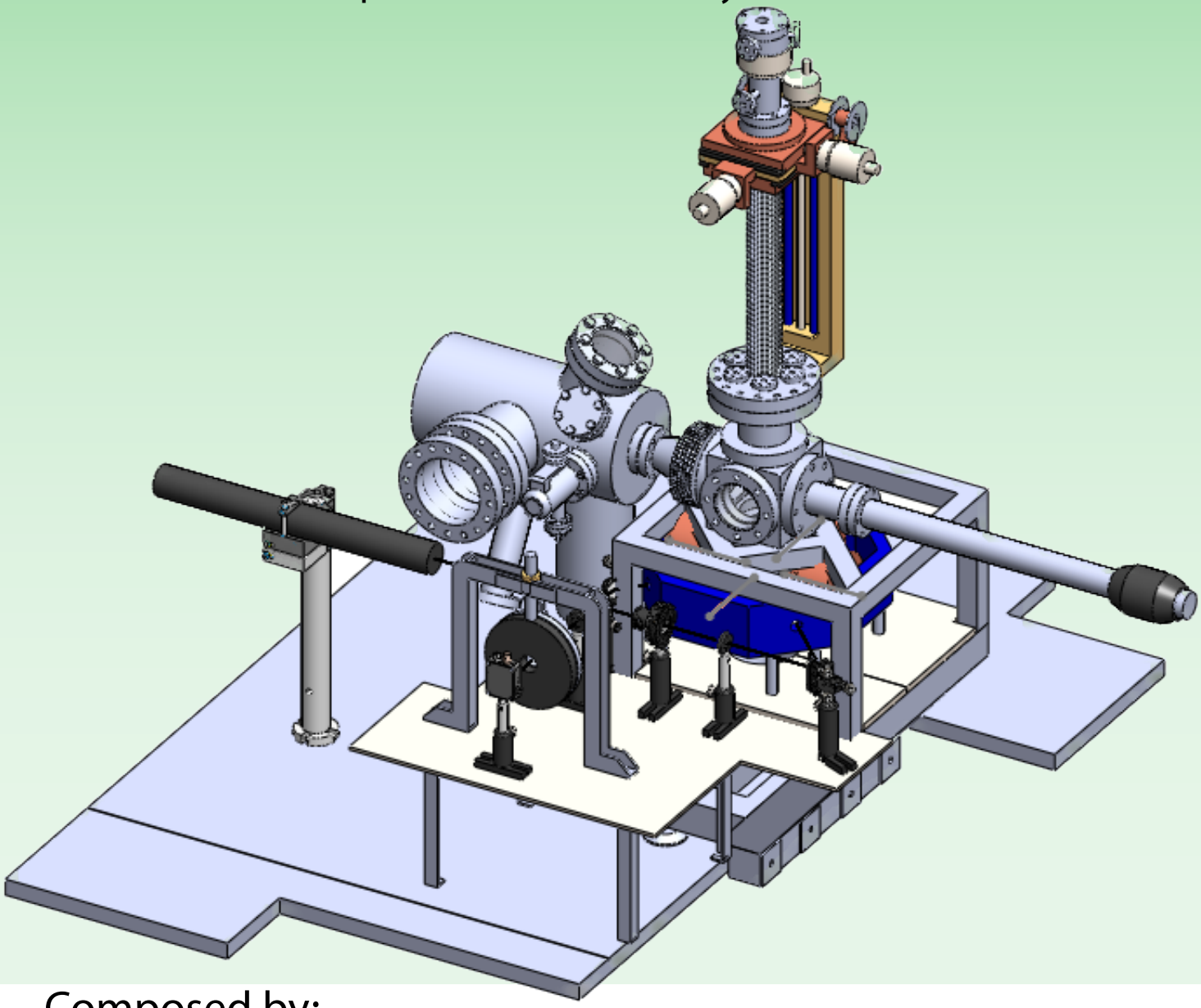

Composed by:
Rasmus Bjørn &
Kristian Bonderup Pedersen

Supervisor:
Associate Professor Lars Diekhöner

Department of Physics and Nanotechnology
Skjernvej 4A
9220 Aalborg Øst
Phone: +45 9940 9215
http://physics.aau.dk

Title:
Development of a Surface Magneto-Optic Kerr Effect Setup

Theme:
Advanced Applications of Nanotechnology

Project Period:
Master thesis
September 2nd, 2010 to
July 1st, 2011

Project Group:
5.217a

Group Members:
Rasmus Bjørn
Kristian Bonderup Pedersen

Supervisor:
Lars Diekhöner

Number of Copies: 5

Number of Pages: 115

Number of Appendices: 5

Total Number of Pages: 138

Abstract

Interest in magnetic nanostructures has increased together with the technological progress. Application of magnetic nanostructeres in e.g. hard disk drives and as magnetic sensors is one of the reasons for increasing demands on size and control of the reorientation of magnetic moments. Based on this a versatile method for characterizing magnetic nanostructeres is essential. The magneto-optic Kerr effect has been used for decades in magnetic analysis, and by combining this concept with a UHV chamber one obtains a surface sensitive method for characterizing magnetic properties of structures in the monolayer range. Accordingly the primary objective of this project is to develop a setup utilizing the surface magneto-optic Kerr effect and adapt it to an existing UHV chamber. Secondly the setup is validated through surface magneto-optic Kerr effect measurements on Co thin films.

Generally the project is separated in three parts: introductory theory, design and development, and finally validation of the system through Kerr effect measurements on Co thin films.

The introductory theory contains the knowledge necessary in order to understand the concept of magneto-optic kerr effect and the magnetic properties of thin films. Initially the basic concepts of magnetism are defined through a semi-classical and statistical mechanical approach. Afterwards magnetism in systems of reduced deimensions, more specifically thin films, is regarded using anisotropy considerations. Finally the concept of magneto-optic Kerr effect is discussed and a setup utilizing the effect for magnetic probing is presented.

It is desired to adapt the surface magneto-optic Kerr effect setup to an existing vacuum system already containing a vaporizer, mass spectrometers, LEED, and a STM. To ease the design of the system, a preliminary simplfified surface magneto-optic Kerr setup is fabricated outside of vacuum. This setup is also used to validate the method as a means to characterize magnetic properties. During the development of the main setup several concepts were considered, the primary are presented chronologically with regard to when they were considered along with pros and cons of the idea. Finally the blueprints for the components designed are presented for the entire final setup.

The final setup comprises numerous components and applications. Overall the setup is centered around a custom designed electromagnet able to deliver app. $200mT$ in a polar and longitudinal configuration. Furthermore the addition of a cryostat enables cooling to $-183°C$ for sample characterization at lowered temperatures.

Through Kerr effect measurements various deficiencies in the setup are identified, e.g. problems with: the entrance windows to the chamber and large order intensity drift. Inspite of this a hysterisis loop is recorded for Co deposited on $Ag(111)$.

Resume

Fremskridtet indenfor teknologi har medført en stadigt stigende interesse indenfor magnetiske nanostrukturer. Eftersom disse magnetiske nanostrukturer har fundet anvendelse indenfor harddisk og magnetisk sensor teknologi, er kravene til størrelse og kontrol af reorientering af magnetiske momenter stigende. På grund af dette følger det at en metode til at karakterisere disse nanostrukturer er nødvendig. I årtier er netop den magneto-optiske Kerr effekt blevet anvendt til karakterisering af magnetiske film. Ved at kombinere konceptet med et UHV kammer, opnår man ydermere en metode til at karakterisere magnetiske egenskaber af strukturer i tyndfilm med en tykkelse i størrelsesordenen af et monolag. Derfor er den primære opgave af projektet at udvikle et overflade magneto-optisk Kerr effekt setup der kan tilpasses til et eksisterende UHV kammer. Anden del af projektet udgør en validering systemets funktionalitet, hvilket gøres igennem Kerr effekt målinger på *Co* tyndfilm.

Generelt er projektet delt i tre: indledende teori, design og udvikling af systemetet og endelig validering af systemet igennem Kerr effekt målinger på *Co* tyndfilm.

Den indledende teori indeholder afsnit, som er nødvendige for at forstå koncepter som magneto-optisk Kerr effekt og magnetiske egenskaber af tyndfilm. Indledningsvis introduceres de basale størrelser indenfor magnetismen i en semiklassisk/statistisk mekanisk adgangsvinkel. Herefter betragtes magnetisme i tyndfilm ud fra anisotropi. Endeligt diskuteres konceptet magnete-optisk Kerr effekt og der redegøres for hvordan en opstilling der udnytter det kunne konstrueres.

Det ønskes at tilpasse opstillingen til et eksisterende UHV kammer der allerede indeholder en fordamper, masse spektrometre, LEED og et skannende tunnel mikroskop. For at simplificere design fasen af systemet blev en simplere indledende opstilling konstrueret hvor alt er placeret udenfor vakuum. Dette setup tjente også det formål at metoden som helhed blev valideret som karakteriseringsmetode med hensyn til magnetiske egenskaber. Mange forskellige koncepter blev overvejet i løbet af design fasen, de primære af disse er præsenteret kronologisk i forhold til hvornår de blev overvejet, sammen med fordele og ulemper ved det pågældende setup. Desuden præsenteres blueprints for alle de komponenter der optræder i det endelige setup.

Det endelige setup indeholder adskillige komponenter og anvendelsesmuligheder. Generelt er systemet centreret omkring en specialfremstillet elektromagnet som kan levere ca. $200mT$ i en polær og longitudinal geometri. Endvidere er der tilføjet en kryostat som muliggør køling ned til $-183°C$ til karakterisering ved lave temperaturer.

Igennem Kerr effekt målinger blev det muligt at identificere diverse mangler i systemet, fx. problemer med vinduerne ind til kammeret samt høj grad af drift i intensity. På trods af disse mangler blev en hysterese kurve målt for en *Co* tyndfilm deponeret på $Ag(111)$.

Preface

This master's thesis is conducted at the Department of Physics and Nanotechnolgy at Aalborg University, Denmark in the period from september 2^{nd} 2010 to July 1^{st} 2011 by Rasmus Bjørn and Kristian Bonderup Pedersen. The theme of the thesis is "Advanced Applications of Nanotechnology", and the overall aim is to develop a setup utilizing the surface magneto-optic Kerr effect to characterize magnetic properties of thin films. The thesis is written under the supervision of associate professor Lars Diekhöner.

Apart from the appendices and the formal sections of a report the thesis consists of three parts: theoretical aspects in chapters 3, 4, and 5; design and development in chapters 6 and 7; and a validation of the setup through Kerr effect measurements on *Co* thin films chapter 8. The appendices includes: a description of equipment and programs used, additional calculations and design blueprints, and surface magneto-optic Kerr measurements on reference samples.

References are presented as numbers in square brackets, e.g. [33], referring to the bibliography situated at the end of the report. Whenever the citation is placed at the end of a section it refers to the entire section. Figures from external sources are cited at the end of the captions, othervise the figure is self-made. Throughout the project the following references are abbreviated: Sec.:section, Cha.:chapter, App.:appendix, and Eq.:equation. Other abbreviations are introduced continuously in parenthesis after the word is introduced.

Regarding mathematical notation, equations are centered on individual lines and are numbered chronologically when referred to. Vectors are denoted with arrows $\vec{a}$ and tensors with a double bar $\overline{\overline{A}}$. Whenever an equation spans more than a single line it is separated in front of a given symbol, multiplication is noted as $\times$.

The following deserve a special thanks for their contribution to the project:

- Hans Nilson
- Jens Rafaelsen
- Peter Kjær Kristensen
- Christian Jensen
- Anders Birk Sørensen

Rasmus Bjørn
Aalborg University July 1^{st} 2011

Kristian Bonderup Pedersen
Aalborg University July 1^{st} 2011

Contents

1 Introduction

Magnetic behaviour of materials have been of interest in centuries. The application of the phenomena, however, was very limited until its connection to electricity was discovered in 1819 by Hans Christian Oersted. During a lecture demonstration he observed that an electric current in a wire deflected the needle in a compass. This discovery was followed by several other and culminated with the definition of Maxwell's equations in 1862 that unite the areas of electricity, magnetism, and optics. Naturally, discoveries within the field of electromagnetisme continued in the following years. [27, p.894-896]

Interest in magnetic thin films intensified significantly in the fifties as IBM introduced the first hard disk drive (HDD) into one of their accounting computers. However, it was not until the late eighties that the interest became "public" as HDDs became available in personal computers. The concept of the HDD is simply to store data by magnetizing a ferromagnetic material in one of two predefined directions, storing data as binary strings. Until 2005 the ferromagnetic domains was orientated parallel to the surface of the HDD but the increasing demand on storage capacity lead to the introduction of perpendicularly orintated domains. This change in procedure in fact underlines the integral problem in HDD technology - keeping up with the increasing demand on speed and capacity, see Figure 1.1. [31]

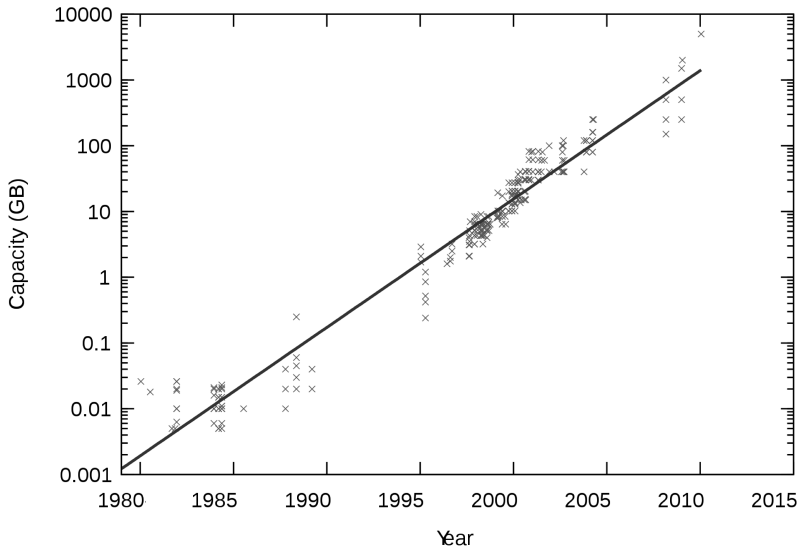

Figure 1.1: Change in storage capacity in HDDs since 1980. The second axis is logarithmic in order to illustrate the exponential behaviour of the graph.

The change in HDD capacity since 1980 is as spectacular as the improvements in central processing units. In 1980 the first gigabyte-capacity disk drive was presented, it weighed app. $250kg$ and had a cost of $40,000. Compared to the common $3Tb$ HDDs available today for less than $200 with a weight below $1kg$ the evolution is evident. In Figure 1.1 a continuation of the exponential evolution in HDD capacity gives an indication of the demands on the storage capacity in years to come.

This increase in storage capacity is rendered possible by reducing the size of the ferromagnetic grains and the readers. As the grains and readers continue to decrease in size they become more vulnerable to the random flipping of magnetic moments due to e.g. thermal energy. Based on the increasing demand and problematics connected with improving HDD capacities alternative methods for creating and arranging the ferromagnetic grains may need to be considered. Following this a reliable method for characterizing ferromagnetic nanostructures is needed. The magneto-optic kerr effect has been used in decades for similar purposes with great succes. Moreover the concept is by all means simple and may be combined with many existing vacuum systems. In the following section a historical overview of the method is presented.

1.1 Magneto-Optic Kerr Effect

The concept of magneto-optic Kerr effect (MOKE) was discovered by John Kerr in 1877 during an experiment where he examined the polarization of light reflected from a polished electromagnet. He discovered that the polarization plane of a light beam would be rotated after reflection from a magnetized surface, see Figure 1.2. Moreover he discovered that the degree of rotation was proportional to the degree of magnetization.

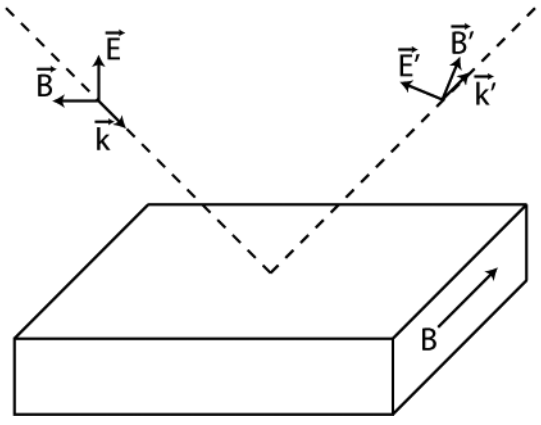

Figure 1.2: Schematic illustrating the concept of MOKE. Incoming electromagnetic radiation is reflected from a transversely magnetised surface resulting in a rotated polarization plane.

Generally the way it was discovered reflects the simplicity of the concept, especially when compared to many other techniques from surface science and optics. Usage

of MOKE in surface characteristics (SMOKE) did not begin before 1985 however, where it was used to study thin *Fe* films deposited on $Au(100)$. SMOKE yielded a method able to measure hysteris loops of the *Fe* thin films with atomic layer sensitivity. [25] [11]

By constructing a SMOKE setup one thereby gains an atomic layer sensitive method for characterizing ferromagnetic nanostructures. Based on this the characterization of ferromagnetic structures of interest is rendered possible. In the following the bilayer triangular islands formed by depositing *Co* on $Cu(111)$ at room temperature are introduced.

1.2 Co Bilayer Triangular Islands

As mentioned above ferromagnetic thin films are studied intensively due to their applications in e.g. magnetic storage media and giant magnetoresistance sensors. Knowledge about the reorientation of the magnetic moments in these ferromagnetic thin films is thus one of the central topics. However, tuning the magnetic reorientation phase transition (RPT), as this process is often named, is troublesome when considering bulk materials. Accordingly, investigating the concept of thickness driven RPT in e.g. *Co* or *Fe* thin films has been of interest in numerous articles, e.g. [13] and [6].

Interesting results has been observed when considering *Co* thin films of submonolayer thickness deposited on *Cu* with various nonmagnetic capping layers. More specifically the influence capping materials as *Au*, *Cu*, *Pd*, *Pt*, *Ag*, and *W* have on the perpendicular magnetic anisotropy as well as RPT has been pursued.

When depositing *Co* onto $Cu(111)$ at room temperature it is well known that the *Co* forms bilayer triangular islands until a certain critical coverage degree. In Figure 1.3 an STM image of $1.1ML$ of *Co* deposited on $Cu(111)$ is displayed, the image is from [5]:

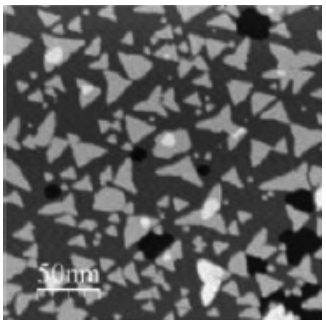

Figure 1.3: STM image of $1.1ML$ of *Co* deposited on $Cu(111)$. The image is from [5].

All these considerations taken into account the bilayer *Co* islands seems to exhibit interesting magnetic properties. Moreover MOKE presents a powerful method for characterizing these magnetic thin films in situ. Combining these two aspects lead

to a formulation of the central problem statement of this project in the following chapter.

Problem Statement 2

The significant interest in magnetic nanostructures is briefly discussed in the introduction. Based on this it is interesting to obtain a method for effectively handling magnetic characterization. The surface magneto-optic Kerr effect is presented in the introduction as a possibility for such a method. The method is conceptually simple and could therefore be adopted to an existing vacuum setup for magnetic characterization in the monolayer range. This is a desirable quality as a UHV chamber containing deposition equipment and a STM is accessible. Therefore the main objective of this master's thesis is to develop a surface magneto-optic Kerr effect setup which is adapted to the existing vacuum chamber.

The secondary objective of the thesis is naturally to test and validate the system created. If the time allows for detailed magnetic characterizaton of a given structure *Co* thin films in the monolayer range presents an interesting choice. Under certain conditions the deposition of *Co* onto $Cu(111)$ in the few monolayer range yields bilayer triangular islands. Characterizing the magnetic properties of these bilayer triangular islands could be a method of validating the SMOKE setup. Finally, interesting effects on the magnetic properties are observed when adding a nonmagnetic capping layer on top of the ferromagnetic structure.

So to summarise, two problematics are of interest in the project, these are as follows:

1. *Development of a versatile surface magneto-optic Kerr effect setup which may be adapted to the existing ultra high vacuum chamber.*

2. *Validation of the surface magneto-optic Kerr effect setup through Kerr measurements. And if the time allows for it a characterization of the magnetic properties of bilayer triangular Co islands, and the effects of capping the islands with a nonmagnetic metal.*

2.1 Purpose and Limitation of the Project

The main topic of this project, is as mentioned above, the development of a setup utilizing the magneto-optic Kerr effect. The secondary topic is first and foremost to validate the system. If possible it is desired to characterize the magnetic properties of *Co* bilayer triangular islands.

This indicates a separation of the project, and apart from the two just mentioned the project contains a third theoretical part. The purpose of the theory included is to understand the surface magneto-optic kerr effect and the concept of magnetism in thin films.

In order to ease the design and development phase of the project a simplified surface magneto-optic Kerr effect setup is created with the sample outside of vacuum. This setup is used solely for validation and optimization of the method.

Designing the arrangement in general is a troublesome process, therefore it is essentiel to master different methods and programs. This includes learning to use programs as: SolidWorks for 3D sketching, COMSOL multiphysics for field simulations, and Visual C-sharp for measurement control; and concepts as: optics in general, vacuum science, assembling and fixation of components, and numerous other topics.

Magnetism 3

This chapter introduces the concept of magnetic behaviour. This includes the definition of magnetic dipoles and thereby magnetization. Afterwards the different magnetic classifications are investigated, including diamagnetic-, paramagnetic-, and ferromagnetic behaviour. Finally the optics of magnetic materials is discussed briefly.

3.1 Magnetization and the Magnetic Susceptibility

Initially a classic electromagnetic approach is used to define the concept of magnetic moment. A given structure is perturbed with an external magnetic field $\vec{H}$ which leads to a magnetic response $\vec{B}$ from the structure. In free space these are proportional through the vacuum permeability $\vec{B} = \mu_0 \vec{H}$. In general however the magnetization $\vec{M}$ of the structure needs be taken into account

$$\vec{B} = \mu_0 \left(\vec{H} + \vec{M} \right). \tag{3.1}$$

The magnetization $\vec{M}$ is naturally a result of the external field $\vec{H}$ and accordingly a quantity referred to as the magnetic susceptibility is defined as

$$\vec{M} = \chi_M \vec{H}. \tag{3.2}$$

It needs to be noted that the magnetic susceptibility in general is a tensor. The magnitude of the magnetization is defined from the amount of magnetic moment pr. volume $M = \frac{\mu N}{V}$. [10, p.2]

By combining Eqs. (3.1) and (3.2) one has

$$\vec{B} = \mu_0 \mu_r \vec{H}, \tag{3.3}$$

where $\mu_r = 1 + \chi_M$ is the relative permeability.

The magnetic classifications discussed later on in this chapter are grouped based on the size and sign of the magnetic susceptibility.

- Diamagnetism - $\chi_M \approx -10^{-5}$
- Paramagnetism - $\chi_M \approx 10^{-5}$
- Collective magnetism - $\chi_M > 1$

In general the magnetic susceptibility is highly temperature dependent and accordingly these values are merely a guidance. Furthermore, for a thorough description

of magnetic behaviour one must apply quantum mechanics, which in the following is used to more accurately define the magnetic classifications. [10, p.3-5] [24, p.134]

3.2 Magnetic Classifications

Basically magnetism can only be defined using quantum mechanics, this is easily outlined by considering the magnetic moment of a free atom. Three characteristics of the magnetic moment is the spin of the electrons, the orbital angular momentum of the electrons, and the change in orbital angular momentum induced by an external magnetic field. The first two effects are paramagnetic contributions while the last is a diamagnetic contribution. These contributions are clearly microscopical and are accordingly described using quantum mechanics. For now however a semiclassical aproach is used as an offset. [14, p.299]

The essential parameter when considering magnetism is the magnetic dipole moment $\vec{\mu}$. Classically this is defined as:

$$\vec{\mu} = I\vec{A}, \tag{3.4}$$

for a current loop, where I is the current and A is the cross sectional area, see Figure 3.1:

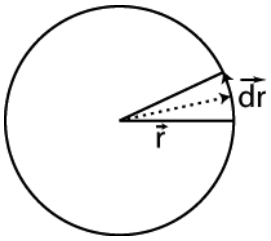

Figure 3.1: An orbiting electron circulating an area A with a period T. Inspired from [24, p.135]

The definition of current is the amount of charge passing an area pr time:

$$I = \frac{dq}{dt} = \frac{q}{T} = -\frac{e}{T}, \tag{3.5}$$

where e is the elementary charge and T the period of circulation. The infinitesimally small area dA spanned by the vectors $\vec{r}$ and $d\vec{r}$ illustrated in figure 3.1 is naturally

given by:

$$\begin{aligned} dA &= 1/2\,|\vec{r}\times d\vec{r}| \\ \frac{dA}{dt} &= 1/2\left|\vec{r}\times\frac{d\vec{r}}{dt}\right| \\ &= 1/2\left|\vec{r}\times\frac{\vec{p}}{m}\right| \\ &= \frac{\left|\vec{L}\right|}{2m} = \frac{L}{2m}, \end{aligned} \tag{3.6}$$

where the momentum $\vec{p} = m\vec{v} = m\dfrac{d\vec{r}}{dt}$ and the angular momentum $\vec{L} = \vec{r}\times\vec{p}$ are introduced. Futhermore $\dfrac{dA}{dt} = \dfrac{A}{T}$ for elliptic orbits, this combined with Eq. (3.6) yields:

$$\frac{A}{T} = \frac{L}{2m}. \tag{3.7}$$

By inserting Eqs. (3.5) and (3.7) into Eq. (3.4) one has the following expression for the magnetic dipole moment given by the angular momentum:

$$\vec{\mu} = -\frac{e}{2m}\vec{L}. \tag{3.8}$$

Eq. (3.8) underlines the statement that the concept of magnetism originates from the angluar momentum and spin of electrons. From this point it is easy to convert this classical investigation of magnetism into a quantum mechanical investigation by introducing the angular momentum operator instead of the classical angular momentum.

$$\begin{aligned} \hat{L}^2\psi &= l(l+1)\hbar^2\psi \\ \hat{L}_z\psi &= m_l\hbar\psi, \end{aligned} \tag{3.9}$$

where l and m_l are the quantum numbers and ψ is the eigenfunction of the operators. Similar equations may be stated concerning the spin quantum numbers s, m_s or the total angular momentum quantum numbers j, m_j. [7, p.220]

Generally the orbital angular momentum can be used to express the magnetic moment as

$$\vec{\mu} = -\frac{g\mu_B\vec{J}}{\hbar}, \tag{3.10}$$

where g is the Landé g-factor, μ_B is the Bohr magneton, and $\vec{J} = \vec{L} + \vec{S}$ is the sum of the orbital and spin angular momentum. The Landé g-factor and the Bohr magneton are given as [14, p.302] [24, p.136]

$$\begin{aligned} g &= 1 + \frac{j(j+1) - l(l+1) + s(s+1)}{2j(j+1)} \\ \mu_B &= \frac{e\hbar}{2m}. \end{aligned} \tag{3.11}$$

By combining Eqs. (3.9) and (3.10) the z-component of the magnetic moment becomes

$$\mu_z = -\frac{g\mu_B J_z}{\hbar} = -g\mu_B m_j \tag{3.12}$$

It is clear from Eq. (3.11) that $g = 1$ when $s = 0$ and $g = 2$ when $l = 0$. By inserting this into Eq. (3.12) one has

$$\begin{aligned}\mu_z^l &= -\mu_B m_l \\ \mu_z^s &= -2\mu_B m_s = \pm\mu_B,\end{aligned}$$

as $m_s = \pm 1/2$ for fermions.

Eq. (3.12) is used later on when defining paramagnetism. In the following a different approach is used to investigate diamagnetism.

3.2.1 Diamagnetism

In the following the concept of atomic diamagnatism is examined by considering an atom with Z electrons in a magnetic field. Generally the behaviour on microscopic scale is governed by the Schrödinger equation, and thereby the Hameltonian. The full Hamiltonian for an isolated atom in external fields is in [7, p.237] given as:

$$\begin{aligned}\hat{H} &= \hat{H}_0 + \hat{H}_{so} + e\vec{r}\cdot\vec{E} + \mu_B\left(\hat{L} + g_s\hat{S}\right)\cdot\vec{B} + \frac{e^2}{8m}\sum_{i=1}^{Z}\left(\vec{B}\times\vec{r}_i\right)^2 \\ &= \hat{H}_0 + \hat{H}_{so} + e\vec{r}\cdot\vec{E} + \hat{H}_{para} + \hat{H}_{dia}.\end{aligned} \tag{3.13}$$

The fundamental Hamilton term $\hat{H}_0$ and the spin-orbit term $\hat{H}_{so}$ are of no interest in the present context as the goal is to derive the modification due to an external magnetic field $\vec{B}$. Furthermore, in the abscense of an external electric field $\vec{E}$ the remaining terms of interest are

$$\begin{aligned}\hat{H}_1 &= \mu_B\left(\hat{L} + g_s\hat{S}\right)\cdot\vec{B} + \frac{e^2}{8m}\sum_{i=1}^{Z}\left(\vec{B}\times\vec{r}_i\right)^2 \\ &= \hat{H}_{para} + \hat{H}_{dia}.\end{aligned}$$

To simplify the deriviation it is assumed that all electronic shells are filled. Accordingly the angular momenta vanishes, $\vec{L}, \vec{S} = \vec{0}$. By orientating the magnetic field along the z-axis, $\vec{B} = B\hat{z}$, the Hamiltonian concerning the influence of an external magnetic field is reduced to: [10, p.9]

$$\begin{aligned}\hat{H}_1 &= \frac{e^2}{8m}\sum_{i=1}^{Z}\left(B\hat{z}\times\vec{r}_i\right)^2 \\ &= \frac{B^2e^2}{8m}\sum_{i=1}^{Z} y_i^2 + x_i^2.\end{aligned}$$

From this Hamiltonian the change in ground state energi due to the diamagnetic term amounts to

$$\Delta E_0^{dia} = \frac{B^2 e^2}{8m} \sum_{i=1}^{Z} \langle 0 | y_i^2 + x_i^2 | 0 \rangle, \tag{3.14}$$

where $|0\rangle$ is the wave function of the ground state. Ground state atoms with filled electron shells naturally exhibit spherically symmetric wavefunctions, accordingly $\langle x_i^2 \rangle = \langle y_i^2 \rangle = \langle z_i^2 \rangle = 1/3 \langle r_i^2 \rangle$. This reduces Eq. (3.14) to

$$\Delta E_0^{dia} = \frac{B^2 e^2}{12m} \sum_{i=1}^{Z} \langle 0 | r_i^2 | 0 \rangle.$$

Introducing the magnetic equation of state $M = -\dfrac{\partial F^*}{\partial B}$ together with the Helmholtz free energy for conservative fields $F^* = E - TS$ at $T = 0$ gives the magnetization as: [26, p.228-229]

$$\begin{aligned} M &= -\frac{\partial F^*}{\partial B} \\ &= -\frac{N}{V} \frac{\partial \Delta E_0^{dia}}{\partial B} \\ &= -\frac{N}{V} \frac{\partial}{\partial B} \frac{B^2 e^2}{12m} \sum_{i=1}^{Z} \langle r_i^2 \rangle \\ &= -\frac{N e^2 B}{6mV} \sum_{i=1}^{Z} \langle r_i^2 \rangle, \end{aligned} \tag{3.15}$$

where N is the number of atoms in the volume V. Given a linear material and a relative permeability in the order of $\mu_r \approx 1$, as would be the case in vacuum, the magnetic susceptibility is found from Eqs. (3.2) and (3.3) as:

$$\chi_M = \frac{M}{H} = \frac{\mu_0 M}{B}. \tag{3.16}$$

By inserting Eq. (3.15) into Eq. (3.16) one has

$$\begin{aligned} \chi_M &= -\frac{\mu_0}{B} \frac{N e^2 B}{6mV} \sum_{i=1}^{Z} \langle r_i^2 \rangle \\ &= -\frac{N \mu_0 e^2}{6mV} \sum_{i=1}^{Z} \langle r_i^2 \rangle. \end{aligned} \tag{3.17}$$

Based on Eq. (3.17) it is possible to gain an understanding of diamagnetic behaviour. As all constants and parameters on the right hand side of Eq. (3.17) are real and positive the diamagnetic susceptibility is negative, $\chi_M^{dia} < 0$. Furthermore the susceptibility is proportional to the expectation value of the distance from the core squared $\chi_M^{dia} \propto \langle r_i^2 \rangle$, and accordingly only the outermost electron shells contribute significantly. It is worth noting that through a more general calculation than the one carried out, it is possible to show that the diamagnetic susceptibility has a neglible temperature dependence. [10, p.9-10]

3.2.2 Paramagnetism

By utilizing Sec. 3.2 and applying statistical mechanics to a simple paramagnetic crystal the concept of paramagnetism is investigated in the following. For simplicity only spin moments are considered meaning that the z-component of the magnetic moment only assumes two values and $m_j = \pm 1/2$. Furthermore the magnetic moments considered are isolated from everything else than applied fields. [10, p.14] [24, p.136]

The interaction energy depends on the orientation of the moment and the applied field:

$$E = -\vec{\mu} \cdot \vec{B}. \tag{3.18}$$

By combining Eqs. (3.12) and (3.18) and aligning the magnetic field parallel to the z-axis one has:

$$E = -g\mu_B m_j B = \pm \mu_B B, \tag{3.19}$$

as $m_j = m_s = \pm 1/2$ and $g = 2$ for fermions. The two possible momenta creates a two-level-system with a spin up and spin down state with related exchange energies. As all momenta are localized in certain lattice positions the system obeys Maxwell-Boltzmann statistics, hence the average moment is found using the Maxwell-Boltzmann distribution function:

$$\langle \mu_z \rangle = \sum_i \frac{\mu_i e^{-E_i/k_B T}}{Z},$$

where Z in this case is the partition function $Z = \sum_i e^{-E_i/k_B T}$ and the degeneracy is set to 1. [26, p.336-337,399-400] [24, p.136-137]

As all momenta in the lattice are isolated from each other the sum parameter i only assumes two values, namely the two energies defined in Eq. (3.19):

$$\begin{aligned} \langle \mu_z \rangle &= \frac{\mu_B e^{-\mu_B B/k_B T} - \mu_B e^{\mu_B B/k_B T}}{e^{\mu_B B/k_B T} + e^{-\mu_B B/k_B T}} \\ &= \mu_B \tanh\left(\frac{\mu_B B}{k_B T}\right). \end{aligned} \tag{3.20}$$

Eq. (3.20) leads to a relative magnetization M/M_S:

$$\frac{M}{M_S} = \frac{\langle \mu_z \rangle}{\mu_B} = \tanh(y), \tag{3.21}$$

where M_S is the saturation magnetization where all magnetic moments are parallel and $y = \dfrac{\mu_B B}{k_B T}$. The relative magnetization is plotted in Figure 3.2:

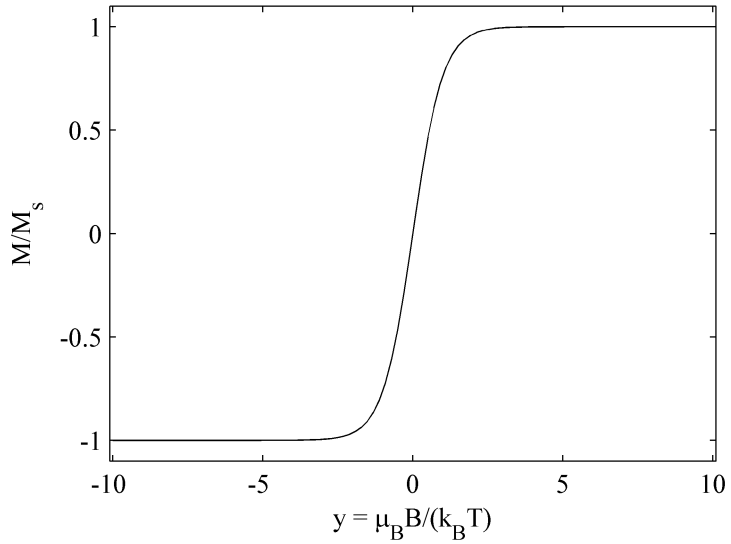

Figure 3.2: Relative magnetization of a paramagnet containing only spin moments. The relative magnetization is given by $\tanh y$ where $y = \dfrac{\mu_B B}{k_B T}$. All units in the plot are arbitrary.

It is seen in Figure 3.2 that for large fields or small temperatures the magnetization approaches the saturation value. This naturally means that all spins are in the same direction. The opposite case is seen for large temperatures or small fields where the magnetization vanishes, due to the thermal fluctuations of the moments.

From this point it is possible to find the magnetization of this two-level spin state system and thereby calculate the paramagnetic susceptibility. Initially the magnetization M_z is found from

$$M_z = n\left\langle \mu_z \right\rangle = n\mu_B \tanh\left(\frac{\mu_B B}{k_B T}\right), \tag{3.22}$$

where n is the atom density. From Eq. (3.22) the paramagnetic susceptibility is found as:

$$\begin{aligned}
\chi_M^{para} &= \frac{\partial \vec{M}}{\partial \vec{H}} \\
&= \frac{\partial}{\partial H} n\mu_B \tanh\left(\frac{\mu_B B}{k_B T}\right) \\
&= \frac{n\mu_B}{H}\frac{\mu_B B}{k_B T}\frac{1}{\cosh^2\left(\frac{\mu_B B}{k_B T}\right)} \\
&= \frac{n\mu_B y}{H}\frac{1}{\cosh^2(y)}.
\end{aligned} \tag{3.23}$$

Eq. (3.23) is plotted in Figure 3.3 for a constant magnetic field and as a function of $1/y$ to illustrate the temperature dependence:

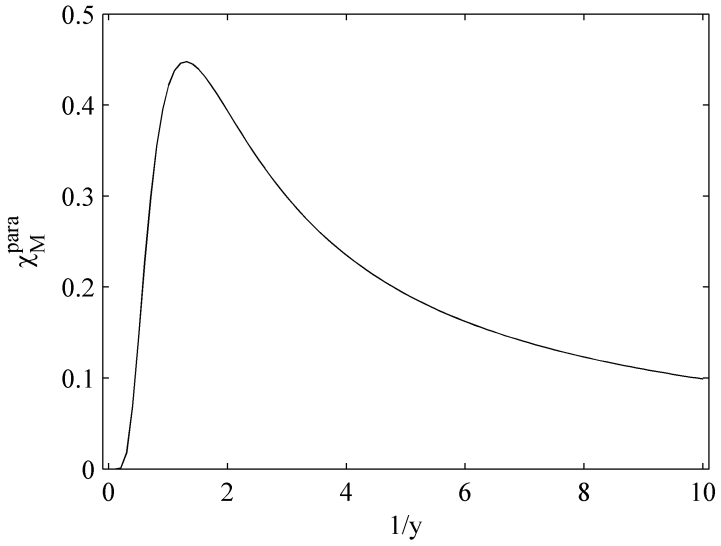

Figure 3.3: Plot of the magnetic susceptibility of a paramagnetic crystal. The susceptibility is given by $\chi_M = \frac{y}{H\cosh^2(y)}$ where $y = \frac{\mu_B B}{k_B T}$. All units in the plot are arbitrary.

From Figure 3.3 it is seen that when $T \to 0K$ the magnetic susceptibility vanishes making the material harder to magnetize. This is due to the origin of paramagnetism, which is the spin and orbital angular momentum of electrons. At $0K$ all electrons are in the ground state cancelling out the angular momentum. Above $0K$ electrons may be excited creating magnetic dipoles in the process. Accordingly the magnetic susceptibility increases with temperature, but only to a certain degree. At some point the thermal fluctuations overcome the magnetic field making the material harder to magnetize, which is apparent from the figure. [10, p.13-15] [24, p.136-140]

Curie's Law

In the high temperature limit the hyperbolic tangent function in Eq. (3.21) may be expanded:

$$P(y) = \sum_{n=0}^{\infty} \frac{f^{(n)}(a)}{n!}(y-a),$$

around $y = 0$ to the first order, which combined with the same steps carried out during Eqs. (3.22) and (3.23) yields:

$$\begin{aligned}\chi_M &= \frac{\partial}{\partial \vec{H}} \frac{n\mu_B^2 B}{k_B T} \\ &= \frac{n\mu_0 \mu_B^2}{k_B T}\end{aligned}$$

$$= \frac{C}{T}. \tag{3.24}$$

Eq. (3.24) is known as known as Curie's law and the constant $C = \frac{n\mu_0\mu_B^2}{k_B}$ as Curie's constant. [10, p.13] [24, p.139]

General Angular Momentum

In the example considered in Sec. 3.2.2 only the spin is included in the total angular momentum. It can be shown that an arbitrary angular momentum J gives rise of a magnetic moment as

$$\langle \mu_j \rangle = \mu_B g j B_j(z), \tag{3.25}$$

where

$$B_j(z) = \frac{2j(j+1)}{2j} \coth\left(\frac{2j+1}{2j}z\right) - \frac{1}{2j}\coth\left(\frac{z}{2j}\right). \tag{3.26}$$

In Eq. (3.26) $B_j(z)$ is the so-called Brillouin function with $z = \frac{g\mu_B j}{k_B T}B$. It needs to be noted that in solids the orbital momentum, which is taken into account in Eq. (3.25), is quenched by crystal field effects, accordingly the simplified consideration in Sec. 3.2.2 is sufficient.

3.2.3 Collective Magnetism

In the previous two examples regarding diamagnetism and paramagnetism all magnetic moments were considered completely isolated. However, in reality permanent magnetic dipoles exhibit a significant exchange interaction, which results in a spontaneous magnetization even in the abscence of external applied fields. Exchange interactions between magnetic dipoles cannot be explained using classical physics, it is purely an quantum mechanical effect which is handled briefly in the following section.

The magnetic moments giving rise to this magnetization can be localized or itinerant. Generally collective magnetism is divided into three subcategories: ferromagnetism, ferrimagnetism, and antiferromagnetism. Common for all of the sub types is a so-called critical temperature T^* below which a spontaneous magnetization is present without an external field. See Figure 3.4 for an illustration of the types of collective magnetism.

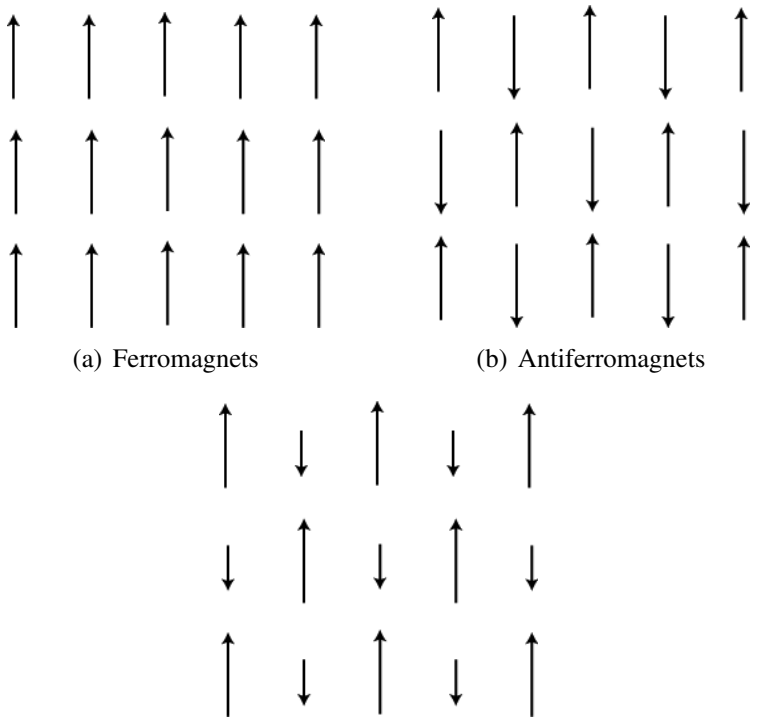

(a) Ferromagnets (b) Antiferromagnets

(c) Ferrimagnets

Figure 3.4: Illustration of the ordering of magnetic moments of ferromagnetism (a), antiferromagnetism (b), and ferrimagnetism (c). Inspired from [14]

3.2.4 Ferromagnetism

As mentioned above ferromagnetic materials exhibit ordered magnetic moments in the abscence of external fields. At $T = 0K$ all magnetic moments are parallel due to the concept of exchange interaction between dipoles. By taking the relevant parts og the Hamiltonian introduced in Eq. (3.13) and introducing a term that includes this so-called exchange interaction one has: [10, p.48]

$$\begin{aligned}\hat{H} &= -\sum_{ij} J_{ij}\vec{S}_i \cdot \vec{S}_j + g_S\mu_B \sum_i \vec{S}_i \cdot \vec{B} \\ &= \hat{H}_{exchange} + \hat{H}_{dia}.\end{aligned} \tag{3.27}$$

In Eq. (3.27) terms concerning all but the change due to magnetic fields are neglected. Furthermore only spin moments are considered for simplicity. Finally the parameter J_{ij} in the exchange term of the Hamiltonian is the exchange constant between spin i and j. A good approximation of the exchange constant is

$$J_{ij} = \begin{cases} J & \text{n.n. spins} \\ 0 & \text{else} \end{cases} \tag{3.28}$$

where n.n. signifies nearest neighbors.[1]

The concept of interacting magnetic ions throughout an infinite lattice is an over-

[1] The exchange constant J in Eq. (3.28) is not to be confused with the angular momentum $\vec{J}$.

whelming problem. However, the problem is significantly simplified by introducing a so-called molecular field $\vec{B}_{mf}$. This molecular field is an inner magnetic field that arises from the aligned magnetic moments due to the exhange interaction. Naturally this field is proportional to the magnetization from the aligned magnetic moments

$$\vec{B}_{mf} = \lambda \vec{M}. \tag{3.29}$$

In Eq. (3.29) λ is the molecular field constant, which for ferromagnets are positive. [10, p.48]

Thus by introducing the molecular field the problem of interacting dipoles is reduced to the same situation as in the paramagnetic example in Sec. 3.2.2 with a modified magnetic field of $\vec{B}+\vec{B}_{mf}$. Accordingly the relative magnetization is given by Eq. 3.21 with the modified field inserted. However, for a more general solution the relative magnetization is expressed from the Brillouin function in Eq. (3.26):

$$\frac{M}{M_S} = B_j(z), \tag{3.30}$$

where $z = \dfrac{g\mu_B j\,(B+\lambda M)}{k_B T}$. By evaluating Eq. (3.30) in the limit where the external field vanishes $B = 0$, the temperature dependence of the magnetization becomes:

$$M(T) = M_S B_j\left(\frac{g\mu_B j\lambda M(T)}{k_B T}\right).$$

This differential equation naturally has a trivial solution $M(T) = 0$, however physically other solutions are more interesting. Graphically the equation is easily solved by:

$$\begin{aligned}\frac{M(T)}{M_S} &= \frac{M(T)}{M_S}\frac{g\mu_B j\lambda M(T)}{k_B T}\frac{k_B T}{g\mu_B j\lambda M(T)} \\ &= y\frac{k_B T}{g\mu_B j\lambda M_S}.\end{aligned}$$

This is seen in Figure 3.5.

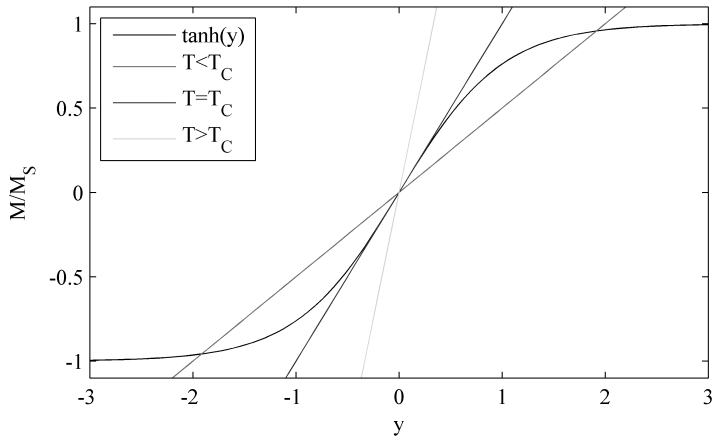

Figure 3.5: Graphic solution to the differential equation in Eq. (3.2.4). For large temperatures $T > T_C$ only one solution exist, $M = 0$, whereas for low temperatures $T < T_C$ there are three.

It is clear from Figure 3.5 that for ferromagnetic materials a critical temperature T_C exists. The critical temperature for ferromagnets is called the Curie temperature and indicate the point where spontaneous magnetization without external fields vanish. This is seen in the figure as only one solution is seen for $T > T_C$ namely $M = 0$ whereas three solutions are seen for $T < T_C$.

The Curie temperature is derived as

$$T_C = \frac{n\lambda\mu_{eff}^2}{3k_B},$$

where $\mu_{eff} = g\mu_B\sqrt{j(j+1)}$.

Conclusively materials exhibiting ferromagnetic probatilities are divided in two domains separated by the Curie temperature. A ferromagnetic domain where spontaneous magnetization occurs and a paramagnetic domain where an external field is needed in order to align the magnetic dipoles.

3.3 Optics of Magnetic Materials

In general most materials need to be handled as aniostropic when considered optically. This even includes most crystal structures as these have a low degree of optical symmetry. In the following the propagation of light in an anisotropic media is handled, for now all magneto-optic effects are neglected however. This section is inspired from [15, Ch.9]

As in most cases where electromagnetic radiation is handled one starts with the

four Maxwell's equations:

$$\vec{\nabla} \times \vec{H} = \vec{J} + \frac{\partial \vec{D}}{\partial t} \qquad \text{Extended Ampere's law} \tag{3.31a}$$

$$\vec{\nabla} \times \vec{E} = -\frac{\partial \vec{B}}{\partial t} \qquad \text{Faraday's law of induction}$$

$$\vec{\nabla} \cdot \vec{D} = \rho \qquad \text{Gauss's law for } \vec{E}\text{-fields}$$

$$\vec{\nabla} \cdot \vec{B} = 0, \qquad \text{Gauss's law for } \vec{B}\text{-fields,}$$

where $\vec{J}$ is the current density, and ρ is the density of free charges. In most optical problems free charges and currents are non-existent in the medium and are accordingly left out. Based on this, one has:

$$\vec{\nabla} \times \vec{H} = \frac{\partial \vec{D}}{\partial t} \tag{3.32a}$$

$$\vec{\nabla} \times \vec{E} = -\frac{\partial \vec{B}}{\partial t} \tag{3.32b}$$

$$\vec{\nabla} \cdot \vec{D} = 0$$

$$\vec{\nabla} \cdot \vec{B} = 0.$$

The goal of the following calculations is to derive a solution of the plane wave form with a phase dependence of

$$\phi = e^{-i[(\omega/c)n\hat{s}\cdot\vec{r} - \omega t]},$$

where $\vec{k} = \frac{\omega}{c} n\hat{s}$.

In the basic rectangular coordinates used the time-derivative $\partial/\partial t$ and the $\vec{\nabla}$ yield simple results when applied to plane wave type solutions:

$$\frac{\partial}{\partial t} \rightarrow i\omega \tag{3.33a}$$

$$\vec{\nabla} \rightarrow -i\vec{k}. \tag{3.33b}$$

By applying the operator identity in Eq. (3.33a) to Ampere's law (3.32a) and Faraday's law of induction (3.32b) one has:

$$\vec{\nabla} \times \vec{H} = i\omega\vec{D}, \tag{3.34}$$

and

$$\vec{\nabla} \times \vec{E} = -i\omega\vec{B}. \tag{3.35}$$

Applying Eq. (3.3) to Eq. (3.35) and combining it with Eq. (3.34) yields:

$$\vec{\nabla} \times \vec{\nabla} \times \vec{E} = \mu_0 \mu_r \omega^2 \vec{D}. \tag{3.36}$$

Eq. (3.36) is a second order linear partial differential equation referred to as the generalized wave equation. The complete solution to this wave equation contains all physical possible electric fields.

Now the second operator identity defined in Eq. (3.33b) is applied to the wave equation in Eq. (3.36):

$$\begin{aligned}\vec{\nabla}\times\vec{\nabla}\times\vec{E} &= -\frac{\omega^2 n^2}{c^2}\hat{s}\times\hat{s}\times\vec{E}\\ &= -\frac{\omega^2 n^2}{c^2}\left[\hat{s}\left(\hat{s}\cdot\vec{E}\right)-\hat{s}\cdot\hat{s}\vec{E}\right]\\ &= -\frac{\omega^2 n^2}{c^2}\left[\hat{s}\left(\hat{s}\cdot\vec{E}\right)-\vec{E}\right],\end{aligned}$$

where the vector identity $\vec{\nabla}\times\vec{\nabla}\times = \vec{\nabla}\left(\vec{\nabla}\cdot\right)-\nabla^2$ is utilized. Inserting this result into the wave equation gives an expression for the dielectric displacement from the electric field:

$$\vec{D} = \frac{n^2\varepsilon_0}{\mu_r}\left[\vec{E}-\hat{s}\left(\hat{s}\cdot\vec{E}\right)\right]. \tag{3.37}$$

In principal this result is general without any assumptions apart from the plane-wave approach. For now, however, this result is left alone while the concept of a dielectric tensor is introduced.

When calculating field components of e.g. the dielectric displacement from the electric field, as in Eq. (3.37). One may readily utilize the dielectric tensor $\bar{\bar{\varepsilon}}$ of the given medium:

$$\vec{D} = \bar{\bar{\varepsilon}}\vec{E}, \tag{3.38}$$

where

$$\vec{E} = \begin{bmatrix}E_x\\E_y\\E_z\end{bmatrix}$$

$$\vec{D} = \begin{bmatrix}D_x\\D_y\\D_z\end{bmatrix}$$

$$\bar{\bar{\varepsilon}} = \begin{bmatrix}\varepsilon_{xx} & \varepsilon_{xy} & \varepsilon_{xz}\\ \varepsilon_{yx} & \varepsilon_{yy} & \varepsilon_{yz}\\ \varepsilon_{zx} & \varepsilon_{zy} & \varepsilon_{zz}\end{bmatrix}$$

By direct calculation of (3.38) it is found that

$$D_i = \sum_{j=1}^{3}\varepsilon_{ij}E_i. \tag{3.39}$$

In general all entries of the dielectric tensor are frequency dependent and may be complex. Based on this all the entries may be unique and simplifying the tensor

impossible.

In many cases the medium under consideration is to some degree both nonabsorbing and not optical active. In this case the tensor elements are real and symmetric so that $\varepsilon_{ij} = \varepsilon_{ji}$. Based on this, it is always possible to rotate the coordinate system to a point where the tensor becomes diagonal. In this case the tensor only contains three independent values:

$$\overline{\overline{\varepsilon}} = \begin{bmatrix} \varepsilon_x & 0 & 0 \\ 0 & \varepsilon_y & 0 \\ 0 & 0 & \varepsilon_z \end{bmatrix}$$

This particular axis of orientation is called the principal axis. For uniaxial mediums the tensor has two equal elements and for biaxial mediums all principal values of the tensor are different.

Magnetic materials, however, cannot be regarded as nonabsorbing. And accordingly each entry of the dielectric tensor needs to be handled as unique to prevent loss of generality. By combining Eqs. (3.37) and (3.39) one obtains three separate equations:

$$0 = \frac{n^2 \varepsilon_0}{\mu_r} \left[E_i - s_i \sum_{j=1}^{3} s_j E_j \right] - \sum_{j=1}^{3} \varepsilon_{ij} E_i,$$

or written in terms of tensors

$$\overline{\overline{M}} \vec{E} = 0, \tag{3.40}$$

where

$$\overline{\overline{M}} = \begin{bmatrix} n^2\left(1 - s_x^2\right) - \dfrac{\varepsilon_{xx}\mu_r}{\varepsilon_0} & -n^2 s_x s_y - \dfrac{\varepsilon_{xy}\mu_r}{\varepsilon_0} & -n^2 s_x s_z - \dfrac{\varepsilon_{xz}\mu_r}{\varepsilon_0} \\ -n^2 s_y s_x - \dfrac{\varepsilon_{yx}\mu_r}{\varepsilon_0} & n^2\left(1 - s_y^2\right) - \dfrac{\varepsilon_{yy}\mu_r}{\varepsilon_0} & -n^2 s_y s_z - \dfrac{\varepsilon_{yz}\mu_r}{\varepsilon_0} \\ -n^2 s_z s_x - \dfrac{\varepsilon_{zx}\mu_r}{\varepsilon_0} & -n^2 s_z s_y - \dfrac{\varepsilon_{zy}\mu_r}{\varepsilon_0} & n^2\left(1 - s_z^2\right) - \dfrac{\varepsilon_{zz}\mu_r}{\varepsilon_0} \end{bmatrix}.$$

From (3.40) it is possible to calculate the exact field at any position if the material characteristics are unknown. In many cases however, parameters like the index of refraction is not well defined and accordingly these would need to be calculated initially. This is done by recognizing that the equation has a solution only if the characteristic equation is fulfilled:

$$\det \overline{\overline{M}} = 0.$$

Naturally, the $\overline{\overline{M}}$ tensor is significantly simplified in nonmagnetic- ($\mu_r = 1$) and nonabsorbing materials ($\varepsilon_{ij} \to \varepsilon_{ij}\delta_{ij}$).

It is discussed later what significance these off-diagonal dielectrec tensor elements mean to the magneto-optic Kerr effect. But as is obvious from the $\overline{\overline{M}}$ tensor these non-zero entries will have an impact on all electromagnetic radiation propagating in the given medium.

Magnetism in Reduced Systems

4

In this chapter magnetism in systems with reduced dimensions, specifically thin films, is described. In order to investigate this the concepts of magneto crystalline- and shape anisotropy are introduced.

4.1 Magnetic Anisotropies

In an isotropic system the magnetic dipoles can be rotated with an infinetisimally small amount of energy, hence there is no prefered direction of the magnetization. In such systems ferromagnetism cannot exist, so the effect of anisotropy needs to be considered. Thin films and nano islands are reduced in one or more dimensions making them naturally anisotropic. In the following magneto crystalline- and shape anisotropy are described in detail as these are important for the understanding of magnetism in reduced systems.

4.1.1 Magneto Crystalline Anisotropy

In a crystallographic structure it is easier to magnetize a magnetic material certain specific directions than others. This is caused by the spin-orbit interaction which aligns the spins in the orbitals. This makes the magnetic moments prefer an alignment along well-determined crystallographic axes. These are reffered to as the easy magnetization axes. Instead of evaluating the spin-orbit interactions through a quantum mechanical analysis a phenomenological approach is used. In this approach the expressions are expanded in power series for the different crystal symmetries, with coefficients determined through experiments.

The direction of the magnetization is determined only by the anisotropy even though the magneto crystalline energy is usually small compared to the exchange energy. This is because the exchange energy only depends on the relative allignment of the magnetic moments without regard to the direction. The direction of the magnetization $\vec{m}$ is related to the coordinate axes by the directional cosine α_i, see App. B.

The magneto crystalline energy per volume can be expressed as a powerseries in α with coeficients b having units of $\frac{J}{m^3}$: [10, p. 91]

$$E_{crys} = E_0 + \sum_i b_i \alpha_i + \sum_{ij} b_{ij} \alpha_i \alpha_j + \sum_{ijk} b_{ijk} \alpha_i \alpha_j \alpha_k + \ldots$$

The energy remains the same if all magnetic moments are reversed, hence it only depends on the alignment:

$$\begin{aligned} E\left(\vec{M}\right) &= E\left(-\vec{M}\right) \\ E\left(\alpha_i\right) &= E\left(-\alpha_i\right). \end{aligned} \tag{4.1}$$

As a result of this all odd power terms vanish in the power series yielding:

$$\begin{aligned} E_{crys} = E_0 &+ \sum_{ij} b_{ij}\alpha_i\alpha_j + \sum_{ijkl} b_{ijkl}\alpha_i\alpha_j\alpha_k\alpha_l \\ &+ \sum_{ijklmn} b_{ijklmn}\alpha_i\alpha_j\alpha_k\alpha_l\alpha_m\alpha_n, \end{aligned} \tag{4.2}$$

for terms of up to sixth order in α. In the following Eq. (4.2) is applied to different crysallographic symmetries.

Cubic Systems

Considering first the second order term and the result of Eq. (4.1) all cross terms $\alpha_i\alpha_j$ vanish in the summation, i.e.

$$b_{ij} = b_{ij}\delta_{ij}. \tag{4.3}$$

This is shown in App. B. Furthermore the cubic symmetry makes the indices $i = 1,2,3$ indistinguishable, hence [10, p. 91]:

$$b_{11} = b_{22} = b_{33}. \tag{4.4}$$

Inserting Eqs. (4.3) and (4.4) into Eq. (4.2)

$$\begin{aligned} \sum_{ij} b_{ij}\alpha_i\alpha_j &= b_{11}\left({\alpha_1}^2 + {\alpha_2}^2 + {\alpha_3}^2\right) \\ &= b_{11}. \end{aligned} \tag{4.5}$$

For the higher order terms these considerations are also applicable. Eq. (4.1) makes all terms involving odd powers of α_i cancel e.g.

$$\begin{aligned} b_{1123}\alpha_1\alpha_1\alpha_2\alpha_3 &= 0 \\ b_{1122}\alpha_1\alpha_1\alpha_2\alpha_2 &= b_{1122}{\alpha_1}^2{\alpha_2}^2, \end{aligned}$$

and the the cubic symmetry results in i.e.

$$b_{1122} = b_{1133} = b_{2233}.$$

From Eq. (4.2) the fourth order term is identified as:

$$\begin{aligned} \sum_{ijkl} b_{ijkl}\alpha_i\alpha_j\alpha_k\alpha_l &= b_{1111}\left({\alpha_1}^4 + {\alpha_2}^4 + {\alpha_3}^4\right) \\ &\quad + 6b_{1122}\left({\alpha_1}^2{\alpha_2}^2 + {\alpha_1}^2{\alpha_3}^2 + {\alpha_2}^2{\alpha_3}^2\right), \end{aligned} \tag{4.6}$$

and similarly the sixth order term

$$\sum_{ijklmn} b_{ijklmn}\alpha_i\alpha_j\alpha_k\alpha_l\alpha_m\alpha_n = b_{111111}\left({\alpha_1}^6+{\alpha_2}^6+{\alpha_3}^6\right)+15b_{111122} \times\left({\alpha_1}^2{\alpha_2}^4+{\alpha_1}^4{\alpha_2}^2+{\alpha_1}^2{\alpha_3}^4+{\alpha_1}^4{\alpha_3}^2 +{\alpha_2}^2{\alpha_3}^4+{\alpha_2}^4{\alpha_3}^2\right) +90b_{112233}{\alpha_1}^2{\alpha_2}^2{\alpha_3}^2. \tag{4.7}$$

Inserting Eqs. (4.5), (4.6), and (4.7) in Eq. (4.2) gives an energy density for cubic systems:

$$\begin{aligned}E_{crys}^{cubic} = {} & E_0+b_{11}+b_{1111}\left({\alpha_1}^4+{\alpha_2}^4+{\alpha_3}^4\right)\\ & +6b_{1122}\left({\alpha_1}^2{\alpha_2}^2+{\alpha_1}^2{\alpha_3}^2+{\alpha_2}^2{\alpha_3}^2\right)\\ & +b_{111111}\left({\alpha_1}^6+{\alpha_2}^6+{\alpha_3}^6\right)+90b_{112233}{\alpha_1}^2{\alpha_2}^2{\alpha_3}^2\\ & +15b_{111122}\left({\alpha_1}^2{\alpha_2}^4+{\alpha_1}^4{\alpha_2}^2+{\alpha_1}^2{\alpha_3}^4\right.\\ & \left.+{\alpha_1}^4{\alpha_3}^2+{\alpha_2}^2{\alpha_3}^4+{\alpha_2}^4{\alpha_3}^2\right).\end{aligned} \tag{4.8}$$

In order to reduce this several expressions derived from the normalization condition for the directional cosines are employed. For the second and third order one has: [10, p. 92]

$$\begin{aligned}1 &= \left({\alpha_1}^2+{\alpha_2}^2+{\alpha_3}^2\right)^2\\ &= {\alpha_1}^4+{\alpha_2}^4+{\alpha_3}^4+2\left({\alpha_1}^2{\alpha_2}^2+{\alpha_1}^2{\alpha_3}^2+{\alpha_2}^2{\alpha_3}^2\right)\\ 1 &= \left({\alpha_1}^2+{\alpha_2}^2+{\alpha_3}^2\right)^3\\ &= {\alpha_1}^6+{\alpha_2}^6+{\alpha_3}^6+6{\alpha_1}^2{\alpha_2}^2{\alpha_3}^2\\ &\quad +3\left({\alpha_1}^4{\alpha_2}^2+{\alpha_1}^2{\alpha_2}^4+{\alpha_1}^4{\alpha_3}^2+{\alpha_1}^2{\alpha_3}^4+{\alpha_2}^4{\alpha_3}^2+{\alpha_2}^2{\alpha_3}^4\right),\end{aligned}$$

which allows for a reduction of the ${\alpha_1}^4+{\alpha_2}^4+{\alpha_3}^4$ and ${\alpha_1}^6+{\alpha_2}^6+{\alpha_3}^6$ terms. In order to eliminate the terms mixing second and fourth order it is multiplied with e.g. ${\alpha_1}^2{\alpha_2}^2$ to get

$$\begin{aligned}{\alpha_1}^2{\alpha_2}^2 &= {\alpha_1}^4{\alpha_2}^2+{\alpha_1}^2{\alpha_2}^4+{\alpha_1}^2{\alpha_2}^2{\alpha_3}^2\\ {\alpha_1}^4{\alpha_2}^2+{\alpha_1}^2{\alpha_2}^4 &= {\alpha_1}^2{\alpha_2}^2-{\alpha_1}^2{\alpha_2}^2{\alpha_3}^2.\end{aligned}$$

Using these expressions Eq. (4.8) reduces to:

$$\begin{aligned}E_{crys}^{cubic} &= E_0+b_{11}+b_{1111}+b_{111111}+\left(6b_{1122}-2b_{1111}\right.\\ &\quad \left.+15b_{111122}-3b_{111111}\right)\left({\alpha_1}^2{\alpha_2}^2+{\alpha_1}^2{\alpha_3}^2+{\alpha_2}^2{\alpha_3}^2\right)\\ &\quad \left(90b_{112233}-6b_{1111}-45b_{111122}+9b_{111111}\right){\alpha_1}^2{\alpha_2}^2{\alpha_3}^2\\ &= K_0+K_1\left({\alpha_1}^2{\alpha_2}^2+{\alpha_1}^2{\alpha_3}^2+{\alpha_2}^2{\alpha_3}^2\right)+K_2{\alpha_1}^2{\alpha_2}^2{\alpha_3}^2,\end{aligned} \tag{4.9}$$

where the K_i are the so-called magneto crystalline anisotropy constants, which are functions of the b coefficients.

Tetragonal and Hexagonal Systems

In tetragonal systems the cross terms vanish as well due to Eq. (4.1), but the symmetry only makes two indices indistinguishable. Hence the second order term reduces to: [10, p. 92-93]

$$\begin{aligned}\sum_{ij} b_{ij}\alpha_i\alpha_j &= b_{11}{\alpha_1}^2 + b_{11}{\alpha_2}^2 + b_{33}{\alpha_3}^2 \\ &= b_{11} + \Big(b_{33} - b_{11}\Big){\alpha_3}^2 \\ &= a_0 + a_1{\alpha_3}^2,\end{aligned}$$

which is obtained using the normalization condition of the directional cosines Eq. (B.2). Additionally the coefficients a_i, which are functions of b_{ij}, are introduced.

The fourth order term amounts to:

$$\begin{aligned}\sum_{ijkl} b_{ijkl}\alpha_i\alpha_j\alpha_k\alpha_l &= b_{1111}\Big({\alpha_1}^4 + {\alpha_2}^4\Big) + b_{3333}{\alpha_3}^4 + 6b_{1122}{\alpha_1}^2{\alpha_2}^2 \\ &\quad + 12b_{1133}{\alpha_3}^2\Big({\alpha_1}^2 + {\alpha_2}^2\Big) \\ &= b_{1111}\Big({\alpha_1}^4 + {\alpha_2}^4\Big) + \Big(b_{3333} + 12b_{1133}\Big){\alpha_3}^4 \\ &\quad + 6b_{1122}{\alpha_1}^2{\alpha_2}^2 - 12b_{1133}{\alpha_3}^4.\end{aligned}$$

Inserting these in Eq. (4.2) yields: [10, p.93]

$$\begin{aligned}E_{crys}^{tetra} &= a_0 + a_1{\alpha_3}^2 + b_{1111}\Big({\alpha_1}^4 + {\alpha_2}^4\Big) + \Big(b_{3333} + 12b_{1133}\Big){\alpha_3}^4 \\ &\quad + 6b_{1122}{\alpha_1}^2{\alpha_2}^2 - 12b_{1133}{\alpha_3}^4 \\ &= K_0 + K_1\alpha 3^2 + K_2\alpha 3^4 + K_3\Big({\alpha_1}^4 + {\alpha_2}^4\Big) + K_4{\alpha_1}^2{\alpha_2}^2,\end{aligned} \tag{4.10}$$

where the magneto crystalline anisotropy constants K_i are introduced again.

For systems with hexagonal symmetry analogeous considerations lead to the expression: [10, p.93]

$$\begin{aligned}E_{crys}^{hex} &= K_0 + K_1\Big({\alpha_1}^2 + {\alpha_2}^2\Big) + K_2\Big({\alpha_1}^2 + {\alpha_2}^2\Big)^2 \\ &\quad + K_3\Big({\alpha_1}^2 + {\alpha_2}^2\Big)^3 + K_4\Big({\alpha_1}^2 - {\alpha_2}^2\Big)\Big({\alpha_1}^4 + {\alpha_2}^4 - 14{\alpha_1}^2{\alpha_2}^2\Big).\end{aligned} \tag{4.11}$$

Replacing the directional cosines in Eqs. (4.10) and (4.11) yields for E_{crys}^{tetra}:

$$\begin{aligned}
E_{crys}^{tetra} \approx & K_0 + K_1 \cos^2\theta + K_2 \cos^4\theta + K_3 \sin^4\theta \Big(\cos^4\phi + \sin^4\phi \Big) \\
= & K_0 + K_1 \Big(1 - \sin^2\phi \Big) + K_2 \Big(\sin^4\theta + \cos 2\theta \Big) \\
& + K_3 \sin^4\theta \Big(\frac{3 + 4\cos 2\phi + \cos 4\phi}{8} + \frac{3 - 4\cos 2\phi + \cos 4\phi}{8} \Big) \\
= & K_0 + K_1 \Big(1 - \sin^2\phi \Big) + K_2 \Big(\sin^4\theta + 1 - 2\sin^2\theta \Big) \\
& + K_3 \sin^4\theta \Big(\frac{3}{4} + \frac{\cos 4\phi}{4} \Big) \\
= & K_0' + K_1' \sin^2\theta + K_2' \sin^4\theta + K_3' \sin^4\theta \cos 4\phi, \qquad (4.12)
\end{aligned}$$

using the trigonometric identities:

$$\begin{aligned}
\cos nx &= 2\cos x \cos\Big(n-1\Big)x - \cos\Big(n-2\Big)x \\
\sin^4 x &= \frac{3 - 4\cos 2\phi + \cos 4\phi}{8} \\
\cos^4 x &= \frac{3 + 4\cos 2\phi + \cos 4\phi}{8}.
\end{aligned}$$

Similarly one may obtain for E_{crys}^{hex}:

$$\begin{aligned}
E_{crys}^{hex} = & K_0 + K_1 \sin^2\theta + K_2 \sin^4\theta + K_3 \sin^6\theta \\
& + K_4 \sin^6\theta \Big(\cos^6\phi - \sin^6\phi - 15\cos^4\phi \sin^2\phi \\
& + 15\cos^2\phi \sin^4\phi \Big) \\
= & K_0 + K_1 \sin^2\theta + K_2 \sin^4\theta + K_3 \sin^6\theta + K_4 \sin^6\theta \cos 6\phi. \qquad (4.13)
\end{aligned}$$

The deriviation of Eq. (4.13) is seen in full extent in App. B.

The terms with $\cos 4\phi$ and $\cos 6\phi$ reflect the symmetry of the basal planes, which is four- and sixfold for tetragonal and hexagonal lattices respectively. In practice only terms up to K_2 are required to obtain resonable agreement. If only these terms are considered the two expressions Eqs. (4.12) and (4.13) are identical and only depend on θ, and hence exhibit a uniaxial symmetry.

4.1.2 Magnetization Axes

Now the energy density of different crystallagraphic systems is described by the magneto crystalline anisotropy constants, which depend on material and temperature. From experience it is sufficient only to consider the constants K_1 and K_2 to achieve good agreement between experiments and calculations. Using the expressions found the easy and hard magnetization axes are determined by replacing the directional cosines with the expressions in Eq. (B.1) and inserting values of θ and ϕ for the crystal directions. [10, p. 94]

For the cubic crystals the [100], [110], and [111] directions are used as an example. These have the angles $\theta = 90^\circ$ $\phi = 0^\circ$, $\theta = 90^\circ$ $\phi = 45^\circ$, and $\theta = 54.70^\circ$ $\phi = 45^\circ$ respectively. This results in the following values of the directional cosines:

$$[100] : \alpha_1 = 1, \alpha_2 = \alpha_3 = 0$$
$$[110] : \alpha_1 = \alpha_2 = \frac{1}{\sqrt{2}}, \alpha_3 = 0$$
$$[111] : \alpha_1 = \alpha_2 = \alpha_3 = \frac{1}{\sqrt{3}}.$$

Inserting these into Eq. (4.9) yields:

$$E_{[100]} = K_0$$
$$E_{[110]} = K_0 + \frac{1}{4}K_1$$
$$E_{[111]} = K_0 + \frac{1}{3}K_1 + \frac{1}{27}K_2.$$

K_0 contributes equally in all expressions and is hence irrellevant in determining the lowest energy. If both K_1 and K_2 are positive $E_{[100]}$ is the lowest of the three. This is also the case if only K_1 is positive if K_2 then lies between $-\frac{9}{4}K_1$ and $-9K_1$. The easy, medium, and hard axis at different values of the magneto crystalline anisotropy constants are given in Table 4.1.

K_1	K_2	Easy axis	Medium axis	Hard axis
+	$+\infty\ to\ -\frac{9}{4}K_1$	100	110	111
+	$-\frac{9}{4}K_1\ to\ -9K_1$	100	111	110
+	$-9K_1\ to\ -\infty$	111	100	110
−	$-\infty\ to\ \frac{9}{4}\lvert K_1\rvert$	111	110	100
−	$\frac{9}{4}\lvert K_1\rvert\ to\ 9\lvert K_1\rvert$	110	111	100
−	$9\lvert K_1\rvert\ to\ +\infty$	110	100	111

Table 4.1: Easy, medium, and hard magnetizations axes of cubic systems for different values of the magneto crystalline anisotropy constants K_1 and K_2. From [10, p. 96]

To illustrate in which direction the magnetization is easy an energy surface is plotted in Figure 4.1.
For tetragonal and hexagonal systems the magnetizations axes are evaluated by considering the expression

$$E_{crys} = K_0 + K_1 \sin^2\theta + K_2 \sin^4\theta,$$

where if only values of the magneto crystalline anisotropy constants up to K_2 are considered in the expressions Eqs. (4.10) and (4.11). The energy density of these systems depend only on the angle θ relative to the basal plane. For positive values of both K_1 and K_2 the minimum energy is when $\theta = 0$, and hence the [0001]-direction

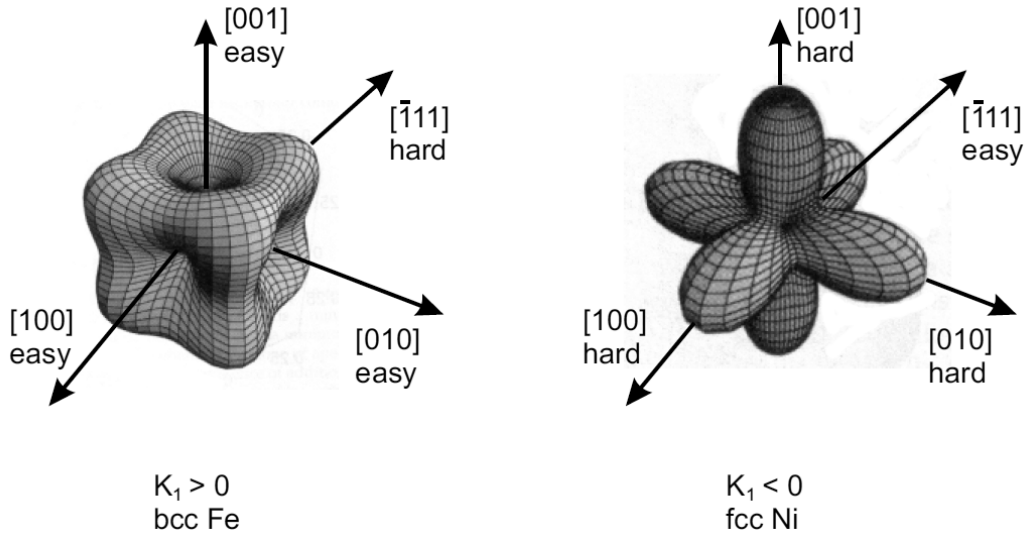

Figure 4.1: Energy surface for the anisotropy of cubic systems. On the left: bcc Fe with a positive K_1. On the right: fcc Ni with a negative K_1. The arrows indicate the easy and hard magnetization axes. The figure is from [10, p.95].

is the easy axis. If both are negative the easy axis lies in the $[0001]$-plane, and the $[0001]$-direction becomes the hard axis. These cases are illustrated using energy surface plots in Figure 4.2.

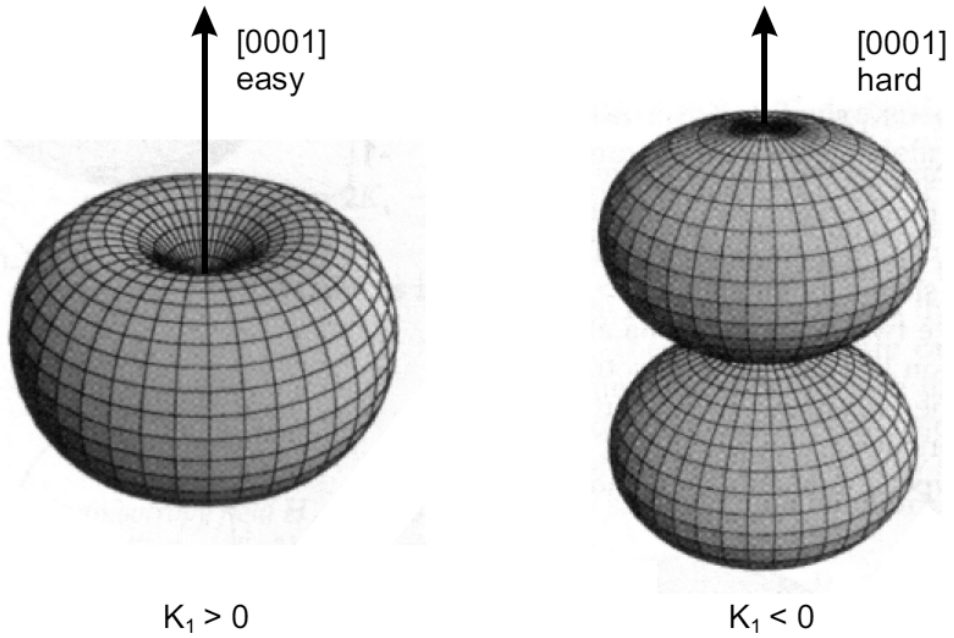

Figure 4.2: Energy surface for the anisotropy of uniaxial systems. On the left K_1 is positive and the easy magnetization axis is perpendicular to the basal plane. To the left K_2 is negative and the easy magnetization axis lies within the basal plane. The figure is from [10, p.97].

The values of K_1 and K_2 for Fe, Ni, and Co are given in Table 4.2.

		bcc-Fe	fcc-Ni	hcp-Co
K_1	$[\frac{J}{m^3}]$	$5.48 \cdot 10^4$	$-12.63 \cdot 10^4$	$7.66 \cdot 10^5$
	$[\frac{eV}{atom}]$	$4.02 \cdot 10^{-6}$	$-8.63 \cdot 10^{-6}$	$5.33 \cdot 10^{-5}$
K_2	$[\frac{J}{m^3}]$	$1.96 \cdot 10^2$	$5.78 \cdot 10^4$	$1.05 \cdot 10^5$
	$[\frac{eV}{atom}]$	$1.44 \cdot 10^{-8}$	$3.95 \cdot 10^{-6}$	$7.31 \cdot 10^{-6}$
K_3	$[\frac{J}{m^3}]$	$0.9 \cdot 10^2$	$3.48 \cdot 10^3$	-
	$[\frac{eV}{atom}]$	$6.6 \cdot 10^{-9}$	$2.38 \cdot 10^{-7}$	-

Table 4.2: Magneto crystalline anisotropy constants K_1, K_2, and K_3 for Fe, Ni, and Co at $T = 4.2K$. From [10, p. 95]

4.1.3 Shape Anisotropy

A polycrystalline sample with no specific orientation of the domains have no magneto crystalline anisotropy, hence one might expect no preferred direction of the magnetization. This is however only true when the sample is spherical. Otherwise a preferred orientaion arises as a result of the shape of the sample. The phenomenon is called shape anisotropy, and occurs as a result of the stray field of the sample.

In an infinite system $\vec{B} = \mu_0\left(\vec{H} + \vec{M}\right)$, but in reality a sample is finite and exhibits poles on the surface causing a stray field outside of the sample. This leads to a demagnetizing field inside the sample. [10, p. 103]

The energy of a sample in its own stray field is given by: [10, p. 103]

$$E_{stray} = -\frac{1}{2}\int \mu_0 \vec{M} \cdot \vec{H}_{demag} dV, \tag{4.14}$$

where $\vec{H}_{demag}$ is the demagnetization field inside the sample. This is related to the magnetization via:

$$\vec{H}_{demag} = -\overline{\overline{N}}\vec{M}, \tag{4.15}$$

where $\overline{\overline{N}}$ is the demagnetizing tensor. If $\overline{\overline{N}}$ is diagonal then the trace[1] is unity, i.e.

$$tr\left(\overline{\overline{N}}\right) = 1.$$

[1] The trace of an $n \times n$ matrix is the sum of the elements on the main diagonal, i.e. $tr\left(\vec{M}\right) = \sum M_{ii}$.

Inserting Eq. (4.15) in Eq. (4.14) yields:

$$\begin{aligned} E_{stray} &= \frac{1}{2}\mu_0 \int \vec{M}\overline{\overline{N}}\vec{M}dV \\ &= \frac{1}{2}V\mu_0\vec{M}\overline{\overline{N}}\vec{M}. \end{aligned}$$

If the simple case of an ellipsoide is considered then $\overline{\overline{N}}$ is a diagonal tensor if the semiaxes a, b, and c are along the coordinate axes. For an arbitrary orientation of the magnetization characterized by the directional cosines α_a, α_b, and α_c the demagnetization tensor becomes:

$$\overline{\overline{N}} = \begin{bmatrix} N_a & 0 & 0 \\ 0 & N_b & 0 \\ 0 & 0 & N_c \end{bmatrix},$$

and the stray field energy per volume is thus:

$$E_{stray} = \frac{1}{2}\mu_0 M^2 \left(N_a\alpha_a^2 + N_b\alpha_b^2 + N_c\alpha_c^2\right).$$

If the sample is spherical $\overline{\overline{N}}$ is:

$$\overline{\overline{N}} = \begin{bmatrix} \frac{1}{3} & 0 & 0 \\ 0 & \frac{1}{3} & 0 \\ 0 & 0 & \frac{1}{3} \end{bmatrix},$$

which leads to a stray field energy density of:

$$\begin{aligned} E_{stray} &= \frac{1}{2}\mu_0 M^2 \frac{1}{3}\left(\alpha_a^2 + \alpha_b^2 + \alpha_c^2\right) \\ &= \frac{1}{6}\mu_0 M^2, \end{aligned}$$

using Eq. (B.2). This expression is independent of all directional cosines, and hence isotropic. This is however only the case for a sphere.

If instead a spheroid is considered the elements of $\overline{\overline{N}}$ become $N_a = N_b$ and $N_c = 1 - 2N_a$, as the semi-minor axes a and b are of the same lenght. If the angle between the magnetization and the semi-major axis c is denoted θ the stray field energy density amounts to:

$$\begin{aligned} E_{stray} &= \frac{1}{2}\mu_0 M^2 \left(N_a\alpha_a^2 + N_a\alpha_b^2 + \left(1 - 2N_a\right)\alpha_c^2\right) \\ &= \frac{1}{2}\mu_0 M^2 \left(N_a + \left(1 - 3N_a\right)\cos^2\theta\right). \end{aligned}$$

Similar considerations can be employed to an infinitely long cylinder. Here $a = b$ and $c = \infty$, which leads to:

$$\overline{\overline{N}} = \begin{bmatrix} \frac{1}{2} & 0 & 0 \\ 0 & \frac{1}{2} & 0 \\ 0 & 0 & 0 \end{bmatrix},$$

and hence a stray field energy density of:

$$E_{stray} = \frac{1}{2}\mu_0 M^2 \left(\frac{1}{2}\alpha_a^2 + \frac{1}{2}\alpha_b^2\right) = \frac{1}{4}\mu_0 M^2 \sin^2\theta.$$

In the case of an infinitely expanded thin plate $a = b = \infty$, and

$$\overline{\overline{N}} = \begin{bmatrix} 0 & 0 & 0 \\ 0 & 0 & 0 \\ 0 & 0 & 1 \end{bmatrix},$$

with a stray field energy density of:

$$E_{stray} = \frac{1}{2}\mu_0 M^2 \cos^2\theta.$$

This example is nearly congruent with a thin film, and as such it is important when considering thin magnetic film structures. The equation is rewritten by introducing shape anisotropy constants analogously to the magneto crystalline case:

$$E_{stray} = K_0 + K_{shape}^V \sin^2\theta, \tag{4.16}$$

with $K_{shape}^V \propto -M^2 < 0$.

The stray field energy has a minimum when $\theta = 90°$, i.e. when the magnetization is in the plane of the film. In table 4.3 values of K_{shape}^V are listed for Fe, Ni, and Co. By comparison with values of K_1 from table 4.2 it is seen that $K_{shape}^V > K_1$, and hence shape anisotropy dominates the magneto crystalline anisotropy. Accordingly in thin film systems an in-plane magnetization is favoured.

	$bcc-Fe$	$fcc-Ni$	$hcp-Co$
$[\frac{J}{m^3}]$	$1.92 \cdot 10^6$	$1.73 \cdot 10^5$	$1.34 \cdot 10^6$
$[\frac{eV}{atom}]$	$1.41 \cdot 10^{-4}$	$1.28 \cdot 10^{-5}$	$9.31 \cdot 10^{-5}$

Table 4.3: Shape anisotropy constant K_{shape}^V for Fe, Ni, and Co. From [10, p. 105]

4.2 Magnetism in Thin Films

The considerations made so far are only valid when the effects of surfaces and interfaces are neglegted. This is naturally incorrect as the magnetic moments interact with a substrate at an interface reducing the magntization. At a surface on the other hand the magnetization is increased due to a more atomic-like behavior. When these

effects are taken into account the reduced symmetry allows for more terms to contribute. All effective anisotropy constants thus consist of a volume and a surface contribution:

$$K^{eff} = K^V + \frac{2K^S}{d}, \tag{4.17}$$

where the factor of 2 arise from the creation of 2 surfaces. The surface contribution exhibits an inverse relation with the thickness of the material, hence it only need to be considered for thin films. If Eq. (4.17) is multiplied with d a plot of $d \cdot K^{eff}(d)$ allows for a determination of K^V as the slope, and K^S as the zero-crossing. In thin films the shape anisotropy is as a result of Eq. (4.16) dominant in the volume contribution, hence K^V is negative. A positive value of K^S therefore leads to a crossing of the first axis at a value d_c, the so-called critical thickness:

$$d_c = -\frac{2K^S}{K^V}$$

At this thickness the magnetization changes between in-plane and perpendicular. So in very thin films the magnetization will be perpendicualar and if the thickness is increased it will shift in a so-called spin reorientation transition to being in-plane when the critical thickness is reached. This is illustrated in Figure 4.3 with an example of *Co* on *Pd*.

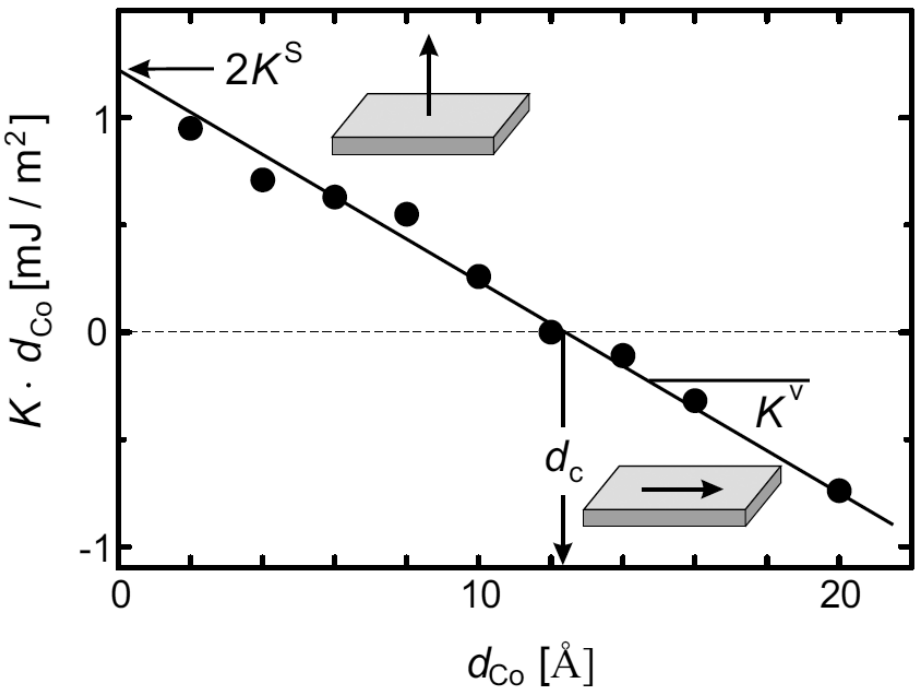

Figure 4.3: Below a critical film thickness, d_c, the effect of the surfaces dominate and makes an perpendicular magnetization preferable. When the thickness is increased to a value above d_c the preferred orientation changes to in-plane. The values of K^V and K^S are determined from the slope and the zero crosing of the line. Illustration is from [10, p. 113]

In a thin film quantum well states arise due to the limitation of the film thickness, and converge to bulk as the thickness is increased. In a ferromagnetic thin film these quantum well states acts as a spin filter so electrons are either confined in the film or strongly reflected depending on their spin orientation relative to the magnetization.

If a magnetic thin film is capped by a nonmagnetic layer the magnetization is reduced both in the topmost layer as the magnetic moments of the surface atoms are restricted, and in the subsequent layers as a result of the hybridisation of the orbitals.

Magneto-Optic Kerr Effect

5

This chapter contains the theoretical definition of the magneto-optic kerr effect. Initially the magneto-optic effect is introduced followed by establishig a model for the propagation of light in a magnetic multilayer structure. Finally the Kerr angle is derived and a basic setup which utilizes the effect to measure hysterisis loops of metallic surface structures is presented.

5.1 Magneto-Optic Effect

Conceptually the magneto-optic effect can be described in several ways. One may take a macroscopical point of view and ascribe the effect to the antisymmetric off-diagonal elements of the dielectric tensor. However, for the full explanation one must use quantum mechanics and explain the effect through a coupling between the electrical field of the light and the spin of the electron, commonly referred to as the spin-orbit interaction. Intially in this section the microscopical description is discussed and later on a more thorough describtion using the dielectric function is introduced.

5.1.1 Microscopical Point of View

All optical properties of a medium are governed by the dielectric tensor. In Sec. 3.3 it is described how this tensor depends on the motion of the electrons in the given medium. Based on this the concept of magneto-optic effect can be described by looking at the response of these electrons to right- and left-circularly polarized light (RCP and LCP). The reason for looking on the response to RCP and LCP is that linearly polarized light may be regarded as a superposition of RCP and LCP light.

If one only considers classical movement of electrons in a medium then in the abscense of magnetic fields all motion is induced by the incident light beam. Based on this it is clear that a RCP beam drives the electrons into a right circular motion and vice versa for LCP light. The radius of the electron orbit remains the same in spite of rotation direction, and accordingly the dipole moment is the same, see Sec. 3.2. From Sec. 3.3 this indicates that no Faraday rotation will occur.

By staying in the same classical scope but applying an external magnetic field parallel to the propagation direction of the beam, an additional contribution to the Lorentz force is gained:

$$\vec{F} = q\left[\vec{E} + \left(\vec{v} \times \vec{B}\right)\right],$$

where $\vec{F}$ is the Lorentz force, q is the charge and $\vec{v}$ is the instantaneous velocity of the particle affected. From the definition of Lorentz force it is clear that electrons in a left circular motion experiences an addional force pointing towards the center of the circle and vice versa for electrons in a right circular motion. Therefore two different dipole moments are present and accordingly two different dielectric constants. Based on this one may conclude it is the external magnetic field which generates the Faraday effect in the classical situation.

However, in reality one observes larger degrees of rotation in ferromagnetic materials than in e.g. nonmagnetic materials. This cannot be accounted for in classical mechanics. Instead the concept of exchange interactions defined in Sec. 3.2.4 and the spin-orbit coupling delivers the correct explanation. The spin-orbit coupling originates from the electron spin and the magnetic field affecting the electron as it propagates in the electric field $-\Delta V$ with momentum $\vec{p}$:

$$SO_{coupling} \propto (\Delta V \times \vec{p}) \cdot \vec{s}.$$

This interaction couples the electrons magnetic moment with its motion and thereby connects the magnetic and optical properties of a given medium. In ferromagnets this gives rise to a large magneto-optic effect whereas in nonmagnetic materials the effect is negligible. Further investigation into the subject is beyond the scope of this project. Instead the interaction between electromagnetic radiation and a medium is considered using the dielectric tensor in the following section.

5.2 Magnetic Multilayers

A reasonable description of SMOKE can be derived by analysing the dielectric properties of a given medium, refer to Sec. 3.3. In the following section this is done by considering light incident on a multilayer structure of N layers with arbitrary magnetic properties.[25] [33] [32]

Linearly polarized light may be considered as a superposition of RCP and LCP light. Generally when light propagates in a medium a change of phase and absorption of light occur. Accordingly, the two waves, the RCP and the LCP, experience different changes to their phase resulting in a rotation of the polarization plane. Furthermore, the ellipticity of the two waves changes due to the different absorption coefficients they experience.

In general the dielectric tensor can always be divided into a symmetric and antisymmetric part. As discussed in Sec. 3.3 it is always possible to orientate the coordinate system so that the symmetric tensor becomes diaganolized. As mentioned before this does not give rise to a Faraday rotation and therefore it is unimportant in the present context. Considering the following dielectric tensor:

$$\tilde{\varepsilon} = \varepsilon \begin{bmatrix} 1 & iQ_z & -iQ_y \\ -iQ_z & 1 & iQ_x \\ iQ_y & -iQ_x & 1 \end{bmatrix}, \tag{5.1}$$

where $n = \sqrt{\varepsilon}$ is the average index of refraction and $\vec{Q}$ is the so-called Voigt vector. The components of the Voigt vector is the magneto-optic constants of the three

possible directions. If only one such exists, the vector reduces to a constant Q. [25] [33]

Determining the dielectric tensor enables the evaluation of the Maxwell equations in any given multilayer structure, as was described in Sec. 3.3. In Jones matrix[1] formulation the complete interaction between a given number of layers and an incident beam can be described using two matrices $\overline{\overline{A}}$ and $\overline{\overline{D}}$. $\overline{\overline{A}}$ and $\overline{\overline{D}}$ are 4×4 matrices and they are in the following referred to as the medium boundary matrix and the propagation matrix. Naturally these matrices are determined from material properties, and thereby using the dielectric tensor from Eq. (5.1).

The medium boundary matrix couples the tangential components of the fields inside the medium with the s- and p-components of the incident electromagnetic radiation:

$$\overline{\overline{F}} = \overline{\overline{A}}\,\vec{P}$$

where $\vec{F}$ and $\vec{P}$ are 4×1 vectors. $\vec{F}$ contains all relevant field components

$$\vec{F} = \begin{bmatrix} E_x \\ E_y \\ H_x \\ H_y \end{bmatrix},$$

and $\vec{P}$ describes all electromagnetic radiation in a given medium, which consists of two in- and outgoing components:

$$\vec{P} = \begin{bmatrix} E_s^i \\ E_p^i \\ E_s^r \\ E_p^r \end{bmatrix}.$$

Based on this, it is simple to formulate the boundary matching conditions as:

$$\overline{\overline{A}}_1 \vec{P}_1 = \overline{\overline{A}}_2 \vec{P}_2. \tag{5.2}$$

Eq. (5.2) is valid only for single boundary problems, with multilayer structures any phase change happening during propagation between media needs to be addressed. The propagation matrix handles this change in the p- and s-components as a function of propagation depth in the given medium. If $\vec{P}_2(0)$ is known, then $\vec{P}_2(z)$ is formulated as:

$$\vec{P}_2(0) = \overline{\overline{D}}_2(z)\vec{P}_2(z). \tag{5.3}$$

From Eqs. (5.2) and (5.3) it is clear that with well defined matrices all optical problems of the layered structure can be handled.

Considering the case illustrated in Figure 5.1(a), which is light incident on a surface of N layers. The geometrical optical situation is shown in Figure 5.1(b).

[1] A notation where the field components are separated and displayed in a vector. Accordingly quantities affecting the fields are displayed in matrices, e.g. transmission and reflection coefficients.

Apart from the boundary between the last and the second last medium the schematic is valid for all the transitions. Naturally no light is incident from the final medium f.

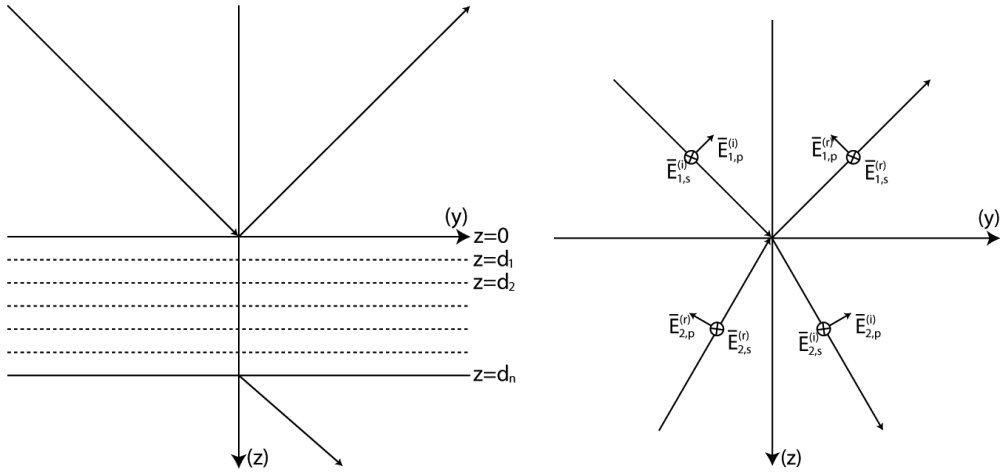

(a) Schematic of light incident upon a multilayer structure.

(b) Two media separated by the xy-plane. Light is incident along the z-direction.

Figure 5.1: Schematics concerning the propagation of light in a multilayer structure. Initially light is incident, and after multiple reflections between the different layers, light is reflected back into the initial medium. Figure 5.1(a) displays the final result with light reflected back into the initial medium and absorbed in the final medium. Figure 5.1(b) displays the geometrical optics around the boundary between two of the layers. Inspired from [25] and [33].

If $\vec{P}_i$ denotes the incident and reflected light from outside of the layered structure it follows from Eqs. (5.2) and (5.3) that:

$$\begin{aligned}\overline{\overline{A}}_i\vec{P}_i &= \overline{\overline{A}}_1\overline{\overline{D}}_1\vec{P}_1 \\ &= \overline{\overline{A}}_1\overline{\overline{D}}_1\overline{\overline{A}}_1^{-1}\overline{\overline{A}}_1\vec{P}_1 \\ &= \overline{\overline{A}}_1\overline{\overline{D}}_1\overline{\overline{A}}_1^{-1}\overline{\overline{A}}_2\overline{\overline{D}}_2\vec{P}_2. \end{aligned} \tag{5.4}$$

It is clear that the line of calculations in Eq. (5.4) can be continued until the last layer N:

$$\overline{\overline{A}}_i\vec{P}_i = \prod_{m=1}^{N}\left\{\overline{\overline{A}}_m\overline{\overline{D}}_m\overline{\overline{A}}_m^{-1}\right\}\overline{\overline{A}}_f\vec{P}_f. \tag{5.5}$$

By rearranging Eq. (5.5) to the form

$$\vec{P}_i = \overline{\overline{T}}\vec{P}_f, \tag{5.6}$$

a new tensor $\overline{\overline{T}}$ is defined as

$$\overline{\overline{T}} = \overline{\overline{A}}_i^{-1}\prod_{m=1}^{N}\left\{\overline{\overline{A}}_m\overline{\overline{D}}_m\overline{\overline{A}}_m^{-1}\right\}\overline{\overline{A}}_f. \tag{5.7}$$

Eqs. (5.6) and (5.7) present a generalized way to calculate the exact reflected field components for any type of layered structure. One just have to calculate the exact medium boundary matrix and propagation matrix. This has been done in detail in numerous works, but is beyond the scope of this project. The interior of the multiplication in Eq. (5.7) represents the intermediate layers of the structure, while the first and last term represents the initial and final media respectively. [25] [33] [32]

In the following section the Kerr angle is formally defined, but for now we merely accept that

$$\phi_p = \phi'_p + i\phi''_p = \frac{E_p^{(r)}}{E_s^{(r)}}$$
$$\phi_s = \phi'_s + i\phi''_s = \frac{E_s^{(r)}}{E_p^{(r)}},$$

where ϕ_p and ϕ_s are the Kerr angles for p- and s-polarized light respectively. By introducing the formal definitions of the medium average fresnel reflection coefficients:

$$r_{ss} = \frac{E_{1,s}^{(r)}}{E_{1,s}^{(i)}} \qquad r_{pp} = \frac{E_{1,p}^{(r)}}{E_{1,p}^{(i)}}$$
$$r_{sp} = \frac{E_{1,s}^{(r)}}{E_{1,p}^{(i)}} \qquad r_{ps} = \frac{E_{1,p}^{(r)}}{E_{1,s}^{(i)}}.$$

One has:

$$\phi_p = \frac{E_{1,p}^{(r)}}{E_{1,s}^{(r)}} \frac{E_{1,s}^{(i)}}{E_{1,s}^{(i)}} = \frac{r_{ps}}{r_{ss}} \tag{5.8a}$$

$$\phi_s = \frac{E_s^{(r)}}{E_p^{(r)}} \frac{E_{1,p}^{(i)}}{E_{1,p}^{(i)}} = \frac{r_{sp}}{r_{pp}}. \tag{5.8b}$$

So by calculating the four fresnel reflection coefficients of the multilayer structure one may derive an expression for the Kerr angle. In the ultrathin limit where the total thickness of the layers is much smaller than the wavelength of the light, $\sum_i d_i << \lambda$, the calculation is significantly simplified. Furthermore, if the initial and final media are nonmagnetic, the coefficients are given as: [25]

$$r_{ss} = \frac{n_i \cos\theta_i - n_f \cos\theta_f}{n_i \cos\theta_i + n_f \cos\theta_f}$$
$$r_{pp} = \frac{n_f \cos\theta_i - n_i \cos\theta_f}{n_f \cos\theta_i + n_i \cos\theta_f}$$
$$r_{ps} = -\frac{4\pi}{\lambda} \frac{n_i \cos\theta_i}{\left(n_i \cos\theta_i + n_f \cos\theta_f\right)\left(n_f \cos\theta_i + n_i \cos\theta_f\right)}$$

$$\times \left(\cos\theta_f \sum_{m=1}^{N} d_m n_m^2 Q_z^{(m)} - n_f n_i \sin\theta_i \sum_{m=1}^{N} d_m Q_y^{(m)} \right)$$

$$r_{sp} = -\frac{4\pi}{\lambda} \frac{n_i \cos\theta_i}{\left(n_i \cos\theta_i + n_f \cos\theta_f\right)\left(n_f \cos\theta_i + n_i \cos\theta_f\right)}$$

$$\times \left(\cos\theta_f \sum_{m=1}^{N} d_m n_m^2 Q_z^{(m)} + n_f n_i \sin\theta_i \sum_{m=1}^{N} d_m Q_y^{(m)} \right),$$

where n_i and n_f are the refractive indices of the initial and final media and θ_i and θ_f are the propagation angles. The way r_{ps} and r_{sp} are formulated clearly indicates a basis for an additivity law in the ultrathin limit. Each of the different multilayers contribute solely through these cross polarization fresnel reflection coefficients. They do so in the same manner through the summations. By comparing this to Eqs. (5.8a) and (5.8b) it can be concluded that the total Kerr signal is in fact a summation of the Kerr signals generated by each layer. Furthermore, as these contributions are independent of each other, the Kerr signal itself is independent of any nonmagnetic layers in the multilayer structure. It needs to be noted that this additivity concept is only valid in the ultrathin limit. This is naturally clear, as the light must attenuate when the total film thickness becomes monumental. Furhermore, this model does not take into account any surface irregularities that may arrise in the ultrathin limit.

5.3 Kerr Angle

As mentioned earlier, a setup utilizing MOKE in surface characterization (SMOKE) is simple, and in the following the basic principles are outlined.

Whenever light is reflected from the surface of any given medium the polarization is changed, apart from the special case of p- and s-polarized light. This is easily seen by describing the reflection og electromagnetic radiation from a surface using the Jones matrix formalism:

$$\vec{E}_r = \overline{\overline{R}}\vec{E}_i,$$

where

$$\overline{\overline{R}} = \begin{bmatrix} r_{pp} & 0 \\ 0 & r_{ss} \end{bmatrix}. \tag{5.9}$$

The reflection Jones matrix from Eq. (5.9) is derived from the special case of incident linearly polarized light. However, as is clear from Eq. (5.9) whenever p- or s-polarized light is incident on a surface the outgoing field only contains p- or s-polarized light respectively. By applying a magnetic field across the surface in a given direction, the effect described in Sec. 5.2 arises and even p- or s-polarized light should be rotated. This extra component of the electric field vector is used to define the quantity known as the Kerr angle ϕ. So for incident p-polarized light the Kerr angle is given by:

$$\frac{E_s^{(r)}}{E_p^{(r)}} = \phi_s = \phi_s' + i\phi_s'', \tag{5.10}$$

where ϕ_s' is the Kerr rotation and ϕ_s'' is the Kerr ellipticity.

The goal of the experimental setup is then to measure the generated field component, which in the case for p-polarized light is $E_s^{(r)}$. This could be accomplished by extinguishing the $E_p^{(r)}$ component using a linear polarizer. By approaching it this way, however, it is hard to evaluate the absolute value of the Kerr rotation or ellipticity as the signal measured in practice is the light intensity ($\propto \left|E_s^{(r)}\right|^2$). Instead the signal is measured in a small angle δ from total extinction so that:

$$\begin{aligned} I &= \left|E_p^{(r)} \sin\delta + E_s^{(r)} \cos\delta\right|^2 \\ &\approx \left|E_p^{(r)}\delta + E_s^{(r)}\right|^2, \end{aligned} \tag{5.11}$$

where it is utilized that δ is small. Combining Eqs. (5.10) and (5.11) yields:

$$\begin{aligned} I &\approx \left|E_p^{(r)}\right|^2 \left|\delta + \frac{E_s^{(r)}}{E_p^{(r)}}\right|^2 \\ &= \left|E_p^{(r)}\right|^2 \left|\delta + \phi_s' + i\phi_s''\right|^2 \\ &= \left|E_p^{(r)}\right|^2 Re\left\{\left(\delta + \phi_s' + i\phi_s''\right)^2\right\} \\ &= \left|E_p^{(r)}\right|^2 \left(\delta^2 + 2\delta\phi_s' + \phi_s'^2 - \phi_s''^2\right). \end{aligned} \tag{5.12}$$

The expression for the light intensity in Eq. (5.12) can be simplified further by considering the size of the terms. Before the polarizer it is clear that $E_s^{(r)} << E_p^{(r)}$, accordingly the Kerr rotation and ellipticity are very small values. Based on this the last two terms are left out:

$$\begin{aligned} I &\approx \left|E_p^{(r)}\right|^2 \left(\delta^2 + 2\delta\phi_s'\right) \\ &= I_0 \left(1 + \frac{2\phi_s'}{\delta}\right), \end{aligned}$$

where $I_0 = \left|E_p^{(r)}\right|^2 \delta^2$. By isolating the Kerr rotation one has an expression for the Kerr rotation:

$$\phi' = \frac{\delta}{2}\frac{I - I_0}{I_0}.$$

By measuring the reflected intensity at an angle δ from total extinction as a function of the magnetic field applied to the medium it is possible to calculate the Kerr rotation's dependence of the magnetic field. For ferromagnetic thin films this should span a hysterisis loop of a given shape.

As mentioned in the introduction of this section this concept has been used for almost three decades to record hysterisis loops of surface structures. In [17] the detection limit for transverse and polar SMOKE is investigated for a film of $0.9ML$

Co deposited on $Rh(111)$ at RT. An STM image of the surface is seen in Figure 5.2(a) and the measured Kerr rotation curve is displayed in Figure 5.2(b):

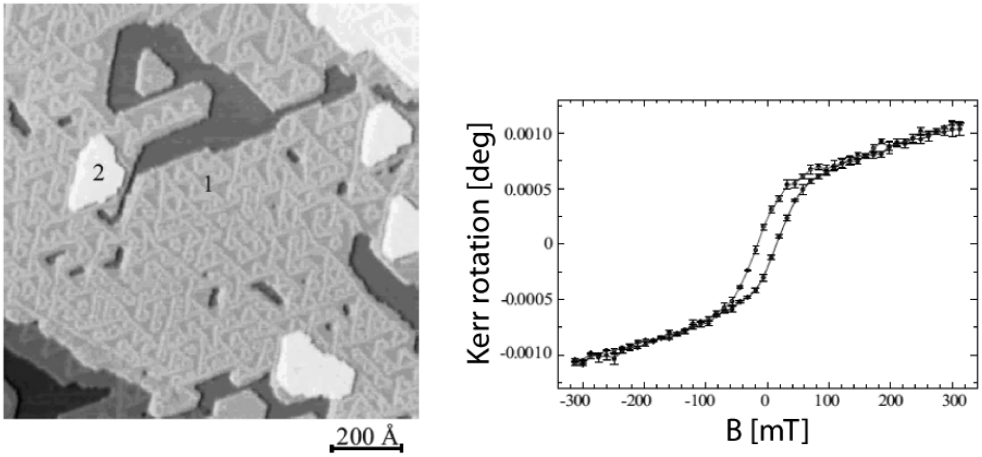

(a) STM image of $0.9ML$ of Co deposited on Rh(111) at RT.

(b) Polar kerr rotation. The curve displayed is an average of three measurements.

Figure 5.2: Two images taken from [17] which displays the usage of SMOKE in practice. In Figure 5.2(a) an STM image of the surface under consideration is displayed. In Figure 5.2(b) the Kerr rotation measured during Polar SMOKE is seen spanning a hysterisis loop with a field variation of $\pm 300mT$.

The Kerr rotation curve illustrated in Figure 5.2(b) clearly spans a hysterisis loop as expected. Furthermore the method is seen to be highly sensitive even when measuring on small coverage degrees as in [17].

5.4 Experimental SMOKE Setup

Basically only a few components are necessary when trying to construct a SMOKE setup. A light source (L), two polarizers (P), a sample (S), a detektor (D), and means of creating a magnetic field across the surface of the sample. This is illustrated in Fig. 5.3.

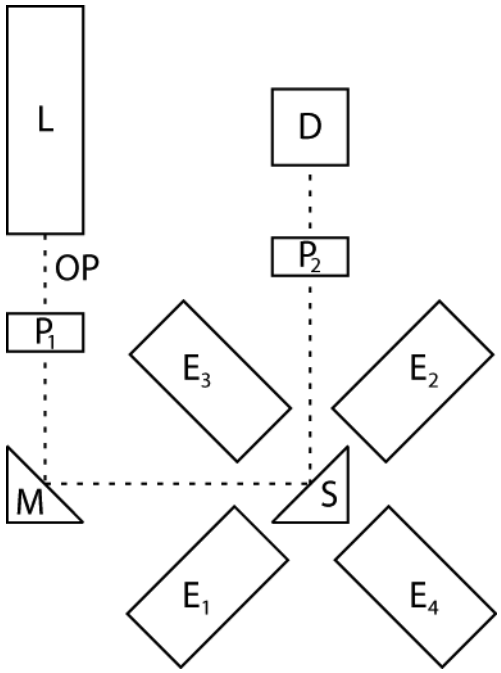

Figure 5.3: Illustration of the basic components needed for a SMOKE setup. Light source (L), polarizers (P), a sample (S), a detektor (D), and electromagnets (E). *OP* naturally denotes the optical path.

The most obvious way to create a variable magnetic field across the surface of the sample is by utilizing electromagnets. The field is easily modulated by varying the current passing through the coils of the electromagnets. Ordinarily one uses a low-power laser as a light source and polarizers with a large extinction ratio. The optical components are presented in detail in App. A.

5.4.1 Electromagnets

The demands on the electromagnets is in fact fairly comprehensive. Apart from a certain desired field strength, field homogeneity, field directions, and spatial volume are also restricted.

Naturally the electromagnets must be able to deliver a magnetic field which saturates the surface in order to measure a full hysterisis loop. In articles concerning SMOKE surfaces saturating at values below $5mT$ and above $200mT$ are seen. Generally, surfaces saturating at values between $20mT$ and a $150mT$ seems the most common case, but in order to create the most flexible setup it is decided to aim for a maximum field of atleast $200mT$. This in itself is troublesome due to the gap needed between the poles of the electromagnets, and is discussed in detail in Cha. 7. For now we merely accept that the desired electromagnet setup delivers a maximum field of $200mT$. [25] [11] [17] [16]

Field homogeneity is not as critical as in many other cases, as the area measured across should be kept below a few millimeters. However, in order to obtain

as homogeneous a field as possible the pole gap needs to be as small as possible and the core diameter needs to be as large as possible. This assumption is validated in COMSOL in one of the following sections, refer to Sec. 6.3 to see the magnetic field simulations.

Field directions play a central part of the setup, most magnetic surfaces display a large degree of anisotropy, see Sec. 4.1.1. Accordingly the surface responds differently to two fields orientated perpedicularly to each orther. With respect to the plane of the optical path (*OP*) the three directions are separated into a longitudinal, a transverse, and a polar orientation, see Figure 5.4.

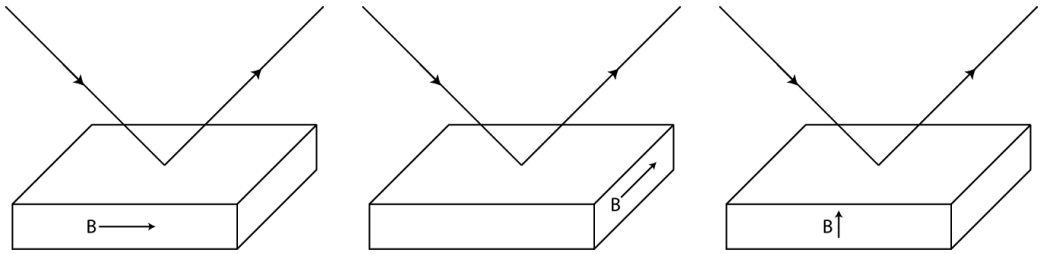

(a) Longitudinal (b) Transverse (c) Polar

Figure 5.4: Illustration of the three possible magnetic field directions with respect to the beam path, longitudinal 5.4(a), transverse 5.4(b), and polar 5.4(c). Inspired from [11]

Due to physical limitations it is almost always impossible to accommodate all three directions. Instead one could apply a magnetic field in the longitudinal and polar directions and, to some degree, investigate the last direction by rotating the polarization of light.

The spatial volume of the electromagnets is important due to numerous reasons. Eventually the setup is created around a UHV chamber in order to investigate ML thin structures and a low volume and weight simplifies e.g. the installation. The final electromagnet setup is discussed in detail in Cha. 7.

5.5 SMOKE Measurement Procedure

As discussed in Sec 5.3 measuring the intensity of the reflected light at an angle δ from total extinction enables the calculation of the Kerr rotation. The procedure used in all of the experiments throughout this project is as follows:

- Initially the electromagnets are placed in either the longitudinal or polar Kerr geometry around a given sample.
- The first polarizer, P_1 in Figure 5.3, is rotated so that either p- or s-polarized light is incident on the surface of the sample.

- By placing the second polarizer, P_2 90° of from P_1 the reflected signal should be near extinction at the detector.
- While measuring the intensity P_2 is rotated using a micrometer screw in order to find the precise angle of extinction.
- From this angle the polarizer is rotated a desired angle δ. This particular angle should be chosen so that the magneto-optic response is as large as possible compared to the noise.
- At the angle δ off total extinction the intensity is measured as a function of the current applied to the coils of the electromagnets. This current naturally generates a given magnetic field across the sample.
- From these data it is possible to calculate the Kerr rotation and the magnetic field strength so that for a ferromagnetic sample one obtains a full hysterisis loop.

Experimental Investigation of MOKE

6

In the following chapter the concept of a free air setup utilizing the magneto-optic kerr effect to characterize the magnetic properties of surface structures is pursued. This includes a characterization of the field variation around two electromagnets using a Hall probe and a finite element simulation.

6.1 Initial Considerations

Designing a setup utilizing SMOKE to characterize the magnetic properties of surface nanostructures is not trivial as small perturbations may have a large impact on the final result. Accordingly, in order to ease and optimize the design phase, a setup utilizing SMOKE is constructed in free air. Naturally, as the sample is situated outside of vacuum, the setup has limitations. But for validation of the method and characterization of the magnetic field variation around the electromagnet core the setup seems adequate.

6.2 Experimental Setup

The setup is similar to the general idea presented in Sec. 5.4, see Figure 6.1.

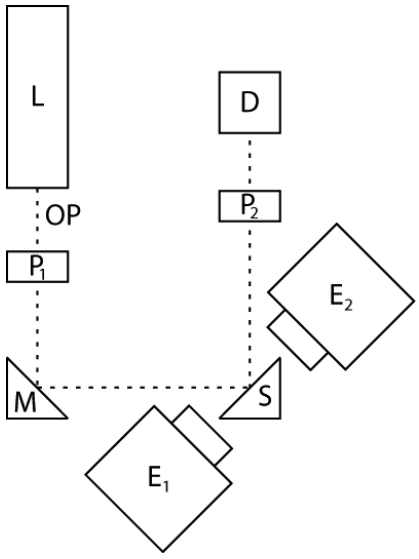

Figure 6.1: Schematic of the setup used while testing SMOKE in free air. The setup consists of a laser (*L*), two polarizers (*P*), a mirror (*M*), a sample (*S*), two electromagnets (*E*), and a detector (*D*).

The figure illustrates the relatively simple geometry used for obtaining hysterisis loops of surface structures in free air. In the figure (*OP*) signifies the optical path beginning at the laser (*L*) and ending at the detector (*D*). In between are two polarizers (*P*), a mirror (*M*) and a sample holder (*S*). To magnetize the surface two electromagnets (*E*) are used. Each consisting of an iron core with a diameter of app. 80*mm* and a length of 205*mm* and a copper coil with app. 750 windings of 2.7*mm* copper thread. The two electromagnets are placed with the smallest possible distance between the cores in order to obtain the largest, most homogeneous field possible. With a distance of 78*mm* the electromagnets produce a magnetic field of app. 60mT with a maximal current of 12A.

The equipment presented in Figure 6.1 only includes the optics and the electromagnets. Additionally electronics are needed for: data acquisition, supplying the current for the electromagnets, and for tuning the before mentioned current. The power supply used for delivering the current is a SM1540-D power supply from Delta Elektronika, a detailed description is presented in Sec. A.2.1 in App. A. It is possible to operate the power supply by manually adjusting the current or using a analogue signal. Data acquisition and applying the analog signal to the power supply is carried out with a standard PCI-9111HR DAQ card from NuDaq. A detailed description is presented in Sec. A.2.2. The electronics surrounding the optical equipment is illustrated in Figure 6.2:

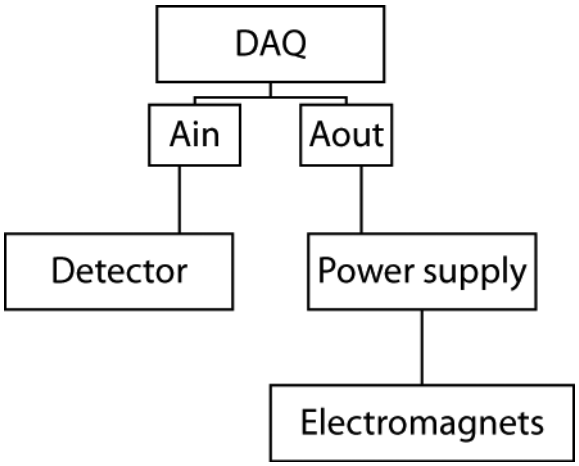

Figure 6.2: Schematic illustrating the electronics used for controlling the SMOKE setup.

Tuning the current using this setup can only deliver from 0A to 40A. However, as the current needs to be inverted to turn the magnetic field the cables connecting the power supply and the electromagnets needs to be swapped every time one wishes to cross from a positive field to a negative. This is a troublesome process when it comes repeating hysterisis loops. In a following section this is solved by introducing relays handled by the DAQ cards digital output.

6.3 Magnetic Field Variation

The surfaces considered in this project are not at all isotropic. Generally nanostructures created on top of a substrate has a minimum of two different directions namely perpendicular and parallel to the surface. Furthermore many samples of interest e.g. Co on Cu(111) displays two different directions in the plane of the substrate. As described in Sec. 5.4, the reponse from the surface depend highly on the direction of the magnetic field lines. Accordingly knowledge about the homogeneity and strength of the magnetic field from the electromagnet is essentiel.

Based on this the field strength is measured around the magnet in key positions using a Hall probe. The field homogeneity is evaluated by simulating the magnetic field from the electromagnet using a finite element method. Finally the experimental and theoretical data are compared to establish validity.

In order to simplify the measurement and simulation of the magnetic field strenght, a simplified setup of the two electromagnets is created. This is seen in Figure 6.3

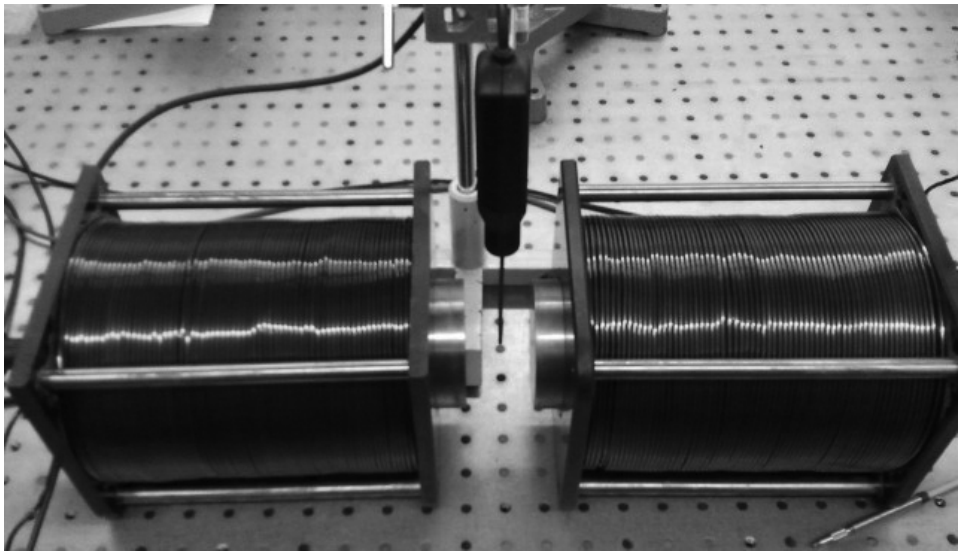

Figure 6.3: Image illustrating the setup used for characterizing the field variation and strength around the two electromagnets used in the experiment described in Sec. 6.2.

6.3.1 Magnetic Field Strength Measured using a Hall Probe

In Figure 6.4 the simplified electromagnet setup from Figure 6.3 is depicted from above with a spacing of 40*mm*.

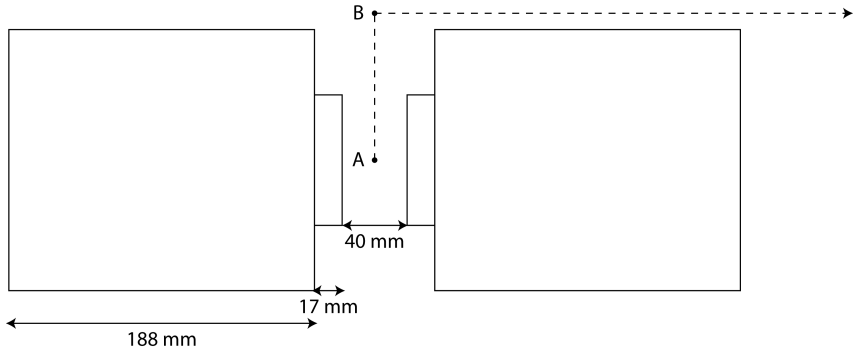

Figure 6.4: Schematic of the electromagnets described in Sec. 6.2 from above. They are spaced 40*mm* apart with the coils placed as far from each other as possible. The point denoted *A* is the starting point for measuring the magnetic field strength, all measurements are carried out along the dashed arrows.

The magnetic field strength is initially measured at point *A* and the along the dashed line with varying distance between measurements, see Table 6.1. All measurements were carried out with a constant current of 10*A* through the coils. *d* denotes the distance in *mm* from point *A* in a vertical direction, after reaching point *B* the distance increases in a horizontal direction as illustrated in Figure 6.4.

A:		B:	
d [mm]	B [mT]	d [mm]	B [mT]
0	91.9	0	10.5
10	91.2	20	7.1
20	88.8	40	2.6
30	81.9	80	-5.3
40	67.5	180	-7.3
50	48.1	240	0.9
60	32.9	270	4.0
70	21.9	290	4.5
80	15.0		
90	10.5		

Table 6.1: Table containing the measured field strengths from the electromagnets illustrated in Figure 6.3.

Plots of the two data series are seen in Figures 6.5(a) and 6.5(b).

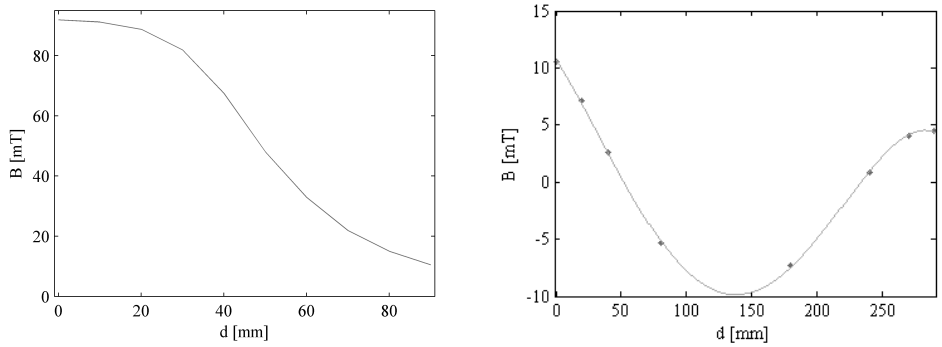

(a) B-field strength along $A \rightarrow B$ route.

(b) B-field strength along $B \rightarrow$ route.

Figure 6.5: Plot of the magnetic field strengts given in Table 6.1, Figure 6.5(a) illustrates the $A \rightarrow B$ route while Figure 6.5(b) shows the $B \rightarrow$ route.

The first data series in Figure 6.5(a) is plotted to illustrate the field variation in the space between the poles. As one might expect the field is strongest in the middle and weakens towards the edges of the magnet cores. Furthermore, it is evident from the figure that the loss of field strength is larger near the edge of the cores, which is at 40*mm* in Figure 6.5(a). This indicates that a large core diameter compared to the spacing between the cores gives rise to a more continuous field.

In Figure 6.5(b) the second data series is presented which illustrates the field variation along the side of one of the coils. From the beginning the field stays at a fairly low level compared to the maximum value attained as expected from the results seen in Figure 6.5(a). Furthermore, the field strength drops to a negative value, which indicates that the field lines have changed direction. Accordingly the other electromagnet no longer influence the field generated by the electromagnet measured along.

6.3.2 COMSOL Multiphysics Simulation of the Magnetic Field

In order evaluate the homogeneity of the magnetic field generated by the electromagnets, the same setup as used in Sec. 6.3.1 is simulated in COMSOL, see Appendix D for a description of the program. In Figures 6.6(a) and 6.6(b) the basic geometry is depicted:

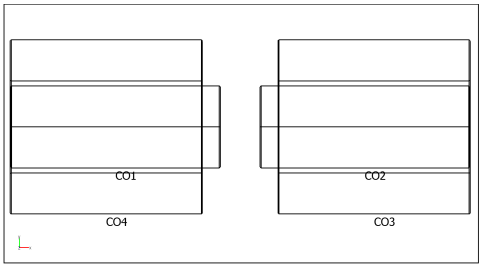

(a) 2D illustration of the two electromagnets from Figure 6.3. All dimensions in the simulation were natural size.

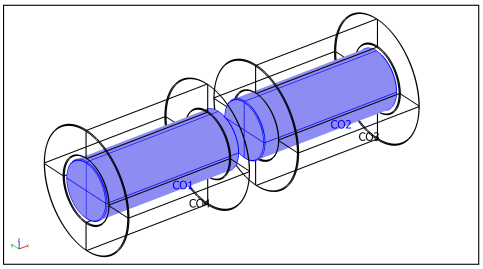

(b) 3D illustration of the two electromagnets from Figure 6.3. The iron cores are highlighted.

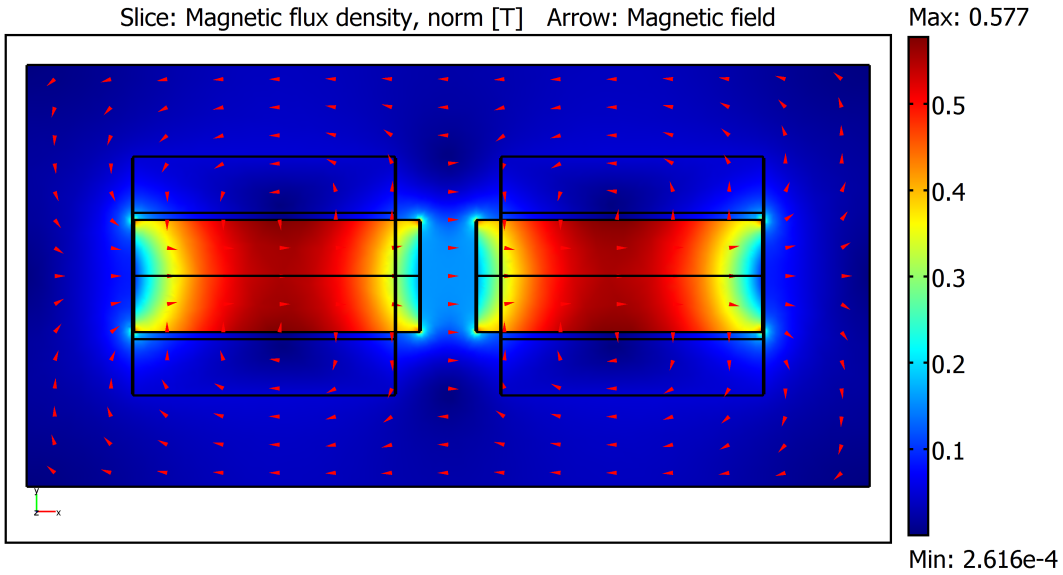

(c) Plot of the normalized magnetic flux density in the xy-plane at $z = 0$, the arrows indicate the magnetic field direction with z-components left out for simplicity. The simulation was carried out with 94000 tetrahedrons.

Figure 6.6: COMSOL simulation of the magnetic field generated by the two electromagnets seen in Figure 6.3. Figures 6.6(a) and 6.6(b) illustrates the basic geometry solved and Figure 6.6(c) the result.

The geometry used in the simulation representing the two electromagnets from Figure 6.3 is illustrated in Figures 6.6(a) and 6.6(b). Lengths and widths are the same as the ones introduced in Sec. 6.2. However, the coils are near impossible to model exactly due to the high number of copper windings. Instead the coil is modelled as a solid copper block surrounding the iron core. Naturally this gives rise to a higher copper density in the coils and will accordingly yield a higher magnetic field strength. This is a known inaccuracy, however, the magnetic field variation should show the same tendencies but at a higher magnitude. The electric current density is fixed at the same value as would be the case in the actual copper wire with $10A$ applied.

In Figures 6.7(a) and 6.7(b) the same field strength curves as measured in Fig-

ures 6.5(a) and 6.5(b) are depicted for the simulation:

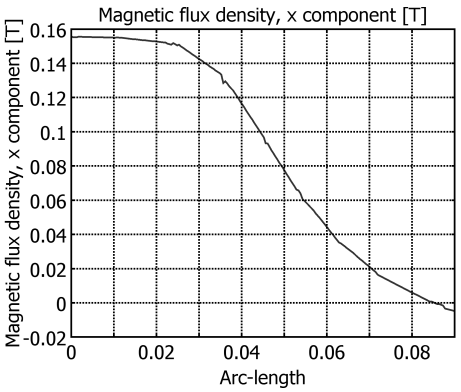

(a) X-component of the simulated field strength from the center between the magnet cores and 90mm outwards.

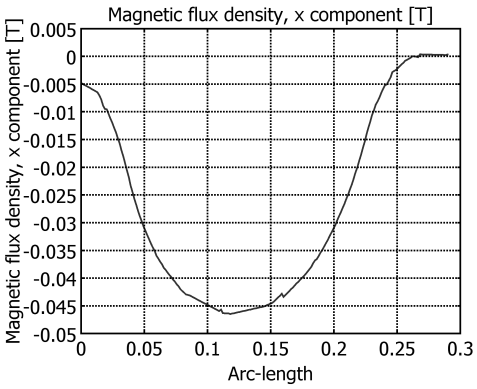

(b) X-component of the simulated field strength along the side of one of the coils.

Figure 6.7: Field strength simulated in certain points for comparison with measured values plotted in Figures 6.5(a) and 6.5(b).

It is clear that the two curves exhibit the same tendencies as observed in the experimentally measured ones. However, from Figure 6.7(a) it is clear that the field strength is about $50-60mT$ stronger and that the field changes direction closer to the electromagnets than in reality. These divergences from the experimental results are not unexpected as earlier stated. The simulation is in principle an ideal system without e.g. impurities or internal boundaries in the iron cores. Furthermore the electromagnets are simulated as sustained in free air, whereas in the experiment the electromagnets are placed on a metallic surface.

In spite of the divergence the simulated curves are in good agreement with the experiments and are therefore regarded as highly useful when trying to depict the magnetic field uniformity and to some degree the field strength. Based on this it seems reasonable to estimate the optimal magnet design regarding field homogeinity and field strength using COMSOL. Not surprisingly it is clear from Figure 6.7(a) that the sample under consideration should be placed in the center between the electromagnet cores spaced with the smalles possible distance. Finally it is also clear from Figure 6.7(a) that the electromagnet core diameter is directly linked to the homogeinity of the field in the gap.

6.4 *Fe* Thin Film Fabrication

In the following section the fabrication of the sample used for SMOKE measurements in free air is described. The sample is desired to consist of a nonmagnetic substrate with a ferromagnetic material deposited on top. This is naturally to isolate the magneto-optic response from the deposited material as much as possible. Furthermore, it is desired to obtain a film like ferromagnetic structure in order to

minimize the contact with free air. This is done by depositing a rather large quantity of ferromagnetic material.

The nonmagnetic substrate in this experiment is an ordinary $Si(100)$ wafer, this substrate is used merely because it is available in abundance. As a ferromagnetic material *Fe* is evaporated on top of the *Si* substrate following a standard physical vapor deposition (PVD). Scanning electron images (SEM) of 30*nm* of *Fe* deposited on $Si(100)$ are seen in Figures 6.8 and 6.9:

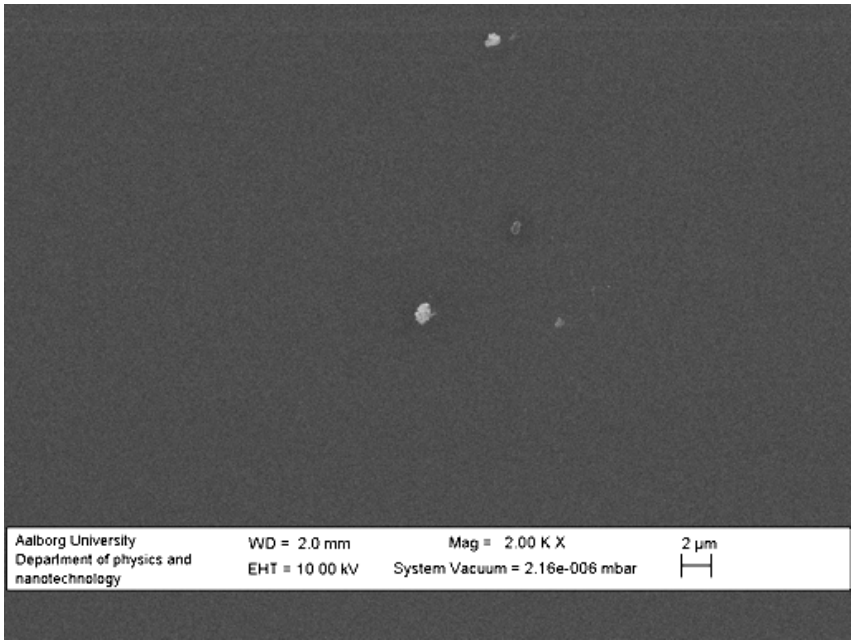

Figure 6.8: SEM image of 30*nm* of *Fe* deposited on $Si(100)$. Apart from a few structures placed arbitrary on the surface, the *Fe* seems to have favored a film like growth.

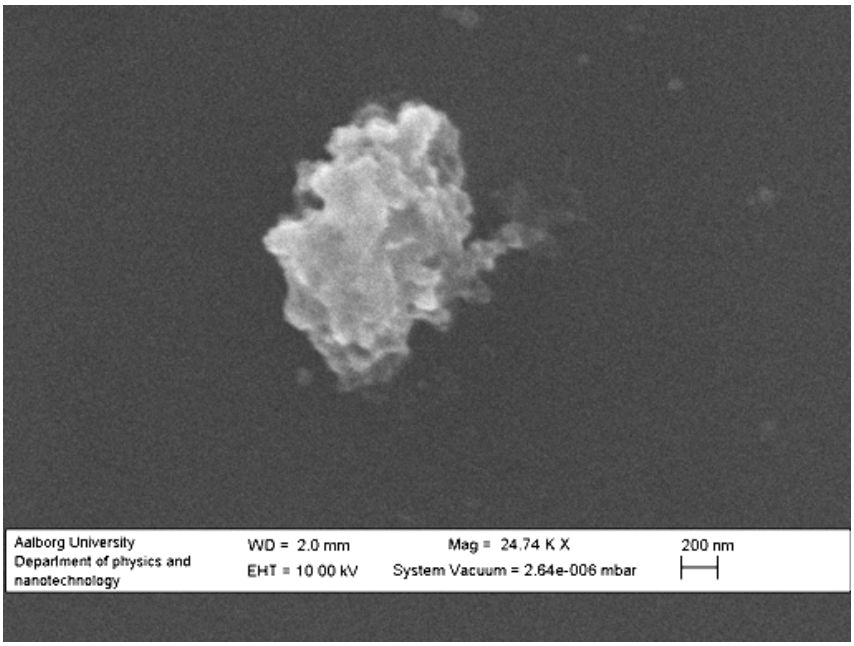

Figure 6.9: A magnification of one of the structures seen in Figure 6.8.

Apart from the few larger structures seen in Figure 6.9 the deposited *Fe* seems to have favored a film type growth. The film thickness was measured to app. 30*nm* afterwards using a profiler in order to validate the quantity of *Fe* deposited on the $Si(100)$ substrate.

6.5 Magnetic Properties of *Fe* Thin Films

The overall goal of this experiment is to validate SMOKE as a method for characterizing magnetic properties of surface structures. Based on this SMOKE is used to record the hysterisis loop of the *Fe* thin film described in the previous section. Furthermore, in order to validify that the *Fe* thin film is in fact responsible for the obtained results they are compared to results gained by using SMOKE on a clean *Si* wafer and on a oxidized *Fe* thin film. Finally, it is of interest to investigate the effects of a nonmagnetic capping layer, and accordingly 20*nm* of *Sn* is deposited on top of the *Fe*.

The measurements are carried out in the way described in Sec. 5.5. To limit noise and fluctuations in the curves all presented measurements are an average of several SMOKE loops each of which are an average of 10 intensities pr. data point. In all measurements the angle δ away from full extinction is chosen to 2°.

6.5.1 SMOKE Measurements on 30nm *Fe*

As mentioned above the sample under consideration consists of a $Si(100)$ substrate with 30*nm* of *Fe* deposited on top. As all measurements are carried out outside

of vacuum the *Fe* surface must be assumed contaminated. This atleast includes to some degree oxidation of the surface of the *Fe* film.

In [9] *Fe* evaporated onto a glass substrate and bulk *Fe* is exposed to the atmosphere and monitored using AFM on selected times over 11 months. On the *Fe* thin film the oxides tends to form on geometrical favorable positions, whereas the smooth surface of the bulk *Fe* displayed a smaller amount of oxide products. Overall the smooth surface displayed a lower oxidation rate than the more rough microstructure.

Based on this it seems fair to conclude that the *Fe* thin films are terminated by a thin layer of oxide. The thickness of this nonmagnetic spacer layer atop of the *Fe* should be well within the model presented in Sec. 5.2 if one ignores any other impurities present. Therefore it seems fair to conclude that the oxide layer has no og negligeble influence on the magneto-optic signal from the *Fe*. In Figures 6.10 and 6.11 the SMOKE measurements for incident p- and s-polarized light, respectively, are presented for a longitudinal Kerr setup:

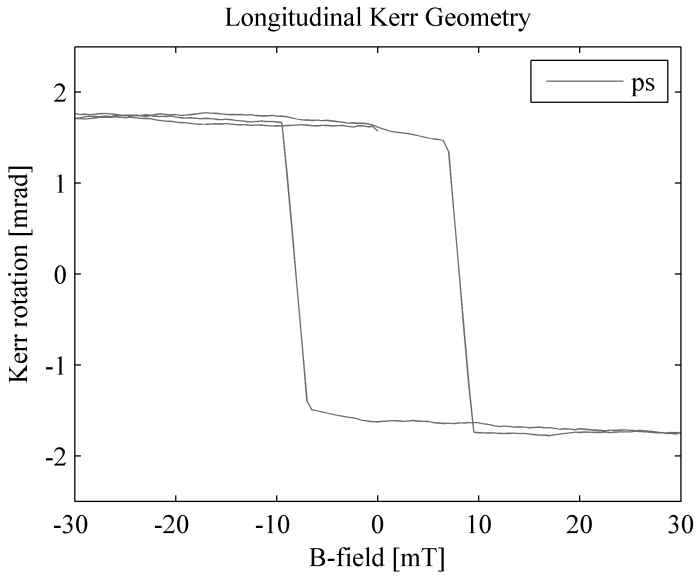

Figure 6.10: Hysterisis loop of a 30*nm Fe* thin film measured using a longitudinal Kerr setup for incident p-polarized light.

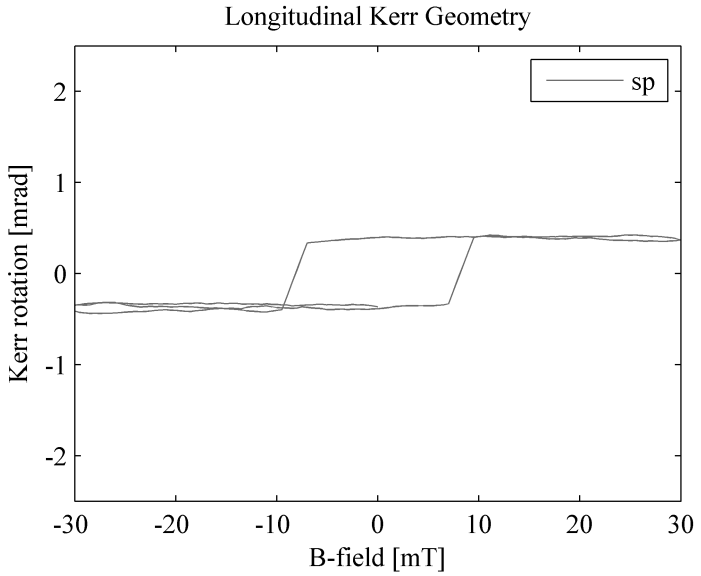

Figure 6.11: Hysterisis loop of a 30*nm Fe* thin film measured using a longitudinal Kerr setup for incident s-polarized light.

The curves presented in Figures 6.10 and 6.11 are clearly hysterisis loops. Measurements were limited to the range of $H = [-30mT; 30mT]$ as no further response was observed outside of this area. The same measurements are carried out on clean $Si(100)$ and are presented in App. E. From the results on clean $Si(100)$ it is concluded that the hysterisis loops are due to the 30*nm* of *Fe*. The coercive field[1] is identified as app. $8mT$ in both hysterisis loops. This is to be expected as the magnetization of the sample should not change with the rotation of the polarization.

As mentioned in Sec. 5.5 the measurements are started out by ramping the field from zero to the highest possible in either the positive or negative direction. Accordingly the magneto-optic response should initially be zero and rise at a given field strength. Yet, as is clear from the figures the degree of Kerr rotation is already at its saturation value when the measurement is initiated. This was consistently observed when measuring on the 30*nm Fe* samples. The reason for this is basically that the thin film maintains its magnetization after a hysterisis loop is recorded. Even after several hours the film maintained the magnetization.

As discussed in Cha. 4 magnetic thin films display easy and hard magnetization axes. Generally one reduces these considerations to regarding an in- or out of plane easy magnetization axis. Whether the easy magnetization is in- or out of plane can be identified from the shape of the hysterisis loop, see Sec. 4.2.

The rectangular looking hysterisis loops from Figures 6.10 and 6.11 clearly indicate an inplane easy magnetization axis. This is in accordance with [4] where it is shown that *Fe* thin films of more than 10*ML Fe* displays in-plane easy magnetization axis. The squareness of the two depicted loops furthermore indicates a

[1] The coercive field of a ferromagnetic material is the field necessary for reducing the magnetization of the material to zero after saturation has been reached. In principle the coercivity of a ferromagnetic material describes how hard it is to demagnetize after saturation.

switching of large single domains.

From the figures it is clear that the hysterisis loop seems to change sign when the polarization of the incident light is rotated. Physically this means that incident s- and p-polarized light is rotated oppositely to each other in this particular sample. From Eqs. 5.8a and 5.8b this is not surprising as r_{ps} and r_{sp} have a different sign in front of the Voigt component in the longitudinal direction. Accordingly, if $Q_{longitudinal} > 0$ and $Q_{transverse} \approx 0$ or $Q_{longitudinal} >> Q_{transverse}$ the Kerr rotation would change sign together with the polarization.

Before it is justified that the above results are in fact generated by the *Fe* layer, the same measurements are carried out on a similar sample where the *Fe* is oxidized.

Oxidized *Fe*

In order to justify that the ferromagnetic *Fe* layer really generates the magneto-optic response shown in Figures 6.10 and 6.11 identical measurements are carried out on an oxidized 30*nm Fe* thin film. The sample is oxidized by heating the sample to 500°*C* for app. two hours in atmospheric conditions. The results of the longitudinal SMOKE measurements are displayed in Figure 6.12:

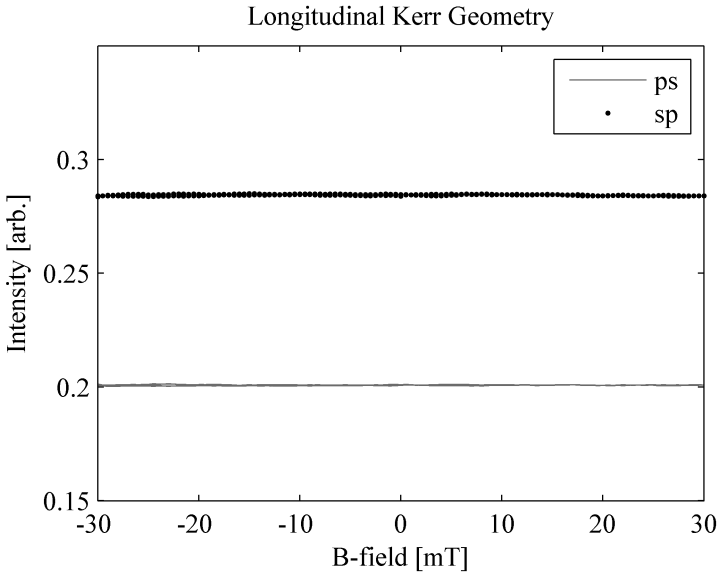

Figure 6.12: SMOKE measurements applied to 30*nm* of oxidized *Fe*.

It is clear from the figure that the oxidized *Fe* thin film does not exhibit any ferromagnetic properties. This confirms that the hysterisis loops in Figures 6.10 and 6.11 are in fact due to the 30*nm* of *Fe*. Based on this it is concluded that SMOKE is in fact a viable method for characterizing magnetic structures. Furthermore through SMOKE it is possible to identify magnetic properties like the coercive field, magnetic field saturation, and easy/hard axis directions. In the following section the effect of a nonmagnetic capping layer is investigated.

6.5.2 Nonmagnetic Capping Layer

As mentioned in the introduction of this section, 20*nm Sn* was deposited on top of the 30*nm* of *Fe* in order to investigate the effects of a nonmagnetic capping layer. The *Sn* was deposited in the same vacuum chamber as the *Fe*, however, before deposition of *Sn* the sample was exposed to air. This was done in order to attain the same degree of oxidation of the *Fe* layer as in the samples without *Sn* on top. Based on this the sample consists of a $Si(100)$ substrate with a layered structure of 30*nm Fe* and 20*nm Sn* with a small oxide layer in between.

Based on the deriviations in Sec. 5.2 capping the *Fe* with a nonmagnetic layer should not have any impact on the magneto-optic response of the sample. However, this was in the ultrathin limit, and a total film thickness of 50*nm* may be too much for that approximation. Moreover the approximation in Sec. 5.2 does not take into consideration any surface roughness or impurities. So it is more likely that the magnetization of the film behaves as discussed in Sec. 4.2 where a nonmagnetic capping layer is expected to increase the saturation magnetization.

In Figures 6.13 and 6.14 the Kerr rotations in $[mrad]$ are depicted against the longitudinal orientated magnetic field for incident p- and s-polarized light respectively:

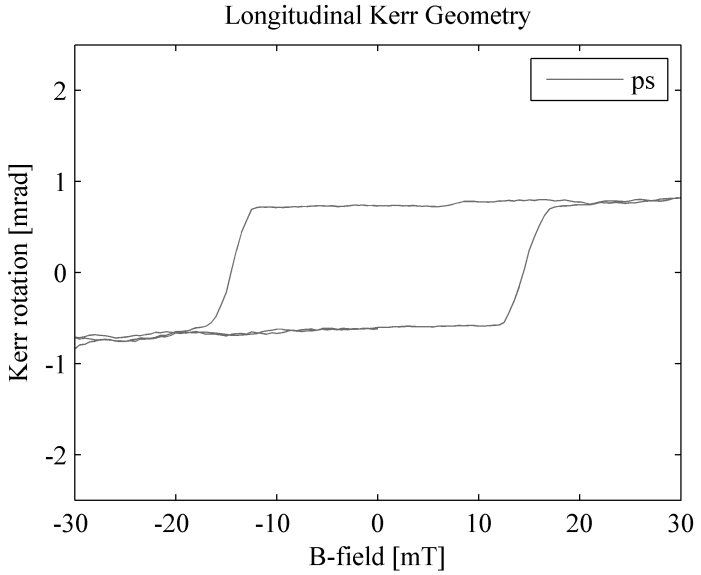

Figure 6.13: Hysterisis loop of a sample consisting of 30*nm* of *Fe* capped with a 20*nm Sn* layer. This measurement was carried out with an incident p-polarized light using a longitudinal Kerr geometry.

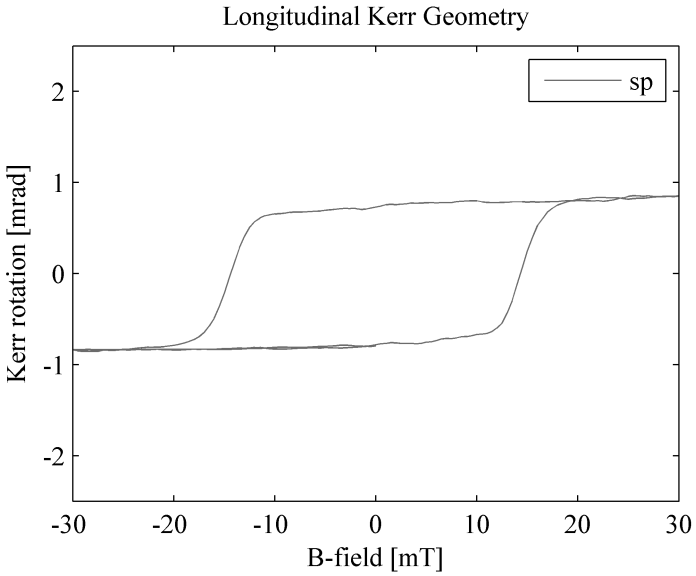

Figure 6.14: Hysterisis loop of a sample consisting of 30*nm* of *Fe* capped with a 20*nm Sn* layer for incident s-polarized light.

The curves in Figures 6.13 and 6.14 clearly span hysterisis loops. As shown in App. E *Sn* in itself does not display ferromagnetic properties, hence the loop must be due to the *Fe*. However, by comparing the loops for this sample consisting of *Fe* and *Sn* with the ones for *Fe* seen in Figures 6.10 and 6.11 some differences are clear. Apart from scalar and shape differences the coercivity is higher.

The coercivity is identified as $14.5mT$ in both hysterisis loops, which compared to the $8mT$ for the clean *Fe* sample means that applying 20*nm* of *Sn* nearly doubles the coercive field. The increase in coercivity is in accordance with theory previously presented as well as results gained by other sources e.g. [6]. In [6] *Ag* is deposited in a wedge like manner on top of $5ML$ of *Co* and the coercivity is measured across the sample. The result is similar to the one presented here, a clear increase in coercive field is observed until a certain critical limit is reached. It is futile to derive further changes to the coercivity and the saturation magnetization from these measurements as too many parameters are uncontrollable, e.g. the degree of contamination.

The scalar changes of the Kerr rotation are irrelevant as the intensity of the incident beam is not necessarily the same. However, the changes in shape are essentiel. When measuring on 30*nm* of *Fe* incident s- and p-polarized light were rotated oppositely each other, this is not the case after *Sn* has been applied on top. This can only be ascribed to changes in the overall magneto-optic response of the layered structure. E.g. if the structure appears isotropic with regard to the Voigt components the Kerr rotation would be similar for incident s- and p-polarized light.

Development of a Vacuum SMOKE Setup

7

As part of this project a SMOKE UHV system was developed in order to investigate the ferromagnetic characteristics of thin film structures. The SMOKE setup needs to be compatible with an existing UHV system, in which the samples are prepared and then characterized by STM. In this chapter the process of development is described from the preliminary ideas to the final design.

7.1 Demands and Preliminary Considerations

In Cha. 5 the concepts of SMOKE are outlined along with the basic components of a SMOKE setup. Furthermore a simple SMOKE setup was constructed around a sample in free air, this is presented in Cha. 6. This setup serves as a verification of the method, however, to acchieve viable results on nanostructured surfaces the experiments need to be conducted in vacuum. This also enables the possibility of surface characterization using STM. As a setup for surface characterization is already at disposal the SMOKE setup is designed to be compatible with this.

Aside from this a cryostat is needed in the setup in order to investigate the temperature dependence of the magnetic properties, e.g. the Curie point.

Additionally some preliminary considerations are discussed regarding the electromagnet as this is a key element in defining the geometry of the setup.

7.1.1 The Existing Setup

The existing UHV system allows for sample preparation using ion sputtering and evaporation along with characterization of the surface via STM. It is an Omicron solution which consists of two main chambers; one for sample preparation, and one for analysis. This is illustrated schematically in Figure 7.1

The operating pressure in the analysis chamber is in the range of $10^{-11} mbar$ and it offers the possibility of performing LEED, Auger, and STM measurements. The vacuum system is positioned on an active table that uses airpressure pistons to stablize it in order to prevent noise during STM measurements.

The preparation chamber usually operates at a slightly higher pressure as it is used for the vacuum degrading processes, i.e. ion-sputtering and e-beam evaporation. Annealing is possible using a W filament on the sampleholder, and cooling is available through a flow of N_2. Finally the preparation chamber is equipped with a load lock system so a sample or STM-tip can be let in without venting the entire setup.

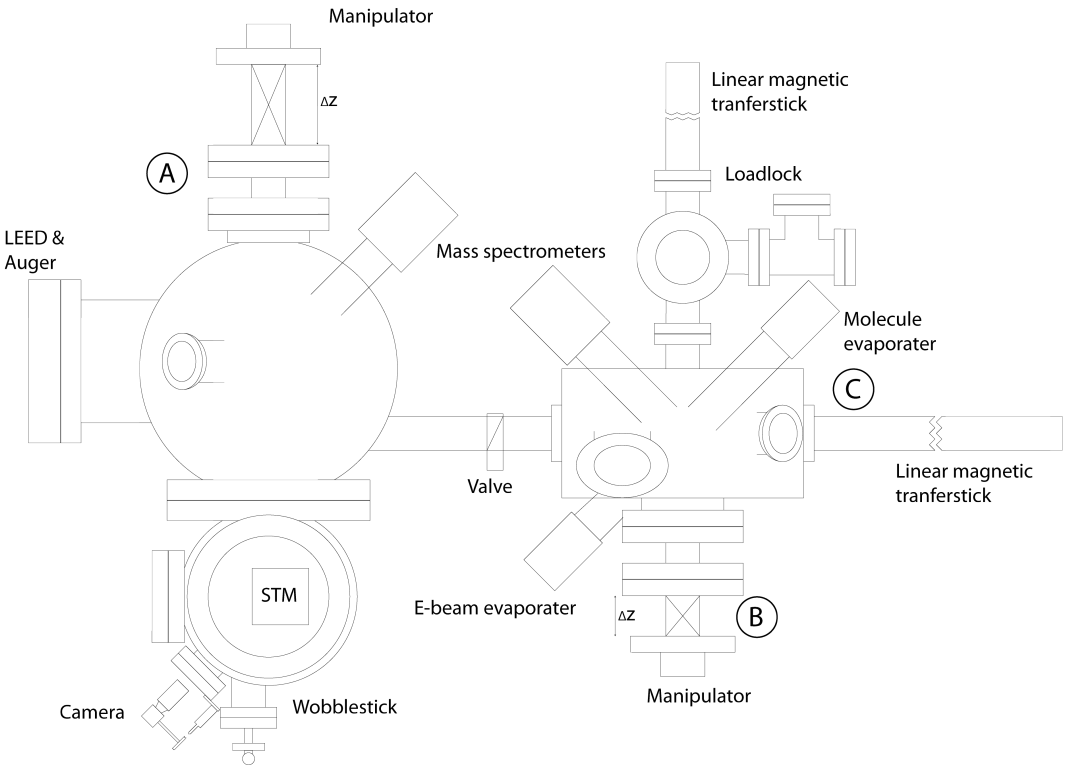

Figure 7.1: Schematic illustration of the existing setup. The labels A, B, and C mark the positions considered for the SMOKE setup.

7.1.2 Electromagnet Design Considerations

Various apects restaint the electromagnet geometry, accordingly the SMOKE chamber needs to accomodate these. The aspects which need consideration are: dipole or quadrupole configuration, core material, pole size and spacing, coils, and if the poles should be inside or outside the vacuum chamber.

As both in-plane and perpendicular magnetization are desired either a dipole or a quadrupole geometry can be used. A dipole geometry is smaller, and hence it is more easily incorporated with the existing setup. It does, however, require either a rotatable sample stage in a three window configuration, see Figure 7.2, or a movement of the poles to obtain both magnetization directions. The advantage of a quadrupole is that a change of magnetization is performed without tampering with the setup.

As discussed in Sec. 5.4.1 a field strength of $200mT$ is desired. A powersupply capable of delivering $40A$ is readily available, as are the coils used in Cha. 6. To attain this relatively high field measurements and simulations show that the pole spacing must be kept as low as possible. At the same time the pole diameter must be large for the field to be uniform across the measurement area.

Though a quadrupole setup thus is favourable with regard to performance, the compatibility requirement makes a dipole more easily integrated. This is taken into consideration in the design process described in the following.

With regard to the core material it should besides from having a high magnetic

permeability also have a low remanence. This requires a low level of C, which is the case for high purity iron, refer to [3]. Special alloys are also available specifically intended for electromagnets. These are, however, very expensive compared to stainless steel, which may therefore be desired.

7.2 Process of Develepment

In the process of developing the SMOKE setup, the design and ideas have changed extensively. Overall it consists of three parts, which may be distinguished by the position in relation to the existing setup, see Figure 7.1. In order to assess the ideas and ensure their realizability the designs considered during this project are drawn in 3D in the CAD based program SolidWorks. This also allows for creation of detailed work sketches for parts that require special ordering.

In this section the motivation for each of the three positions is presented along with the associated designs. Additional SolidWorks sketches are seen in App. C.

7.2.1 SMOKE setup in the Analysis Chamber

The logical placement of the setup is in connection with the analysis chamber. This is based on the better environment, lower pressure, and less tranfering. The solution considered in the analysis chamber is to design a setup in collaboration with the manipulator marked as position A in Figure 7.1. The idea is to have the SMOKE chamber in between of a manipulator and the analysis chamber so the sample is withdrawn from the latter into the SMOKE setup. The solution thus requires minimal modifications and space to incorporate.

The first design of the SMOKE setup is based on a standard CF100 distance-flange with six minor flanges on the side. As the sample stage is rotatable the setup is designed with a dipole magnet in a three window configuration. A schematic illustration of the idea is seen in Figure 7.2.

As the setup is based on three windows some of the optical components must be movable to allow for a switch between windows. This gives rise to challenges concerning both allignment and positioning in general. To circumvent these the optics are placed on holders attached to the window flanges, see Figure C.1.

The disadvantage of using this position is, however, that the setup requires a very long travelling distance as the sample must also be reachable by the wobblestick at the STM. A long travel is disadvantageous as manipulators of that magnitude are big and expensive. As a result of this the position is revised.

7.2.2 SMOKE Setup at Preparation Chamber Manipulator

In this geometry the chamber is placed at the manipulator in the preparation chamber, marked as position B in Figure 7.1. By using this position a manipulator with a lesser range is required. With an offset in the design considered for the analysis

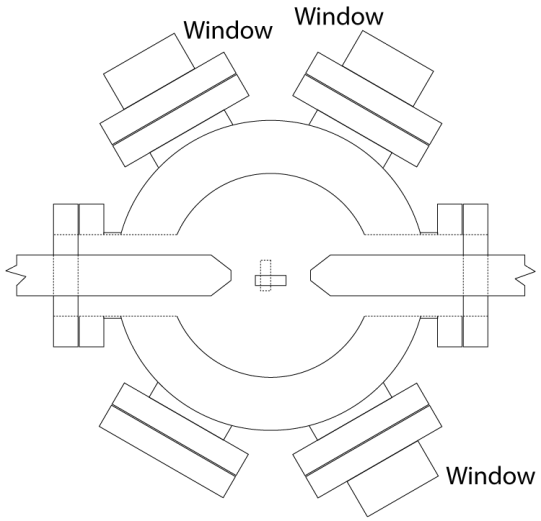

Figure 7.2: A schematic illustration of a three window configuration using a dipole electromagnet. A rotation of the sample switches the magnetisation between in-plane and perpendicular, which requires an extra window.

chamber the attention is turned towards implementing an electromagnet. As mentioned in Sec. 7.1.2 the poles can either be inside or outside of the vacuum chamber. In [30] a SMOKE setup with poles inside the chamber is described. Here the yoke is fed through a flange by welding in a M8 stud used for fastening the pole on each side. Having the poles inside the chamber sets restrictions on the core material. So to ease the construction it is decided to place them outside of the chamber.

In order to bring the poles as close to the sample as possible sockets are introduced into the chamber. Though this allows for a smaller pole gap the minimum distance in this design is limited by the total height of the sample stage as this must be able to rotate freely to swicth the magnetization. To facilitate this it is considered to adapt a solution from [30], where the poles are retractable by use of linear translators. This requires the sockets to be part of a flange, hence the diameter is limited to certain values. In Figure C.2 the chamber part is illustrated with CF40 and CF63 flanges. From these figures it is clear that the CF63 flange is too large. A CF40 flange only allows for an inner diameter of app. 38*mm*, which gives rise to small magnet poles. Furthermore the size of the solution is extensive due to the linear translators. As a result of this it is decided to let the sockets be built into the chamber and have an inner diameter of 52*mm*. This is illustrated in Figure 7.3.

The decision is supported by measurements of the field strength as a function of the pole gap when using the electromagnets described in Sec. 6.3 in a closed circuit.

Having established a geometry for the chamber the attention is turned towards the electromagnet. As the chamber is placed app. 50*cm* above the table the magnet requires support. This is solved by designing a yoke able to stand on its own on the main table. The yoke is based on the design of the electromagnet from which the coils are taken, and is designed to be separable in key positions. This allows it to be handled more easily. A drawing of the magnet is seen in Figure C.3.

The complete SMOKE setup based on this concept is presented in Figure 7.4.

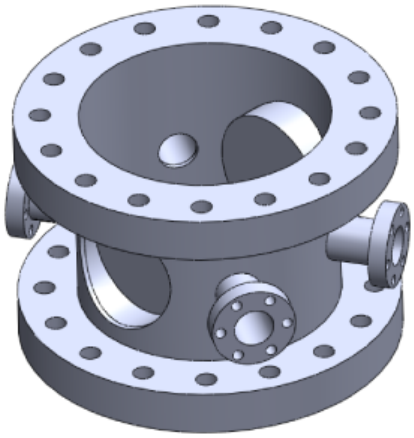

Figure 7.3: The SMOKE chamber with sockets used to bring the electromagnet poles closer to the sample.

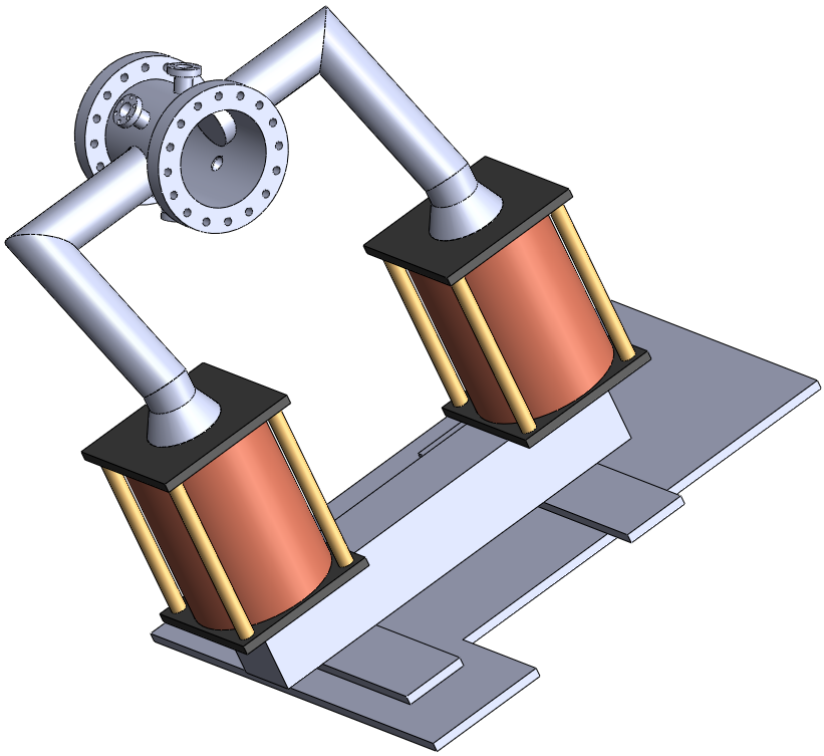

Figure 7.4: SMOKE setup at position B designed with a magnet that stands on the main table.

The main disadvantage is its size and weight, which according to the 3D model is app. $110kg$. Furthermore there are uncertainties regarding the performance of the magnet.

7.2.3 SMOKE Setup in the end of the Preparation Chamber

The uncertainties connected with the fabrication of an electromagnet lead to the decision of investigating the possibility of having the magnet designed by a company specialized in the area. Furthermore it was decided to create a more compact setup, hence a quadrupole magnet is desired.

At the same time the position of the setup is revised, and it is decided that a setup based on the position at the end of the preparation chamber, marked as position C in 7.1, is more flexible. The setup is constructed around a six-way CF63 cube which allows for a manipulator to move the sample into the SMOKE chamber positioned on the opposite side of the cube. The inner diameter of the openings used for the manipulator are increased to avoid the possibility of crashing the cryostat. Additionally four holes are made in the corners on one of the sides for mounting purposes. The cube is illustrated in Figure C.4.

The company chosen for the design of the electromagnet is called Danfysik and in order to illustrate the idea a setup based on a spherical chamber is designed. This design is illustrated in Figure 7.5.

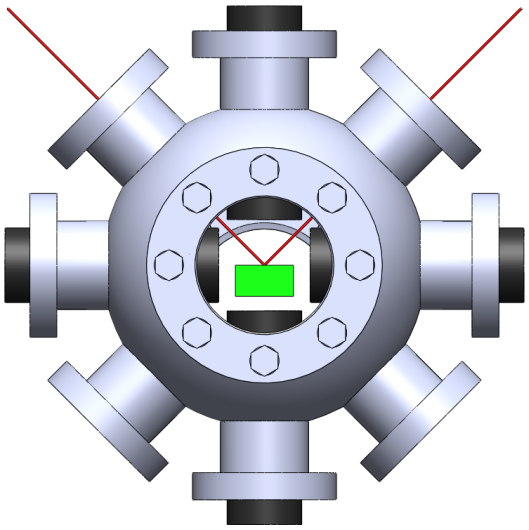

Figure 7.5: The figure is used to illustrate the idea of the setup to the company designing the magnet.

The flange in the back of the chamber is lovered to ensure the sample surface is in the center of the chamber. Of the magnet only the poles are illustrated as the design of the magnet is bestowed upon Danfysik.

Consultations with Danfysik lead to the decision of designing a magnet with a pole gap of $45mm$ in both directions as this is just enough to fit a standard CF40 tube. The adjacent poles are faceted to allow for small tubes to fit between them.

These tubes are used to attach the windows for the laserlight in the void between the coils. The magnet is described in detail in 7.3.

The geometry of the magnet makes it advantegeous to have a vertically oriented setup as this eases both the alignment of the optics and the support of the setup. The latter is important as the setup in total has an estimated weight of app. $70-80kg$. To ease the mounting a flexible coupling is introduces between the setup and the preparation chamber. The coupling part is designed to provide the needed spacing to fit the magnet next to the preparation chamber and acts as a transition from the CF40 flange to the CF63 on the cube. See Figure C.6 for an illustration of the coupling.

Having established a viable arrangement regarding the magnet a SMOKE chamber part is designed which fits both the requirements regarding the magnet and has space for a cryostat, which has a diameter of app. $38mm$. As this might be more than will fit between the poles when a sampleholder is mounted the chamber must be designed so it narrows in right before the poles. This enables the cryostat to move to that point and then allow only the sample holder to reach into the narrow part. To ease navigation of the cryostat and avoid crashing a window is added just above the narrowing. The chamber is seen in Figure C.5. This was, however, cast aside as it was decided to use a spare manipulator that has a shorter range than the one first considered.

As the travelling distance is reduced the chamber in C.5 is too long, and a new one is required. The new manipulator has an inner diameter of only $25mm$ at the entrance, which is smaller than the cryostat that is considered. Additionally cryostats are typically only available for flanges CF63 and larger due to their width. The problem is circumvented by designing a homemade cryostat with a smaller diameter. The homemade cryostat is described in detail in Sec. 7.2.4. As the diameter of the cryostat is reduced it is no longer necessarry to have a wider tube in the top of the chamber. Due to the reduced length there is no longer room for the window used for manoeuvring of the cryostat. But as there are no narrowings it is also obsolete. The simplified chamber is seen in Figure 7.6.

Having established a geometry for the chamber and magnet that defines the frameworks of the setup the smaller parts are considered in the following.

7.2.4 Cryostat

As mentioned in Sec 7.2.3 the inner diameter of the manipulator is only app. $25mm$ and the topflange is a CF40. Cryostats of this size are not ordinary making it costly and time consuming to aquire one. As a consequence of these circumstances a simple cryostat is instead fabricated.

The cryostat is based on a steel tube with a diameter of $21mm$, which is cooled using liquid N_2. To avoid magnetic influence of the cryostat a Cu rod is used for the last $80mm$ before the sample holder. This is done as Cu is nonmagnetic and has a good thermal conductivity. A large contact surface is important between the tube and the rod to effectively cool the Cu reservoir, and furthermore the solution needs to be vacuum compatible. This is solved by welding a bolt in the end of the steel

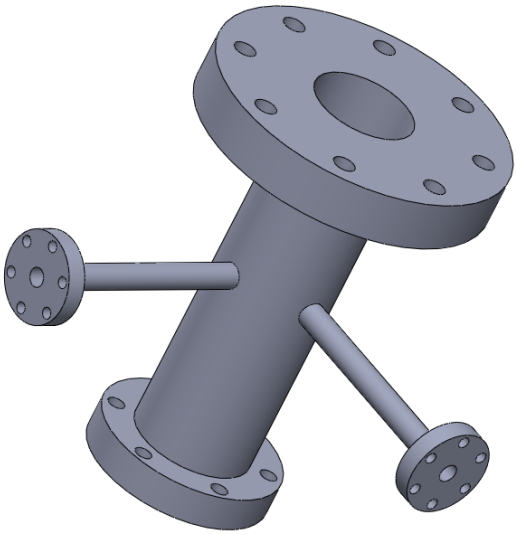

Figure 7.6: The chamber is a modified version of the one in Figure C.5. This chamber requires less range from the manipulator and has no widening in the top as it is designed for a slim cryostat.

tube to give it a threaded rod used to fasten into a tapped hole drilled in the *Cu* rod. To avoid air being trapped behind the threaded rod, a hole is drilled into the side of the *Cu* rod. A washer of *In* is applied between the steel tube and the *Cu* rod for enhanced thermal contact.

The thickness of the tube wall is reduced over part of the length. This is done to reduce the heat transfer between the cryostat and the rest of the chamber giving a more effective control of the temperature. A platform is cut in the sample end of the *Cu* to have a base for attaching the sample holder.

The cryostat is illustrated in Figure 7.7.

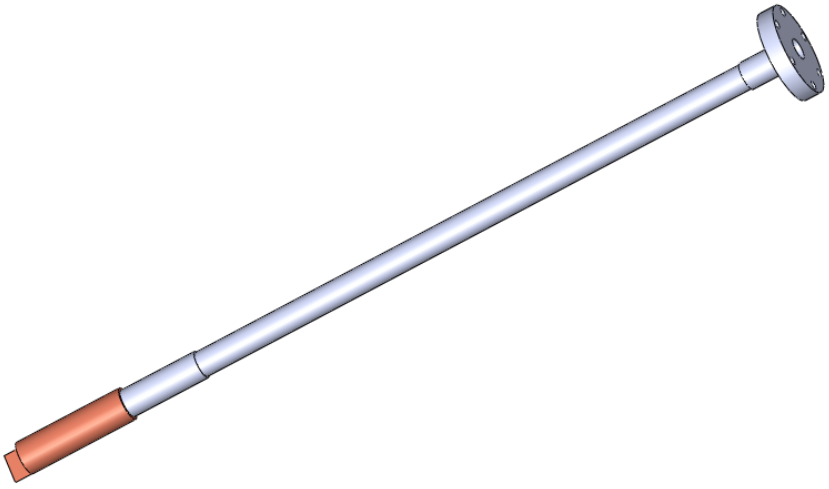

Figure 7.7: The cryostat comprises a steel tube closed with a threaded rod used to attach a nonmagnetic *Cu* reservoir.

7.2.5 Sample Holder

The sample holder is based on a ZHSTSKM model from VG Scienta, with some alterations to make it completely nonmagnetic and compatible with an Omicron $18mm \times 18mm$ flag. The modified sample holder is constructed as follows: The base plate has two tappered holes for the central screws holding the sample holder together. The original plate is made from steel, and is hence replaced by one made from *Mb*. The *Mb* plate is elongated to provide batter stability by fastening it on the cryostat.

Four thin *Mb* plates are placed on top of the base plate to reduce heat radiation. Additionally they have a bend along the edge to contain a *W* filament. The filament is isolated with ceramic spacers and attached to screws in the end of the top plate.

The top plate is replaced as a longer plate is needed. The plate is bolted to the cryostat and base plate in one end, and additionally two screws fastens it to the tappered holes in the middle of the base plate. The top plate consists of two identical plates of $0.5mm$ *Mb*, where the second plate serves as a spacer to countersink two screws. These are used to attach a sample case, which fits an omicron sample flag. The sample holder is seen in Figure 7.8. The resistive heating from the *W*

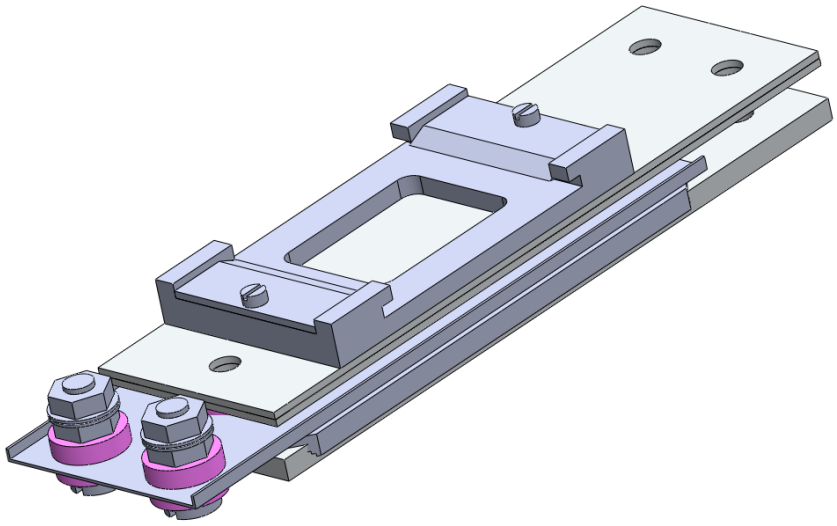

Figure 7.8: The modified sample holder used in the SMOKE setup. It is made from *Mb* plates and held together by *Mb* and *Ti* screws to make it completely nonmagnetic. An omicron sample flag fits into the slit in the sample case in the top part of the holder and is clamped by the two small plates. The filament is attached to the electrically isolated screws in the end, and the thermocouple is fastened using a screw and a washer on the side of the sample case.

filament provides a countermeasure for the cryostat, which is cooled using liquid N_2. This allows for the temperature to be controlled by the applied current. A type E themocouple, chromel-constantan, is used along with an Euroterm 3508 to measure the temperature. The type E thermocouple is nonmagnetic and has a range of $[-200; 900°C]$.

7.2.6 Support

Due to the weight of the setup it is necessary to secure and support it. Furthermore as the setup is placed between the preparation chamber and the linear transfer stick the travelling distance is prolonged, and hence the transfer stick is too short. Accordingly a longer one is needed which also requires additional support. Finally the optics need to be positioned on a plate which can be removed when the system is baked.

As both the vacuum parts and the magnet need to be mounted properly a special frame is constructed, see Figure 7.9. The frame is made from stainless steel as is has

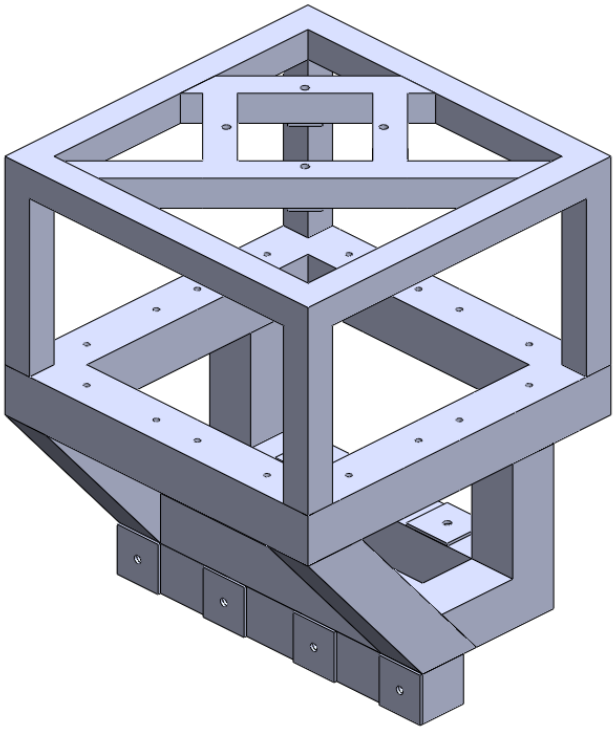

Figure 7.9: The frame used to support the magnet and vacuum parts is designed to fit the edge of the main table. The magnet stands on an aluminum plate on the plateau in the middle and the transverse profiles in the top supports the CF63 cube.

to be bakeable. It is comprised of two parts: the bottom part on which the magnet rests and the top part used to support the vacuum cube, Figure C.4. The bottom part is made from $50 \times 50 \times 3mm$ square profiles and is mounted on the main table on both sides of the table edge. The shape of the frame is designed to fit next to the preparation chamber, where a tube runs below the bend on the back of the frame.

On top of the bottom part of the frame a $10mm$ *Al* plate is placed for the magnet to stand on. *Al* is ideal as it is nonmagnetic and hence does not influence the measurements. In Figure C.7 an illustration of the plate is seen. The hole in the middle allows for use of the window in the bottom of the SMOKE chamber, Figure 7.6. Furthermore it is divided in two so it can be inserted and removed around the SMOKE chamber.

The top part of the frame is constructed from $30 \times 30 \times 3mm$ steel as this fits

beteen the cube and the magnet yoke. A cross is designed in the top of the frame to support the corners of the cube, which are supplied with tappered holes. This also allows the SMOKE chamber to fit in the middle. Additionally a hole is filed in one of the legs to allow for the passage of the laser.

The support for the linear transfer stick is inspired by the original support, where two steel tubes are hinged on the side of the main table and the end of the transfer stick. They are made with regularly threaded holes in one end and oppositely threaded in the other. This enables an adjustment of the length to give a perfect balance and ease alignment of the transfer stick with the rest of the setup. In the modified setup the hinges on the table are moved further down yielding a greater angle and the tubes are elongated.

A special table is designed for the optical components. In addition to bringing them to the needed height the table is easily removed along with the components prior to a system bakeout. This allows the components to remain in their respective positions on the table easing the alignment. The table frame is made from steel and the plate is *Al*. The table is seen along with the optical components in Figure 7.10.

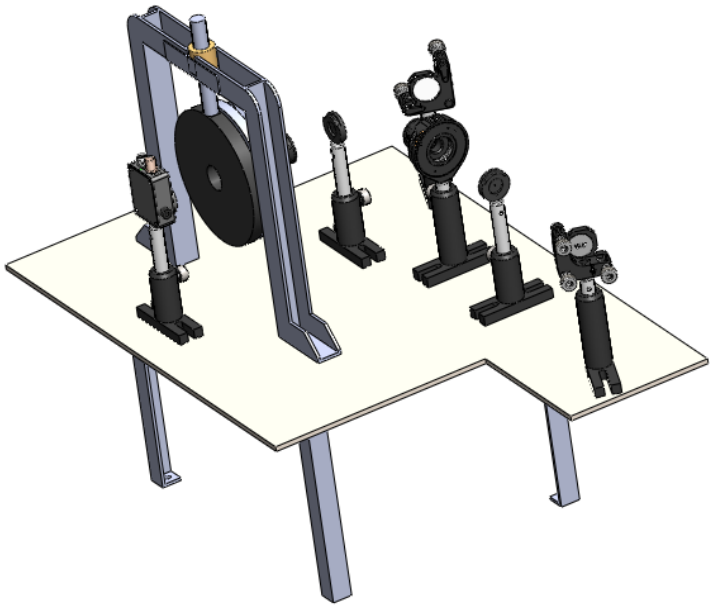

Figure 7.10: The optical components are placed on a table which allows for them to be easily removed all together prior to a bakeout of the system.

7.2.7 Bakeout Isolation

The addition of the SMOKE setup to the existing system makes it too large for the box used for isolation during bakeouts. To circumvent this a new end side plate is made for the box. The plate is made from 1.5*mm Al*, and the joints are sealed using aluminium tape.

7.3 Quadrupole Electromagnet

As mentioned earlier it was decided to have the quadrupole electromagnet designed and fabricated by an external company named Danfysik. Naturally the magnet needed to fulfill all the demands from Sec. 5.4.1 while staying as compact as possible. The blueprint delivered with the electromagnet is presented in App. C.1 and a SolidWorks illustration is seen in Figure 7.11. This illustration was used to evaluate the dimension of the surrounding geometry in SolidWorks. The four poles of the quadrupole electromagnet are denoted 1, 2, 3, and 4, where 1 and 3 are opposite each other and similarly with 2 and 4. The pairs are denoted the 1-3 and the 2-4 geometry respectively, and the current is applied to the coils in the direction implied by the notation. The core diameter is 50*mm* and all cores are chamfered to a width

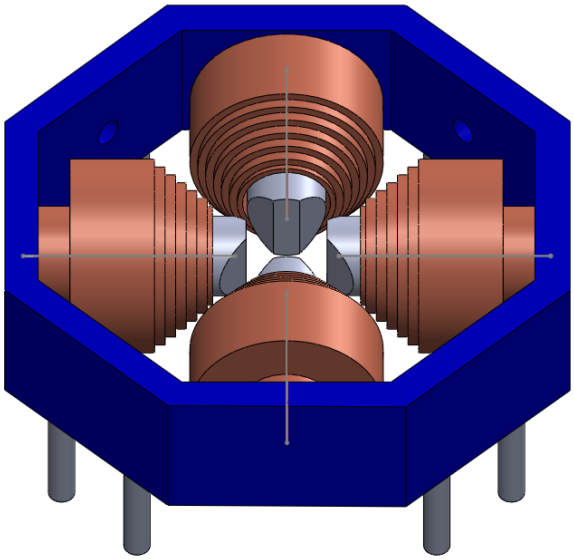

Figure 7.11: SolidWorks illustration of the custom ordered electromagnet from Danfysik. Detailed blueprints for the geometry is presented in App. C.1.

of 20*mm*. All coils are 110*mm* in diameter at the widest point and narrows to a diameter of 50*mm*. The coils consist of 63 turns of copper and the yoke/core consists of S235-JRG2 steel[1]. The yoke is 20*mm* wide, 80*mm* high, and forms an even octagon with sidelengths of 132.55*mm*. Combining the coils and the yoke the total weight of the electromagnet amounts to app. 50*kg*. As described in Sec. 7.2.3 the spacing between pole tips is ordered to be 45*mm* to allow a CF40 tube in between, however, after an inspection of the electromagnet it is evident that this distance is not uniform everywhere in the gap. In fact it is clear that the poles are uneven with regard to length and the surface of the tips are far from leveled. This naturally gives rise to an error when considering the field homogeneity, as well as field ramping when comparing the 1-3 and 2-4 geometry. This inaccuracy in the production needs

[1]The product code S235-JRG2 indicates which type of steel one considers. Basiccally it contains information of the layout, composition and strength of the material. This steel is so-called structural carbon steel, the remaining information contained in the number regarding strength etc. is irrelevant in the present.

to be remedied, but due to lack of time, the inaccuracy must be tolerated for now.

Naturally the electromagnet setup needs to be characterized thouroughly, this is carried out in the followingly by measuring the field using a Hall probe and by COMSOL simulations. The data obtained is then compared to values provided by the manufacturer for validation.

7.3.1 Magnetic Field Characterization

In Figures 7.12 and 7.13 the magnetic field strength generated by the quadrupole electromagnet with 40A applied is illustrated for the 1-3 and 2-4 geometry respectively.

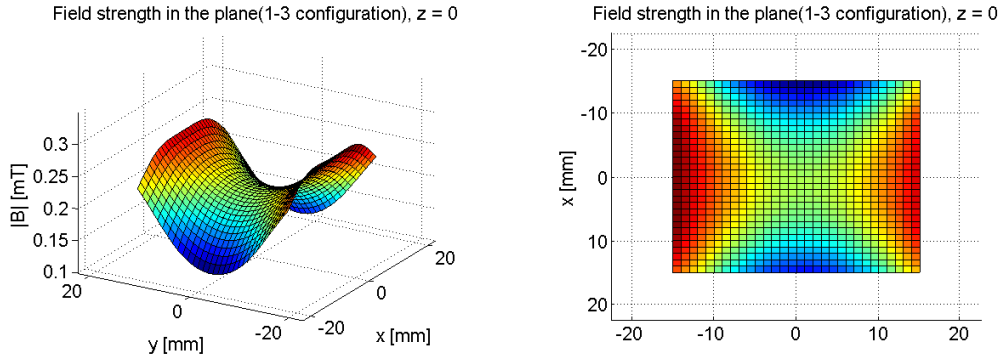

(a) 3D surface plot.

(b) Plot along the z-axis.

Figure 7.12: Surface plot of the field strength in a plane between the poles in $z = 0$. The y-axis is orientated between the two poles i.e. as a normal to the pole surfaces, whereas the x-axis is orientated parallel to the pole surfaces. This plot is the field strength generated by the 1-3 pole geometry.

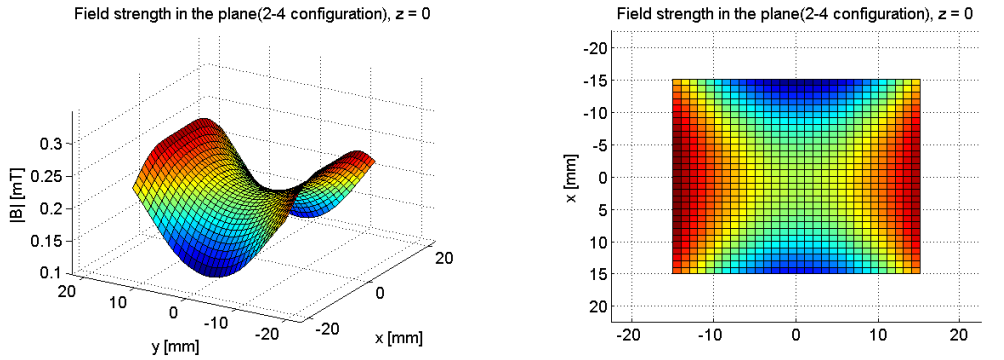

(a) 3D surface plot.

(b) Plot along the z-axis.

Figure 7.13: Same situation as in Figure 7.12 for the 2-4 geometry.

These measurements were conducted by Danfysik and delivered with the electromagnet. The measurements are carried out with 40A applied to the coils and the

field is measured in planes between the poles. Origo is placed in the center between the poles, and measurements were taken in the plane $x = [-15mm, 15mm]$, $y = [-15mm, 15mm]$ in $1mm$ steps. 29 planes were recorded in the area $z = [-14mm; 14mm]$ in $1mm$ steps. Only the two planes recorded in $z = 0$ are presented in Figures 7.12 and 7.13. From the plots along the z-axis in Figures 7.12(b) and 7.13(b) the lack of field homogeneity is evident. Apart from the fact that the field strength is much higher at the pole to the left in the figures[2], the field strength is significantly higher in the bottom than in the top of the figures[3]. Based on the measurements carried out by Danfysik it is concluded that the magnetic field generated by the electromagnet is extremely inhomogeneous, which naturally gives rise to errors in the data obtained through SMOKE. Through consultation with Danfysik it was discovered that the lack of homogeineity in the longitudinal direction of the magnetic field is due to the relationship between gap and core diameters. In order to gain the same field strength at both pole faces the core diameter must be widened. The inhomogeneity in the transversal direction with regard to the field direction the shortcommings of the electromagnet is attributed to the innacurracy in the production. This discrepancy should be remedied at a later time. This is naturally very unsatisfactory as the electromagnet was ordered at Danfysik to obtain a high quality electromagnet with regards to field homogeneity.

In the following the current versus magnetic field characteristics (I-B) of the electromagnet are measured using a Hall probe, the probe is fixated in origo inside a CF40 tube placed in the pole gap. This is done to simulate the conditions of the final setup. The current is ramped in the following steps:

1. $0A$ to $40A$
2. $40A$ to $-40A$ [4]
3. $-40A$ to $40A$ [4]

After reaching $40A$ in step three the current is turned directly to zero. This ramping is exactly the same as the method used when measuring a hysterisis loop. In Figures 7.14(a) and 7.14(b) the I-B curves for the 1-3 and 2-4 geometry are presented, in both cases the positive current direction is along the direction of the numbering of the poles, that is from 1 to 3 and 2 to 4.

[2]Notice the differens in the density of the deep red color at $y = -15$ and $y = 15$, indicating the highest field in the plot, app. $280mT$

[3]This is seen by regarding the density of the dark blue color corresponding to a field strength of app. $130mT$, which clearly is higher in the top.

[4]The current directions is switched using relays, this is described in detail later.

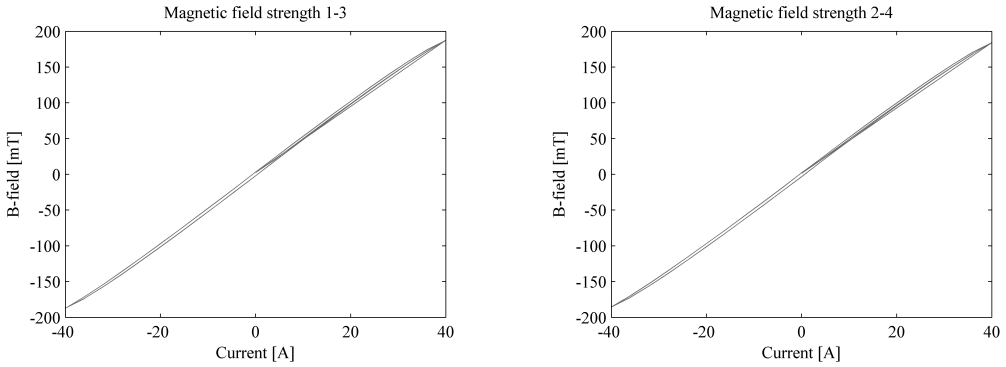

(a) I-B curve for the 1-3 pole geometry.

(b) I-B curve for the 2-4 pole geometry.

Figure 7.14: Current versus magnetic field characteristics of the two geometries, 1-3 and 2-4. The current is ramped through an entire loop.

From the measurements presented in the figures it was apparent that the total remanence of the setup is non-zero. This is clear from the I-B characteristics as the curve does not pass through origo. After applying $40A$ corresponding to a field of app. 180 mT inside the CF40 tube the remanens of that particular geometry was as high as $2-3mT$. By removing the CF40 tube it was discovered that this remanence is solely due to the electromagnet. This is naturally another error in the electromagnet setup, and must be due to the material used for the poles and the yoke. As before mentioned these consists of so-called carbon steel, which is steel where no minimum content of chromium, cobalt, nickel etc. is specified. In Sec. 7.1.2 it was specified that to obtain a low remanence the material should be as close to pure iron as possible, and accordingly carbon steel is not the ideal compound for low remanence electromagnets. This shortcomming of the electromagnet should also be remedied at a later time, e.g. by substituting the poles, which is also agreed upon with Danfysik. For now, however, the remanens must be ignored, and hopefully the error is minimized by proper calibration.

In the following section the electromagnet is characterized thorugh COMSOL simulations.

7.3.2 COMSOL Simulation of Field Characteristics

As in Cha 6 the magnetic field generated by the electromagnet setup is simulated using COMSOL multiphysics. There are several reasons for performing these simulations. Initially they are used in the design process of the quadrupole electromagnet for validation of the geometry, e.g. the simulation is used to estimate how fast the magnetic field attenuates as a function of z[5]. This relation is important in order to estimate the necessary length of the copper adapter between the cryostat and the sample holder, see Sec. 7.2.4 for details. The simulation is carried out using the full

[5]The z-axis is orientated in the same way as in the field characteristics presented in Figures 7.12 and 7.13

scale electromagnet geometry seen in Figure 7.15:

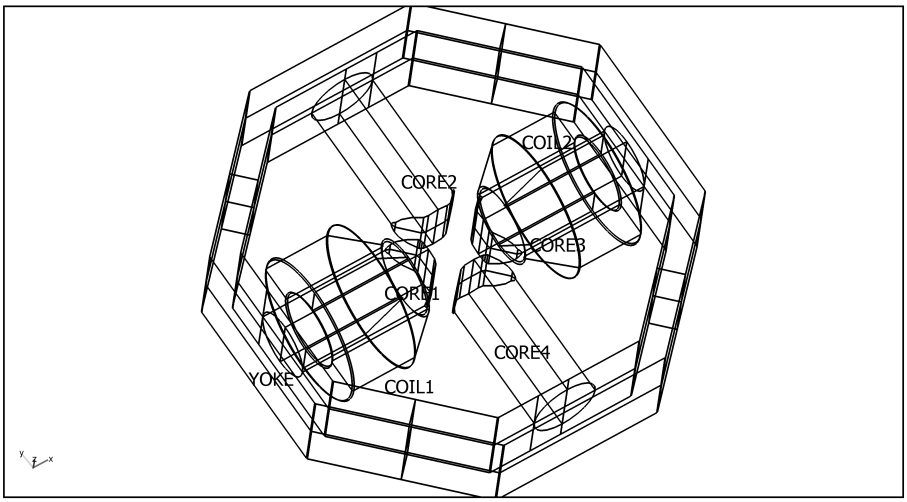

Figure 7.15: Schematic of the geometry used for simulations of the magnetic field generated by the quadrupole electromagnet. In the simulations most dimensions are an exact copy of the real electromagnet geometry.

In the simulations only the two coils where the current is applied is included, this is illustrated in the figure. The other two are excluded in order to limit the amount of boundaries and thus the amount tetrahedrons needed for the simulation. Furthermore, as in Sec. 6.3.2 the coils are modelled as solid *Cu* and the stepwise narrowing of the coils seen in Figure 7.11 is approximated by a straight line. The initial simplification is discussed in detail earlier and gives rise to an overall larger magnetic field strength. The latter, however, is considered to be very reasonable as it limits the amount of corners and boundaries and thus the risk of singularities and the number of tetrahedrons. In the simulation the PDE is only dependent on the free current density, as described in Sec. D.2 in App. D, which in our case is considered constant. Therefore the field induced in the core by the coil is only dependent on the coil volume and the distance between core and coil[6]. Accordingly, substituting the stepwise narrowing with a straight line seems a good approximation.

In the following it is attempted to simulate the field strength surface plots presented in Figures 7.12 and 7.13. The result is seen in Figure 7.16:

[6]This statement is naturally only valid in the present simulation.

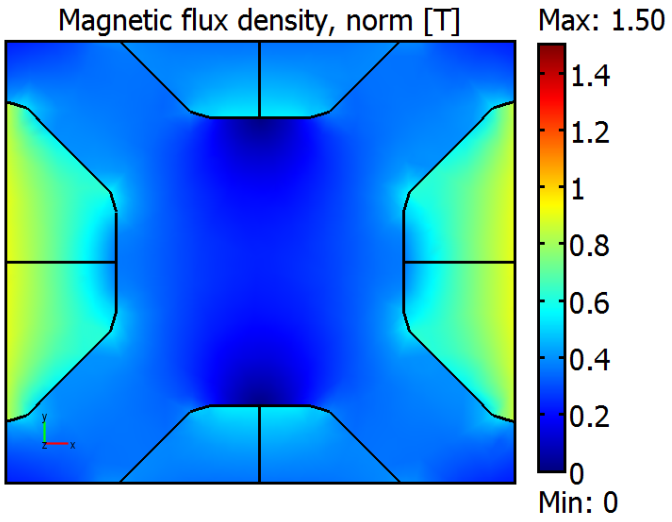

Figure 7.16: COMSOL simulation of the magnetic field generated by the electromagnet from Figure 7.11 with 40*A* applied to the coils 1 and 3. The magnetic field strength displayed is for the plane in $z = 0$.

The geometry is the same as in Figures 7.12 and 7.13, though this figure displays the field inside of the pole tips as well. This surface plot is naturally perfectly symmetrical as the geometry is modelled ideally. Furthermore in Figure 7.16 it is seen that the maximum field value in the gap does not appear in the center of the core, but around the edges closer to the coils. This is naturally a discrepancy in the simulation which is seen by comparison with the experimental data. The reason for this error is attributed to an error in the solver around edges, even though all edges are chamfed with several millimeters, singularities appears in the solution.

The field strength calculated in origo is also significantly higher than experienced in reality. Experimentally it was measured to be $203mT$ in one direction and $199mT$ in the other, whereas theoretically it is calculated to be $232mT$. This is not unexpected as discussed earlier in Cha. 6, the copper density in the coils is higher in the simulation than in reality, and the boundaries between the core and yoke are modelled as an ideel continuum. Furthermore the relative permeability of the core material is estimated as Fe, which is presumed to be higher than for ordinary steel.

By observing the field lines of the simulated magnetic field it is also clear that the two cores not in use shunts the magnetic field. This minimizes the magnetic field strength obtained in origo, accordingly if one desires a field strength above $200mT$ the cores not in use could simply be removed.

Effects of a CF40 Tube

During SMOKE measurements a CF40 low magnetic steel tube surrounds the sample. In spite of being low magnetic the tube may affect the overall magnetic field behaviour. Accordingly the same simulation as illustrated above is carried out with a tube of $44mm$[7] in diameter and $2mm$ walls. This is seen in Figure 7.17.

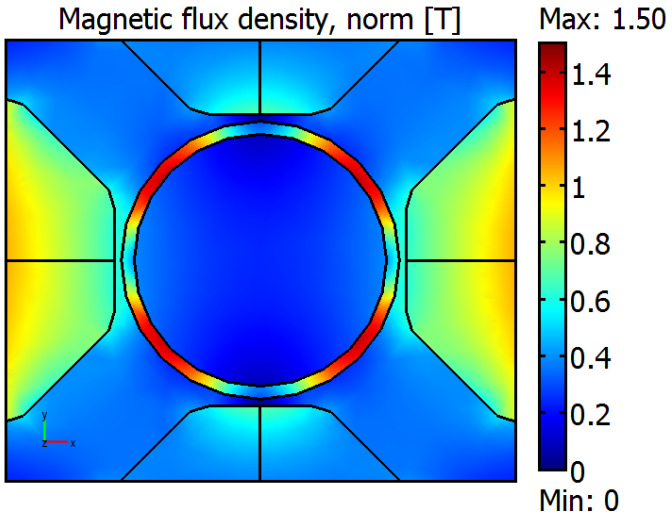

Figure 7.17: COMSOL simulation of the magnetic field generated by the electromagnet from Figure 7.15 with $40A$ applied. Furthermore a $44mm$ tube is placed in between the poles.

The tube is modelled as an arbitrary ferromagnetic material, that is $\chi_M > 1$ or $\mu_r > 2$. From Figure 7.17 it is evident that the inserted tube acts as a shunt for the magnetic field without changing the strength in origo, however. This was validated theoretically by measuring the field generated with $40A$ applied to the electromagnet with and without a steel tube inserted. The field strength values obtained inside of the walls of the tube ranges as high as $1.2T$. This increase in the field strength in the gap between used and unused cores compared to the previous simulation is expected as the medium overall has a higher permeability. In Figure 7.16 the surrounding mediums all consist of nonmagnetic materials, $\mu_r \approx 1$, whereas in this latter the tube acts ferromagnetic. It does, however, not seem likely that the field should rise to such a high level in the gap even though a slightly magnetic medium is added.

[7] The reason the diameter is adjusted to $44mm$ is to avoid direct contact with the electromagnet in the simulation.

7.4 The Complete SMOKE Setup

The SMOKE setup designed in this project is made compatible with an existing vacuum chamber which provides the possibility for surface characterization via STM. This allows for the determination of the magnetic properties associated with different thin film structures. Cooling using liquid N_2 and resistive heating via a W filament are made available making it possible to characterize the temperature dependence of the magnetic properties, e.g. determination of the Curie point.

The electromagnet used is a quadrupole which allows for both longitudinal and polar SMOKE measurements, and it is capable of producing a field strength of app. $200T$ in the center.

A SolidWorks illustration of the complete SMOKE setup is seen in Figure 7.18 along with the end of the preparation chamber on which it is attached.

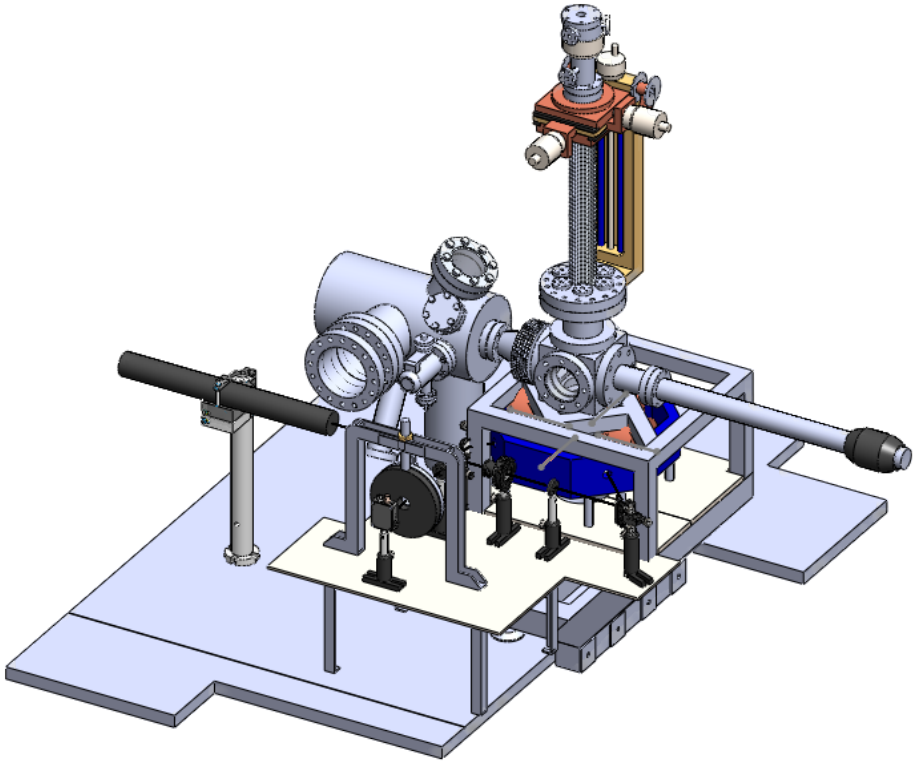

Figure 7.18: An illustration of the complete SMOKE setup attached to the preparation chamber.

Surface Magneto-Optic Kerr Effect Setup

8

This chapter serves as a validation of the system developed in the pervious chapter. This involves testing of the equipment and an evaluation of possible lacks the system may contain.

8.1 UHV Smoke Setup

In Cha. 7 a detailed description of the system created in order to adapt SMOKE to the existing UHV chamber is introduced. This includes detailed blueprints for all the separate vacuum components, an illustration of how the optical components are placed, and finally a description of the custom ordered quadrupole electromagnet.In this section the equipment utilized to control the setup is introduced.

The SMOKE setup is controlled in the same manner as in Sec. 6.2 with the introduction of relays between the power supply and the electromagnets in order to easily invert the polarity of the power supply and hence the magnetic field. Handling the relays is carried out using the digital output of the DAQ card, however, the electric effect supplied by the card is insufficient to switch a relay. Based on this a so-called stepper is introduced. A schematic of the setup is presented in Figure 8.1:

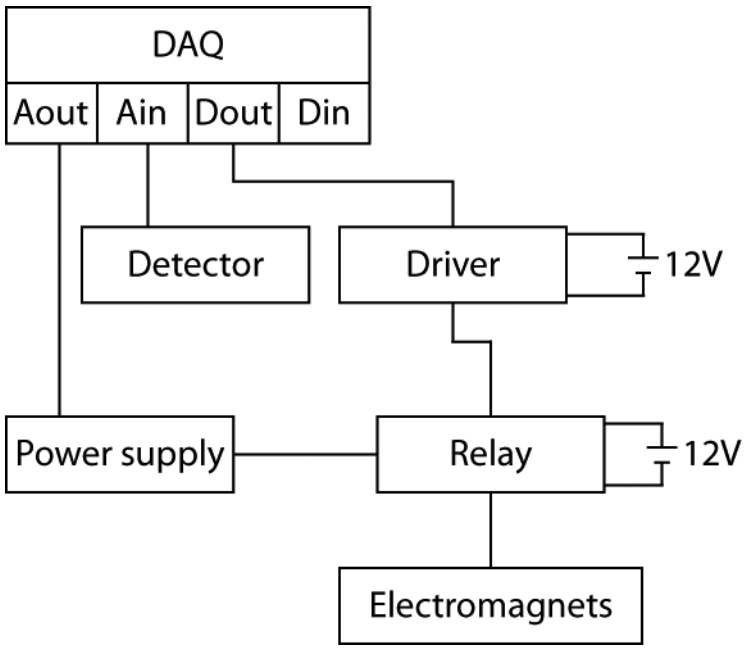

Figure 8.1: Schematic illustrating the electronics used for controlling the SMOKE setup.

Principally a relay is an electrically operated switch, where the switching is carried out by applying a current to an electromagnet. When a magnetic field is generated by the electromagnet a *Fe* armature is displaced towards a metallic contact creating an electric connection. Whenever the electromagnet is demagnetized a spring connected to the armature ensures zero connection through the relay.

Therefore in order to always gain a connection through the relay arrangement a constant $12V$ DC is supplied, as illustrated in Figure 8.1. Whenever the current direction needs to be switched another $12V$ DC needs to be applied, this second current is supplied by the stepper. The functionality of the stepper is to "upscale" the $5.5V$ signal from the DAQ card to the $12V$ signal used to switch the relays.

Conclusively the direction of the current is inverted by supplying the stepper with a digital signal. This significantly simplifies the repetition of hysterisis loops, as a change of field direction only requires supplying the stepper with a digital signal. Therefore the recording of a large amount of hysterisis loops in order to limit noise is significantly simplified.

Controlling the power supply and relay as well as obtaining data from the detector is as before mentioned carried out with a DAQ card. In order to control the DAQ card a piece software is written in Visual C-sharp, an image of the interface of the program is seen in Figure 8.2.

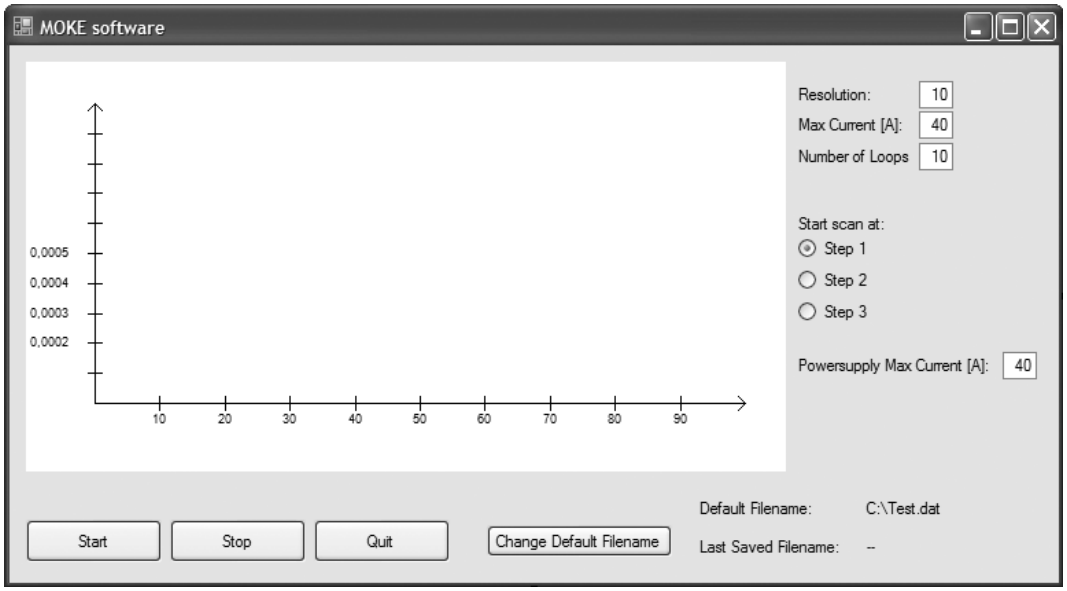

Figure 8.2: Interface of the program written in Visual C-sharp for control of the SMOKE setup.

8.2 Evaluation of Vacuum Components

The total SMOKE system presented in Figure 7.18 contains different components and application possibilities. These need to function properly to enable their usage in SMOKE characterization.

Most crucial is the overall vacuum performance, assembling a setup of this magnitude will without doubt result in a few mounting errors. Accordingly the system is pumped and controlled for leaks repeatedly until a satisfactory performance is observed. The final result is a system durable to the bottom of the $10^{-10} mbar$ range which is the same as the existing system without the SMOKE setup attached. This is naturally very satisfactory as the SMOKE system in itself does not require additional pumping.

The cryostat and the sampleholder are fabricated by the group itself, based on this a thorough investigation and characterization of their abilities is needed.

8.2.1 Cryostat and Sampleholder Characterization

The method used for characterizing the cryostat is simply to fill the reservoir with liquid *N* while monitoring the temperatur change using the thermocouple mounted on the sampleholder. After reaching a minimum value where the *Cu* rod in the bottom of the cryostat has reached a minimum temperature the temperature is raised by supplying a current to the sampleholder filament. In Figures 8.3 and 8.4 the curves are presented.

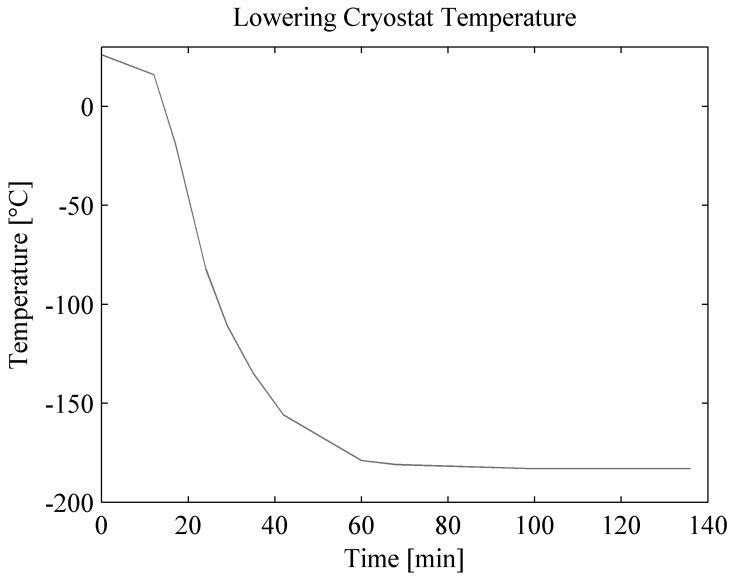

Figure 8.3: Curve illustrating the cooling of the cryostat using liquid *N*. The cryostat was filled with liquid *N* and afterwards left alone to stabilize at the lowest possible temperature.

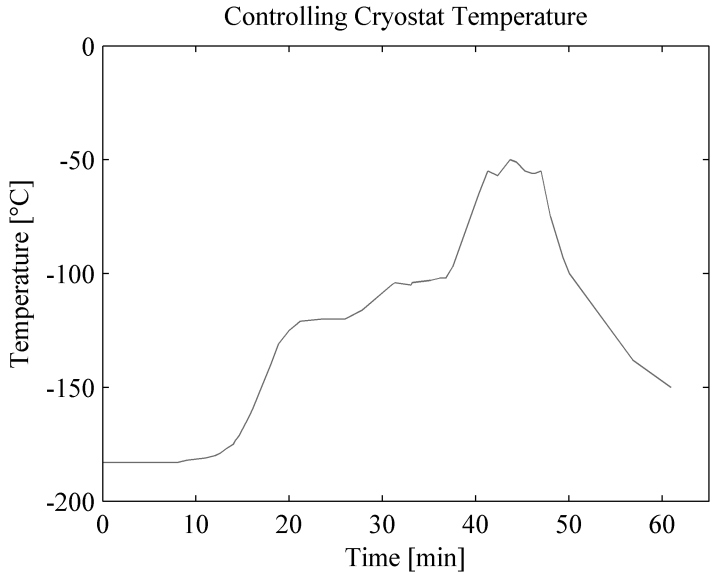

Figure 8.4: Curve illustrating the effect of heating the filament on the sampleholder when the copper reservoir is cooled to $-183°C$. The plateus indicate values where the temperature is kept steady on purpose.

In Figure 8.3 the current temperature is plotted against the time from the point where the cryostat is filled with liquid N. After more than two hours the cryostat temperature remains steady at a minimum value of $-183°C$. This point require only about an hour to reach. Conclusively the cooling concept of the cryostat is well-functioning.

By adding a current to the filament on the sampleholder it is possible to add a counterheat to the cooling of the reservoir. This is carried out initially by applying a small current and raising it to a degree where the temperature gradient is satisfactory. When reaching a desired temperature the current is modulated in order to remain steady, see Figure 8.4. In the figure the temperature is initially raised from $-183°C$ in order to identify the current needed. Naturally the current needed varies with the increasing temperature, accordingly the current is modulated throughout the curve in order to ensure a continuous increase. The plateus indicate areas where the temperature was kept steady to ensure it was fully controllable. Finally after reaching $-50°C$ further heating was stopped in order to investigate the recooldown process. As is seen in Figure 8.4 the sampleholder temperature quickly drops to $-150°C$.

Control of the temperature is by all means a simple process which could easily be governed by the Eurotherm presented in Sec. 7.2.5. Furthermore the temperature is easily kept steady to a degree where several hysterisis loops could be performed without significant temperature deviation.

8.3 Magnetic Properties of *Co* Nanostructures

In order to validate the SMOKE system developed as a viable method for characterizing ferromagnetic nanostructures a sample consisting of a nonmagnetic substrate with a ferromagnetic material deposited on top is fabricated. Initially it was desired to characterize the distinctive triangular islands *Co* form when deposited on $Cu(111)$ at room temperature (RT). But due to lack of both time and access to a $Cu(111)$ substrate mounted on a nonmagnetic flag another sample is considered. Measuring on this sample purely serves as an evaluation of the system, leaving the actual interpretation of magnetic properties for more well executed experiments.

The sample inspected as a means to validate the system as applicable is *Co* deposited on an $Ag(111)$ substrate. This particular substrate is used as it is already mounted on a suitable nonmagnetic sample flag, and *Ag* is nonmagnetic and similar to *Cu*.

8.3.1 *Co* Thin Film on *Ag(111)*

The sample is prepared following the same steps as presented in Sec. 9.1.2 for *Co* deposited on $Cu(111)$. An STM image of the clean $Ag(111)$ crystal is presented in Figure 8.5.

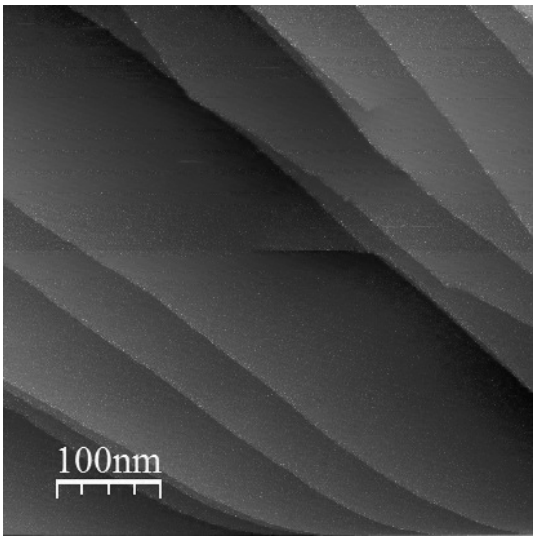

Figure 8.5: STM image of $Ag(111)$ cleaned using *Ne* sputtering as described in Sec. 9.1.2.

As is seen in the figure the *Ag* surface is primarily dominated by terraces. This is certainly useful as step sites often presents an area with increased reactivity and accordingly attracts atoms deposited on the surface. Naturally this latter situation is not desired unless one specifically wants to investigate the magnetic properties of metals adsorbing on step sites. Furthermore the $Ag(111)$ surface presented in Figure 8.5 appears, for the intended purpose, clean of any unwanted materials. The

purity demands are not in the present essential as the goal is simply to validate the setup.

In Figure 8.6 the STM image of the $Ag(111)$ crystal with *Co* deposited is presented.

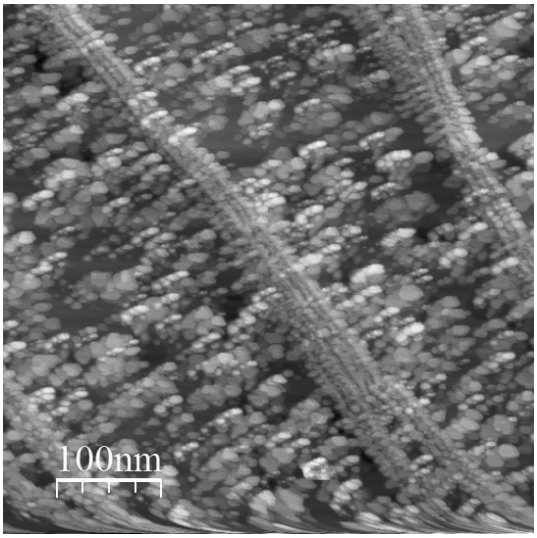

Figure 8.6: STM image of *Co* deposited on $Ag(111)$ at RT.

The sample is fabricated at $T_s = 26°C$ with a flux of app. $13.5nA$ for $47s$. As mentioned earlier the *Co* is clearly seen to nucleate around step sites, but due to the large terraces and the large amount *Co* deposited the *Co* seems well distributed on the crystal.

In Figure 8.7 the histogram for the height distribution of the sample is presented.

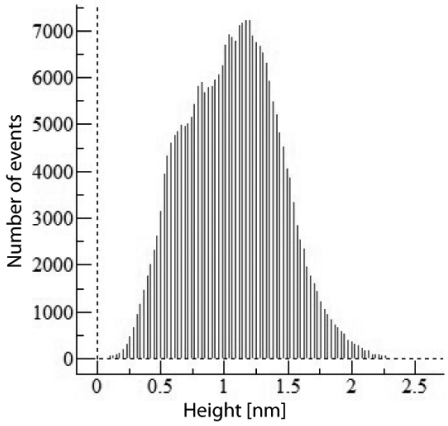

Figure 8.7: Histogram of the STM image presented in Figure 8.6. Using WSxM the extrema around $1.25nm$ is identidifed as the substrate.

The extrema seen around a height of $1.25nm$ is identified as the substrate height

using the equalizer in WSxM 5.0[1], accordingly the events recorded above are primarily *Co*. This yields a maximum height of the *Co* formations of app. $1.2nm$ and an average height of app. $0.5nm$. From these numbers the coverage of the $Ag(111)$ crystal is estimated to be app. $2-3ML$. These numbers are supported by profile measurements, which are presented in Figure 8.8.

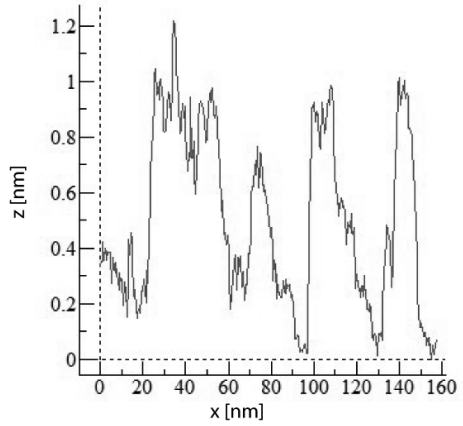

Figure 8.8: Profile measurement across the STM image presented in Figure 8.6. The profiling is conducted across step sites and areas of high intensity.

8.3.2 Magneto-Optic Response from *Co* on *Ag(111)*

Measuring the magneto-optic response is sometimes a troublesome process due to the intensity of the signals handled. Normally one operates extremely close to the total extinction limit, as presented in Cha. 5, which renders noise an important factor. Based on this the noise contributions in the setup are analyzed before actually measuring hysterisis loops.

Initially the optics are aligned against the *Co* sample presented above and the intensity of the reflected light is simply measured at a small angle δ from total extinctions. The incident light is swapped between p- and s-polarized light, completely in accordance with the method used for actually measuring the magneto-optic response in Cha. 6.

The first observation was an unusally large intensity of reflected light at the detector without an added magnetic field. In fact, after applying a magnetic field and thereby gaining a magneto-optic response it is seen that the SMOKE signal constitute only $\frac{1}{80}$ of the signal detected. Due to the large extinction ratio between the glan-laser polarizers this signal is generated somewhere in the setup. By rearranging the polarizers it is discovered that the rotation of the polarization occurs in the area including the two windows and the sample. That is while the light travels

[1]Software developed by Nanotec Electronica for handling equipment and data within surface probing microscopy techniques.

through the initial window, is reflected from the sample and is transmitted through the second window. From Figure 8.6 it is clear that the surface itself is rough, accordingly the polarization must be rotated during reflection. However, from other sources this error does not seem paramount. From [22] it is learned that even the smallest amount of uneven strain applied to the windows result in the generation of elliptically polarized light. This problem is partly overcome by introducing a compensator[2] into the optical setup. In this case the compensator is chosen as a quarter wave plate ($\lambda/4$) where the angle of incidence decides the phase change of the electric field vector. The compensator is then used in the following way:

1. Before adding the $\lambda/4$-plate to the setup the two polarizers are adjusted successively in order to determine the extinction point, just as described in Sec. 5.5.

2. After reaching the extinction point of the two polarizers, the first polarizer is fixed.

3. Then the $\lambda/4$-plate is introduced after the first polarizer and before the initial window.

4. Now the extinction is further improved by succesive rotation of the $\lambda/4$-plate and the second polarizer.

By following this line of succesive rotation of the components one should reduce the signal generated by the first window. It is noted that ideally the windows should be removed from the UHV setup and tested in isolation for confirmation. And if it proves correct the windows should be replaced.

By minimizing the signal generated around the sample it became possible to more effectively illustrate the magneto-optic response. In Figures 8.9 and 8.10 the magneto-optic response gained by changing the current applied to the electromagnets from $-40A$ to $40A$ is displayed.

[2] In optics a compensator is ordinarily a retarder or wave plate, which is a device that applies a phase change to the incident light and thereby alter the polarization.

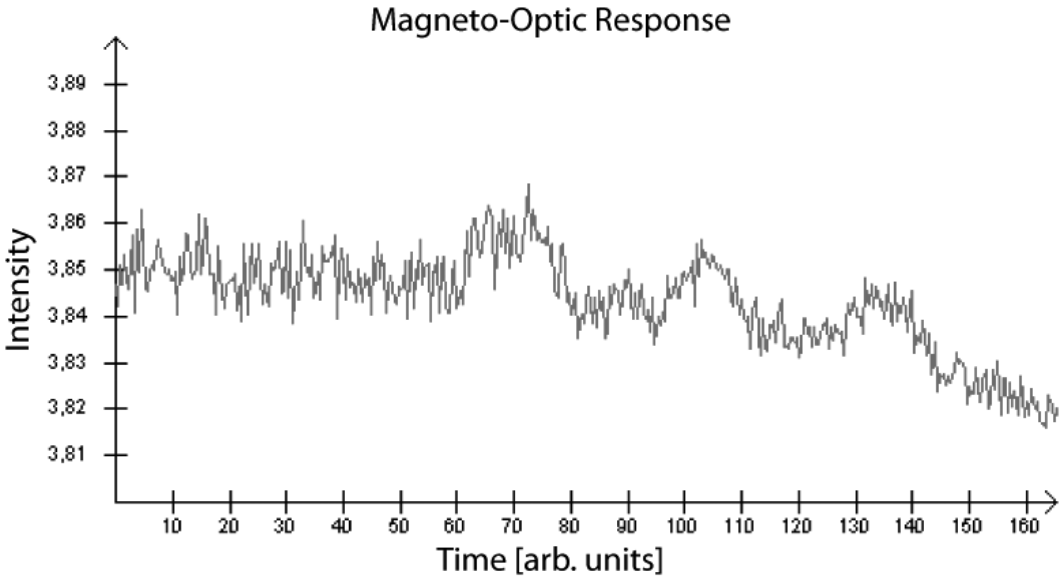

Figure 8.9: Optical response from the sample presented in 8.6. The current applied to the electromagnet is swapped from: $0A$ to $40A$, $40A$ to $0A$, $0A$ to $-40A$ and so on.

This measurement is carried out without the before mentioned $\lambda/4$-plate and with the electromagnet adjusted for the polar geometry. The current applied to the electromagnet is swapped from $-40A$ to $40A$ via $0A$. This corresponds to swapping the applied magnetic field from $-185mT$ to $185mT$, and should thus switch the intensity of the detected light between extrema. The three extrema seen in Figure 8.9 all represent the negative field direction. No visible response was observed in the other direction. The apparent loss of intensity experienced during the measurement is adressed later on. This loss, however, renders the measuring of reference signals from the clean $Ag(111)$ sample nearly impossible. The oscillating response gained when measuring on clean $Ag(111)$ neither confirm nor dismiss the response observed on *Co*. In the present it is merely accepted that *Ag* does not contribute to the magneto-optic response. In Figure 8.10 the same measurement is carried out with the $\lambda/4$-plate inserted.

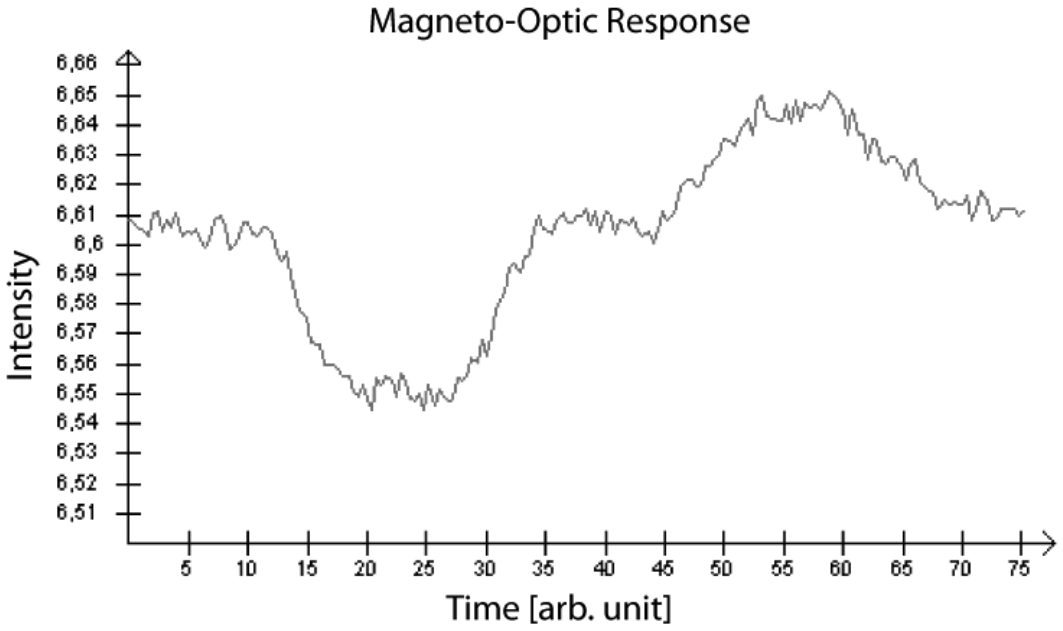

Figure 8.10: Same measurement as in 8.9 but with the addition of a $\lambda/4$-plate to the setup.

The enhancement from the use of the $\lambda/4$-plate is evident from the beginning. Apart from significantly reducing the intensity at the detector[3], the magneto-optic response is now present in both magnetization directions.

The plot in Figure 8.10 clearly indicates the existence of a magneto-optic signal, and the behaviour observed in the figure indicates the possibility of hysterisis loops. However, when trying to succesively reproduce this latter result a large degree of drifting intensities is observed. This is seen in the end of Figure 8.9. In order to investigate this behaviour the detector was set to record the intensity of the reflected light of an unperturbed sample, see Figure 8.11. The behaviour observed in Figure 8.11 cannot, in the present, be explained. Drift varying over this long a period without connection to equipment warmup is not an ordinary event. Ideally all of the optical equipment should be tested separately outside of the setup in order to validate their capabilities. The detector was substituted with another model during measurements, but the results were inconclusive.

By ignoring the drifting intensities and repeating the experiment a number of times it was possible to obtain a hysterisis loop. This is presented in Figure 8.12.

[3]The signals in Figures 8.9 and 8.10 are not directly comparable as the latter is measured with a higher amplification.

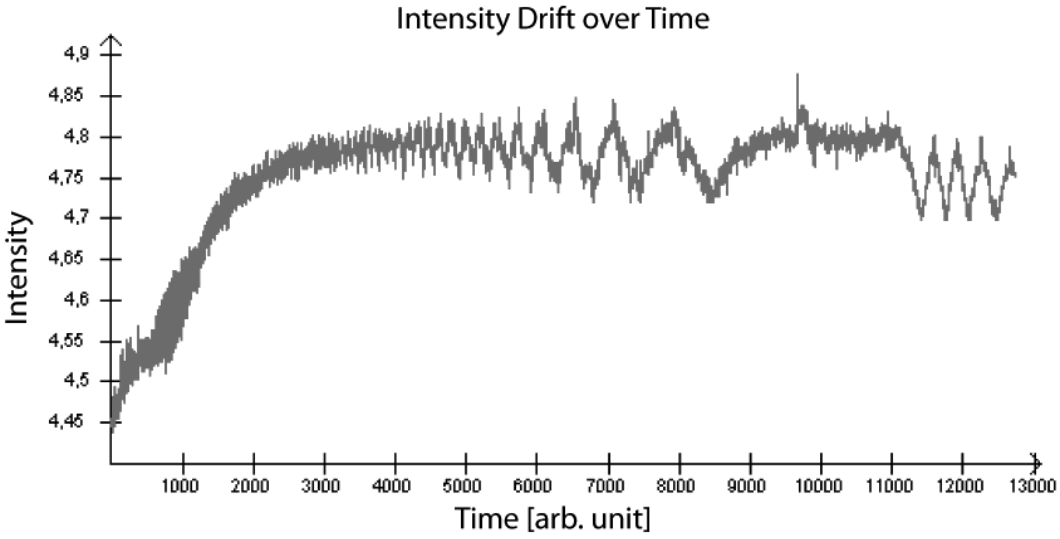

Figure 8.11: Plot of the unexplainable intensity drift observed during SMOKE measurements.

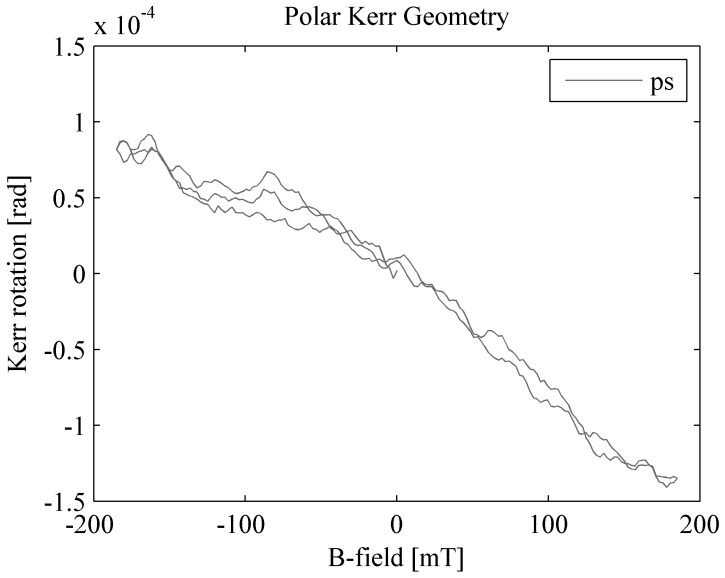

Figure 8.12: Hysterisis loop of the *Co* on $Ag(111)$ sample presented in 8.6. This hysterisis loops is a single mathematically smoothed curve.

The curve in the figure does, to some degree, resemble the s-type curves often experienced in the polar geometry. S-type curves indicate an out of plane easy magnetization axis, as described in Cha. 6. This also supports the lack of results gained through measurements using the longitudinal geometry. The plot in the figure is a single measurement, ordinarily one averages across several loops in order to reduce the effect of noise. This is not possible in the present due to the before mentioned intensity drift. It is therefore not possible to estimate the magnetic properties, like the coercive field, to a satisfactory degree. One observation which seems possible is to estimate the saturation field, but on either side the loop seems to be slanted.

Accordingly $185mT$ may not be enough to reach saturation.

8.4 Necessary Adjustments to the SMOKE System

Overall the capabilities of the system has been proved, the method itself is validated outside of vacuum in Cha. 6 and the response is identified in Figures 8.9 and 8.10. Inspite of a significant drift in the measured intensity it was possible to obtain a curve resembling a hysterisis loop, see Figure 8.12. However, in order to fully gain the ML sensitive method for magnetic characterization the noise needs to be reduced or the magneto-optic signal increased. Furhermore the unexplainable drifting of intensity needs to be identified and removed. Finally replacing the windows, and thereby limitting the change in polarization created before and after the sample, may yield significant improvements.

Perspectives 9

In this chapter the perspectives of using the SMOKE setup developed in this project are considered. As described in Cha. 8 lack of time and problems with the final measurements rendered it imposible to obtain viable results from well characterized surface structures, e.g. the Co islands mentioned in Cha. 1. This chapter therefore also contains a description of these in order to discuss the potentiel characteristics of these.

9.1 Perspectives for the SMOKE Setup

As concluded in Cha. 8 the setup is fully compatible with the existing setup, which thus provides the possibility of preparing and characterizing a large variety of samples by varying e.g. coverage and the surface temperature during sample preparation. Capping layers and sandwich structures are similarly obtainable, which is of interest with regard to magnetic data storage.

In addition to these experiments the temperature control in the SMOKE setup has been tested succesfully and thus provides the possibility of characterizing the temperature dependence of the magnetic properties, e.g. determination of the Curie point.

Naturrally the problems described in Sec. 8.3 require some alterations of the setup in order to obtain accurate results, but these are, as described, believed to be associated with windows and optical components, and can thus be remedied without disassembling the entire setup.

9.1.1 Characterization of *Co* using SMOKE

Co has gained much attention in surface science due to the formation of bilayer triangular islands on e.g. $Cu(111)$. As *Co* is ferromagnetic SMOKE can be used to characterize the magnetic properties of these islands. Due to lack of time this characterization has not been conducted during this project, but some consideration has been put into interesting experiments which could e carried out. Specifically measurements using SMOKE to investigate the following had been planned:

- Magnetic properties for *Co* bilayer triangular islands on $Cu(111)$ at RT.
- Temperature dependence and determination of the Curie Point for *Co* bilayer triangular islands on $Cu(111)$

- Effects of a nonmagnetic cappinglayer using *Ag* to cap a surface with *Co* bilayer triangular islands on $Cu(111)$

- Importance of shape by preparing samples with dendritic *Co* islands fabricated below RT and samples with coalesced islands by increased deposition.

In the preparation of these experiments the growth of *Co* on $Cu(111)$ was also investigated, and is hence described in the following.

9.1.2 Growth of *Co* Thin Films on *Cu(111)*

Co does not exist naturally in its pure form, and is mainly produced as a biproduct from mining *Cu* and *Ni*. *Co* is a ferromagnetic metal with the curie temperature $T_C = 1115°C$ and a magnetic moment of app. $1.6\mu_B$ per atom. *Co* is often applied in the creation of resistant and temperature stable alloys. Furthermore due to its manetic properties, it is often employed in permanent magnetic alloys as well.

Co arranges crystallically as *HCP* and *FCC*, with an ideal transition temperature around $450°C$, but due to a low energy difference random intergrowth is common.

Evaporation of *Co* onto a $Cu(111)$ surface leads to epitaxial growth which initially follows the fcc stacking of the $Cu(111)$ surface. In the bulk phase the two materials are completely immiscible at RT, but this does not rule out surface alloying. It has, however, not been observed at RT, but measurements using STM have shown what appears to be alloying at a temperature of $345K$. It has also been noted that when the temperature raises above RT hexagonal vacancy islands have been observed in the uncovered areas of the $Cu(111)$ surface. [20] [23]

The *Co* formation follows the Volmer-Weber[1] growth mode, and the shape of the islands depends on the surface temperature; at low temperatures the islands are dendritic whereas they are triangular at RT. In the low-coverage regime the triangular islands are always $2ML$ high, and after forming across the surface the subsequent layers form ontop of the islands. [20]

The difference in interatomic distances for *Cu* and *Co* is small, $< 2\%$ [8], and as a result of this the *Co* can either continue the fcc stacking of $Cu(111)$ or it can arrange in hcp stacking as $Co(0001)$. Studies using LEED has shown that deposition of up to app. $2ML$[2] favours a continuation of the fcc stacking whilst the surface coverage of hcp domains increases at further deposition and is almost complete at $5ML$. At this point almost the entire surface is covered and the islands coalesce. [12] [19]

[1] Volmer-Weber growth also known as island growth occurs when the overlayer substrate interaction energy is lower than that between neighboring atoms. [18, p. 102]

[2] Here $1ML$ describes a one-to-one atomic ratio in relation to the $Cu(111)$ surface

9.1.3 Bilayer Triangular Islands

The $2ML$ high triangular shaped islands observed on samples prepared at RT, as mentioned above, form as a result of anisotropic corner diffusion. On a close packed $fcc(111)$ surface two kinds of steps can be distingushed; a so-called A-step along a $\{100\}$-microfacet and a B-step along a $\{111\}$-microfacet, see Figure 9.1.

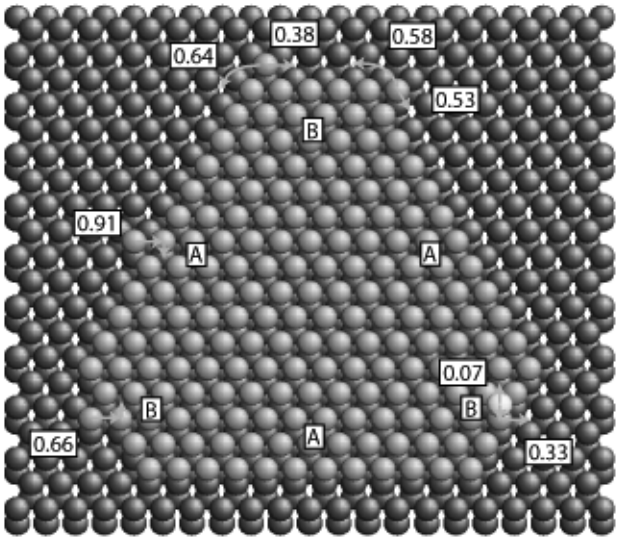

Figure 9.1: Model of monolayered triangular Co island on a $Cu(111)$ surface. Anisotropic corner diffusion makes triangular islands with A-step edges favourable, and an exchange mechanism at the B-step edges gives rise to an upward interlayer transportation of atoms. The energy barrier of relevant events are shown in the boxes. Inspired from [20].

To evaluate the growth, the rate of diffusion of Co atoms needs to be considered. This is done using the Arrhenius equation

$$\nu = \nu_0 \exp\left(\frac{-E}{k_B T}\right), \tag{9.1}$$

where ν is the rate of the proces, ν_0 is the prefactor[3], and E is the energy barrier of the process. If the rate atoms diffusing from A- to B- and B- to A-stepsides are app. equal the resulting growth is hexagonal islands. However, if the growth is dominated by either A to B-diffusion or B to A-diffusion, i.e. the ratio between the corner difusion-energy and the step-energy is markedly lower for one of the directions, then the result is triangular islands like the Co islands on Cu(111) (A to B-diffusion).

To elaborate, the energy barriers of the individual processes need to be considered. These have been calculated in Ref. [20], and appear from the Figures 9.1 and 9.2. When a Co atom travels along an A-step edge it must overcome a barrier $E_A = 0.53eV$. At a corner it can either diffuse back or it can overcome a barrier

[3]The prefactor is in units of Hz and describes the number of events per second that can result in a reaction or not. In [20] the prefactor of all events is taken to be 10^{12}.

$E_{AB} = 0.58eV$ to hop across the corner to the B-step edge. The ratio of the two processes are found using Eq. (9.1):

$$\begin{aligned}\frac{\nu_A}{\nu_{AB}} &= \exp\left(\frac{E_{AB} - E_A}{k_B T}\right) \\ &\approx 0.15\end{aligned}$$

where the prefactors are considered equal and $T = RT$. Making the same considerations for an atom on a B-step edge, where the energies involved are $E_B = 0.38eV$ and $E_{BA} = 0.64eV$, yields a ratio

$$\frac{\nu_B}{\nu_{BA}} \approx 5 \cdot 10^{-5}.$$

The conclusion to these results is that at RT the atoms only diffuse around corners from A-step edges to B-step edges, and the result is triangular islands with A-step edges.

The reason the islands grow to bilayer height across the surface before starting a third layer can also be found by considering the energy barriers of the possible processes involved, see Figure 9.2. To get ontop of the first layer an atom can either

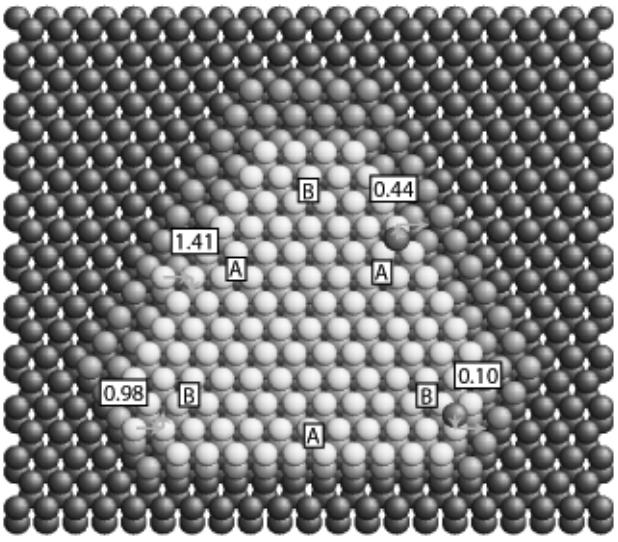

Figure 9.2: Model of bilayered triangular Co island on a $Cu(111)$ surface. The energy required for an atom to move from the second to the third is too high for the proces to take place, and as a result all places on the second layer are occupied before a third layer can start to form resulting in bilayered islands. Inspired from [20].

land on an island or move up via an exchange mechanism, in which another atom traveling alongside the edge takes its place as it moves up. The energy barriers are $0.91eV$ and $0.66eV$ at A- and B-step edges respectively, which for an A-step exchange is too high for the process to take place at RT. An atom ascended at a B-step edge can either descend ($0.33eV$) or move away from the edge ($0.07eV$), and with a relative probability of the order 10^{-5} the atom is not likely to descend. This shows

that Co atoms can reside on a $1ML$ Co island due to a net upward transportation at the B-step edges. These atoms then have a possibility to collide on the island to form a dimer, which can serve as a nucleationsite for the second layer, as it has a binding energy of $1.5eV$, and hence does not dissosiate.

If the same considerations are performed for a third layer the exchange barriers for upward transportation at both A- and B-step edges are too high ($1.41eV$ and $0.98eV$ respectively) to take place at RT. Atoms landing ontop of a second layer can diffuse around on the layer ($0.07eV$) or descend via exchange at an A- or B-step edge ($0.44eV$ and $0.10eV$). Both of these processes take place at RT, hence there is a transportation of atoms from the third to the second layer, but not the opposite. This results in atoms occupying all availible sites in the second layer and thereby the formation of bilayered islands in accordance with experiments, which is seen in Figure 9.3. The figure also shows the triangular islands have one of two different

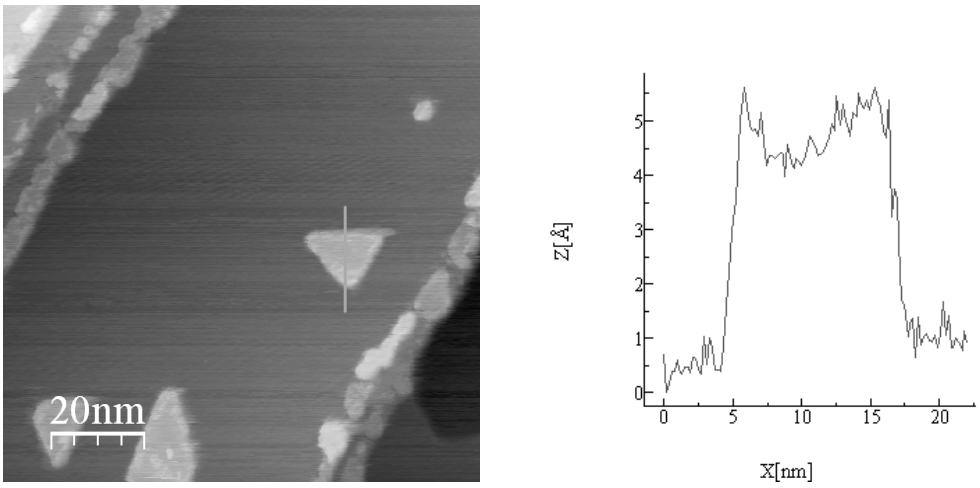

(a) (b)

Figure 9.3: Results of a STM scan of Co islands on a $Cu(111)$ suraface. 9.3(a) is the converted plane of the measurement from which it is clear that the Co grows as triangular islands. 9.3(b) is a profile of height along the line in 9.3(a) and from this the height is seen to be app. $4Å$ corresponding to $2ML$.

orientations, which is explained as follows. When an atom lands on a $fcc(111)$ surface it can land in either a fcc-site continuing the stackingsequence of the substrate $ABCa$ or it can land in a hcp-site and thereby create a stackingfault $ABCb$. As mentioned a continuation of the fcc stacking is favoured in the low-coverage domain, so the stacking will be $ABCabcabc$ and $ABCbacbac$. [8] [12]

Structures formed from fcc- and hcp-sites differ in the way that the spatial directions of the A- and B-steps are switched, so if the growth is triangular islands formed on hcp-sites will have opposite orientations, as seen in Figure 9.4. Studies using STM has shown a relative amount of triangles on fcc- and hcp-sites to be 0.65 and 0.35. [20]

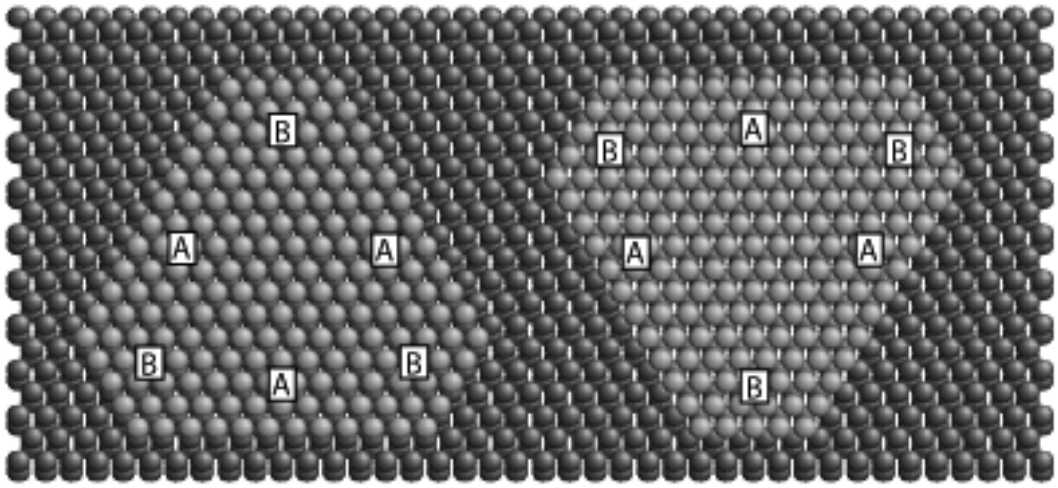

Figure 9.4: Model of monolayered *Co* islands on a $Cu(111)$ surface. Islands formed on fcc- and hcp-sites have different orrientations because the *A*- and *B*-steps switches.

Conclusion 10

The main motivation behind the project was to develop a versatile setup for characterizing magnetic nanostructures. This is due to the huge interest in magnetic structures for magnetic storage and sensor applications. In this area *Co* deposited on nonmagnetic substrates in monolayer thicknesses and capped with a nonmagnetic layer has gained a significant interest as the latter tunes the properties of the perpendicular magnetic anisotropy and magnetic reorientation phase transition. Based on this two problematics were formulated as:

1. *Development of a versatile surface magneto-optic Kerr effect setup which may be adapted to the existing ultra high vacuum chamber.*
2. *Validation of the surface magneto-optic Kerr effect setup through Kerr measurements. And if the time allows for it a characterization of the magnetic properties of bilayer triangular Co islands, and the effects of capping the islands with a nonmagnetic metal.*

The initial problematic is the primary objective, whereas the latter, apart from interest in magnetic structures, serves as a validation of the setup developed. Naturally several theoretical aspects needs to be investigated in order to develop a satisfactory SMOKE setup, including: fundamental magnetic definitions, magnetic behaviour in systems of reduced dimensions and a definition of the magneto-optic Kerr effect. Furthermore the theory is tested in practice through a simplified setup constructed in free air.

To establish a fundamental knowledge of magnetic behaviour the concepts of magnetic dipoles and magnetization are defined. Based on these the various magnetic classifications, dia-, para-, and collective magnetism, are defined through semiclassical and quantum mechanical considerations. Finally the optics of magnetic materials are outlined using the dielectric tensor.

In order to understand the concept of magnetism in reduced dimensions, the magneto anisotropy energy is used to describe anisotropy in thin films. This includes both the magneto crystalline anisotropy and the shape anisotropy of thin film structures. Structures with reduced dimensions generally displays a significant surface contribution, accordingly this is introduced into the model allowing for a qualitative description of magnetism in thin films.

To gain a proper insight into the concept of the magneto-optic Kerr effect, the phenomena is investigated through a quantum mechanical and an optical approach. The latter is the most detailed where the magneto-optic response is derived for a layered structure of arbitrary thickness. This is done by introducing a thin limit approximation where the total film thickness is far below the wavelength of the

incident light. Using this approximation the Kerr rotation is derived from the reflection fresnel coefficients, and is presented in Eqs. 5.8a and 5.8b. A formal definition of the Kerr angle is carried out ab initio, and the Kerr rotation, used in Kerr measurements, is derived in Eq. 5.3. Afterwards a setup utilizing this phenomena for magnetic characterization is presented schematically in Figure 5.3.

In order to validate the approach of the surface magneto-optic Kerr effect setup a simplified setup is constructed outside of vacuum. It comprises the same basic optical equipment, but is centered around a simple electromagnet geometry at our disposal. The chapter serves as a preliminary validation of the concept, and in addition to this several aspects are investigated. These are the longitudinal magneto-optic response of: a single 40*nm Fe* layer, 40*nm* oxidized *Fe*, and *Fe* capped with 20*nm Sn*. For all of the samples incident s- and p-polarized light are used. Hysterisis loops are recorded for the 40*nm Fe* sample and the sample capped with *Sn*, seen in Figures 6.10, 6.11, 6.13, and 6.14. The sample with oxidized *Fe* displayed no ferromagnetic behaviour at all. This is in accordance with the theory presented earlier and thus validates the concept as a method for characterizing magnetic structures. Furthermore it is observed that capping the ferromagnetic material with a nonmagnetic modulates the magnetic properties of the underlying material. This is best seen in the response from p-polarized light, which changes drastically. Moreover the coercive field is observed to change from 8*mT* for the 40*nm Fe* sample to 14.5*mT* for the capped sample. For all of the samples the easy magnetization axis is identified as an in-plane axis, which is in accordance with other sources, and the theory presented in Cha. 4.

The theory investigated and the experiments carried out yielded significant information to the design part of the project. To further improve the setup, simulations of magnetic field characteristics are created in COMSOL multiphysics, presented in Figures 7.16 and 7.17. During the design phase several different concepts were considered, distinquished by their position relative to the existing setup: as a part of the analysis chamber, as a part of the preparation chamber, or placing it separately at the end of the system. All have pros and cons, the latter, however, seems the most reasonable choice with regard to the possible geometries. Based on this position the system is created around a custom designed quadrupole electromagnet fabricated by Danfysik. This electromagnet was custom ordered in order to gain the highest possible field homogeneity while having the possibility of a field of 200*mT* at the center of the pole gap. The electromagnet received, however, displayed a large degree of inaccuracies. Apart from uneven pole faces and gaps the core material was unsatisfactory for Kerr effect measurements due to remanence. These problematics with the electromagnet have been recognised by Danfysik, and will be remedied. But due to lack of time this is not done until after the completion of this project. For now the remaining setup is assembled with the possibility of sample heating and cooling through a custom made cryostat. An illustration of the total setup mounted on the UHV system is seen in Figure 7.18.

In order to validate the design and assembling of the system all separate parts are tested. This includes the validation of the: UHV performance, temperature control of the cryostat, and its abilities to record the magneto-optic response.

The base pressure of the UHV system after attaching the SMOKE setup is the

same as before. Based on this it is clear that no modifications are needed with regard to pumping capacity of the setup.

Testing of the cryostat capabilities is carried out by lowering its temperature as much as possible using liquid N. When reaching the minimum temperature, which was identified as $-183°C$, the sample holder filament is counterheated by applying a current. This is done to investigate the degree of control one has over the sample temperature during SMOKE measurements. It is found that by simple modulation of the current the sample temperature is easily kept constant giving time to measure several full hysterisis loops.

Finally in order to evaluate whether the system is applicable for SMOKE the magneto-optic signal generated in a sample consisting of a $Ag(111)$ substrate with Co deposited on top is measured. During these measurements it is found that the windows into the vacuum chamber probably alters the state of polarization and thus decreases the overall signal. This is partly solved by introducing a compensator into the optical setup in form of a $\lambda/4$-plate. Apart from the discrepancy created in the windows a large degree of drifting is observed in the intensity. This latter error needs to be solved before the system is fully applicable for SMOKE measurements. Inspite of these problematics a magneto-optic response is observed in Figures 8.9 and 8.10 and a hysterisis loops is recorded for the polar Kerr geometry, see Figure 8.12.

Generally SMOKE measurements presents an interesting method for probing magnetic properties of nanostructures. Based on this a short description of further possible perspectives is presented. It is centered around the distinctive triangular islands Co form when deposited on $Cu(111)$ at room temperature.

Bibliography

[1] Bernhard halle nachfolger gmbh. On the web: http://www.b-halle.de.

[2] Delta elektronika. On the web: http://www.delta-elektronika.nl.

[3] Goodfellow. On the web: http://www.goodfellow.com/.

[4] S.D. Bader, E.R. Moog, and P. Grünberg. Magnetic hysterisis of epitaxially-deposited iron in the monolayer range: A kerr effect experiment in surface magnetism. *Journal of Magnetism and Magnetic Materials*, 53:L295–L298, 1985.

[5] J. Bork, L. Diekhöner, Z. Li, and J. Onsgaard. Electronic structure and ordering of multilayers of co and ag on cu(111) investigated by photoelectron spectroscopy. *Surface Science*, 604:1536–1541, 2010.

[6] F.C. Chen, Y.E. Wu, C.W. Su, and C.S. Shern. Ag-induced spin-reorientation transition of co ultrathin films on pt(111). *Physical Review B*, 66:1–5, 2002.

[7] J. Dahl. *The Quantum World of Atoms and Molecules*. World Scientific Publishing Co. Pte. Ltd., 2001. ISBN: 981-02-4565-3.

[8] J. de la Figuera, J. E. Prieto, C. Ocal, and R. Miranda. Scanning-tunneling-microscopy study of the growth of cobalt on cu(111). *Physical Review B*, 47(19):13043–13049, 1993.

[9] I. Flis-Kabulska. Oxide growth on evaporated thin film and bulk iron exposed to humid air and hcl or hno3 vapours. *Journal of Electroanalytical Chemistry*, 508:89–96, 2001.

[10] M. Getzlaff. *Fundamentals of Magnetism*. Springer-Verlag, 2008. ISBN: 978-3-540-31150-8.

[11] J.R. Hampton, J. Martínes-Albertos, and H.D. Abruña. Development of a versatile smoke system with electrochemical applications. *Review of Scientific Instruments*, 73(8):3018–3021, 2002.

[12] K. Heinz, S. Müller, and L. Hammer. Crystallography of ultrathin iron, cobalt and nickel films grown epitaxially on copper. *Journal of Physics: Condensed Matter*, 11:9437–9454, 1999.

[13] M. Kisielewski, A. Maziewski, and M. Tekielak. New possibilities for tuning ultrathin cobalt film magnetic properties by a noble metal overlayer. *Physical Review Letters*, 89(8), 2002.

[14] C. Kittel. *Introduction to Solid State Physics*. Wiley and Sons, Inc, 2005. ISBN: 0-471-41526-X.

[15] M.V. Klein and T.E. Furtak. *Optics*. Wiley and Sons, Inc, 1986. ISBN: 0-417-87297-0.

[16] J.W. Lee, J.R. Jeong, D.H. Kim, J.S. Ahn, J. Kim, and S.C Shin. Three-configurational surface magneto-optical kerr effect measurement system for an ultrahigh vacuum in situ study of ultrathin magnetic films. *Review of Scientific Instruments*, 71(71):3801–3805, 2000.

[17] A. Lehnert, P. Buluschek, N. Weiss, J. Giesecke, M. Treier, S. Rusponi, and H. Brune. High resolution in situ magneto-optic kerr effect and scanning tunneling microscopy setup with all optical components in uhv. *Review of Scientific Instruments*, 80, 2009.

[18] Hans Lüth. *Solid Surfaces, Interfaces and Thin Films*. Springer, 4th edition, 2001. ISBN: 3-540-42331-1.

[19] S. Müller, G. Kostka, T. Schäfer, J. de la Figuera, J. E. Prieto, C. Ocal, R. Miranda, K. Heinz, and K. Müller. The structure of co films on cu(111) up to 15 ml. *Surface Science*, 352-354:46–49, 1996.

[20] N. N. Negulyaev, V. S. Stepanyuk, P.Bruno, L. Diekhöner, P. Wahl, and K. Kern. Bilayer growth of nanoscale co islands on cu(111). *Physical Review B*, 77:125437–1–125437–7, 2008.

[21] NuDAQ. Pci 9111hr user's guide. On the web: www.nudaq.com.

[22] K. Pedersen. *Photoelastic Properties of Aluminum and Copper Studied by Ellipsometry*. PhD thesis, Physics Laboratory, University of Aalborg, 1986.

[23] M. Ø. Pedersen, I. A. Bönicke, E. Lægsgaard, I Stensgaard, A. Ruban, J. K. Nørskov, and F. Besenbacher. Growth of co on cu(111): subsurface growth of trilayer co islands. *Surface Science*, 387:86–101, 1997.

[24] T.G. Pedersen and L. Diekhöner. Electric, optical and magnetic properties of nanostructures. Compendium created at Aalborg University, 2009.

[25] Z.Q. Qiu and S.D. Bader. Surface magneto-optic kerr effect. *Review of Scientific Instruments*, 71(3):1243–1255, 2000.

[26] F.W. Sears and G.L. Salinger. *Thermodynamics, Kinetic Theory, and Statistical Thermodynamics*. Addison-Wesley Publishing Company, 1986. ISBN: 0-201-06894-X.

[27] R. Serway and Jewet. *Physics for Scientists and Engineers*. Thomson - Brooks/Cole, 2004. ISBN: 0-534-40949-0.

[28] J.M. Thijsen. *Computational Physics*. Cambridge University Press, 2007. ISBN: 0-521-83346-9.

[29] Thorlabs. On the web: http://www.thorlabs.de. Supplier of optical equipment.

[30] V. Usov, S. Murphy, L.Seravalli, and I. V. Shvets. Developments in surface magneto-optical kerr effect setup for ultrahigh vacuum analysis of magnetic ultrathin films. *Review of Scientific Instruments*, 76:046102–1–046102–3, 2005.

[31] Wikipedia. The free encyclopedia. On the web: www.wikipedia.org.

[32] J. Zak, E.R. Moog, C. Liu, and S.D. Bader. Universal approach to magneto-optics. *Journal of Magnetism and Magnetic Materials*, 89:107–123, 1990.

[33] J. Zak, E.R. Moog, C. Liu, and S.D. Bader. Magneto-optics of multilayers with arbitrary magnetization directions. *Physical Review B*, 43(8):6423–6429, 1991.

List of Components

A

This appendix introduces the equipment not designed by the group. This includes optical components, vacuum equipment and electronics used for data management.

A.1 Optical Components

In Sec. 5.4 the concept of SMOKE is presented. Here the optical equipment used is described in detail.

A.1.1 Light Source

As a light source a high power HeNe laser with an output of $5mW$ was used. The full specifications chart is seen in Table A.1.

Model:	GL10
Specifications:	Value:
Wavelength	$632.8nm$
Maximum ouput power	$10.0mW$
Minimum ouput power	$5mW$
Polarization	Linear > 500:1
Mode structure	$TEM_{00} > 99\%$
Beam diameter	$0.8mm$
Beam divergence	$1.01mrad$
Beam drift after 30 min warm-up	$< 0.20mrad$
Long term beam drift	$< 0.02mrad$
Product number	HRP050

Table A.1: Table containing the specifications for the HeNe laser used as a light source in the SMOKE setup. The laser is bought via [29].

A.1.2 Polarizers

The polarizers used in the SMOKE setup are so-called Glan-laser calcite polarizers. The concept of a Glan-laser polarizer or a Glan-Taylor prism in general is to have two right angled prisms of a birefringent material placed as seen in Figure A.1. When incident arbitrarily polarized light hits the angled prism at the interface of the air gap, the light is split into an ordinary and extraordinary ray.

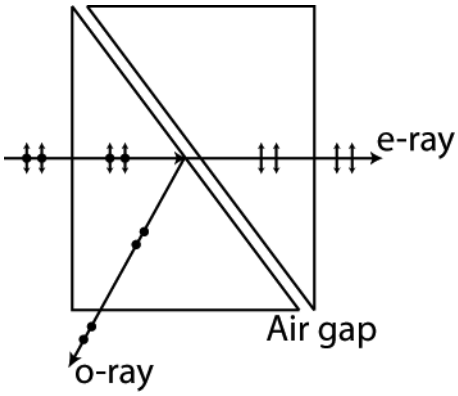

Figure A.1: Illustration of a Glan-Taylor prism. Two angled prisms consisting of a birefringent material are placed with a small air gap between them. Incident arbitrarily polarized light is split into the ordinary and extraordinary ray.

In these particular polarizers the ordinary ray exits the polarizer at an angle of 61° with respect to the polarizer normal. See Figure A.2 for an image of the polarizer and Table A.2 for the full specifications.

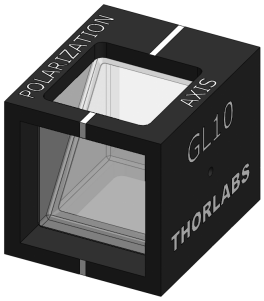

Figure A.2: SolidWorks image of the Glan-Laser polarizer. From [29].

Model:	GL10
Specifications:	Value:
Transmission range	0.35-2.3μm
Extinction ratio	100,000:1
Material	Laser quality natural calcite (low scatter)
Coating	Uncoated
Wavefront distortion	= $\lambda/4$ over clear aperture
Aperture	$10mm \times 10mm$
Prism Dimensions ($W \times L$)	$12mm \times 13.7mm$

Table A.2: Table containing the specifications for the Glan-laser polarizer used in the SMOKE setup. The polarizers are bought via [29].

When it comes to mounting the polarizing prisms two different rotation mounts are used. The polarizer situated before the sample is placed in an ordinary metric

rotation mount called RSP1X15/M from [29] which can be rotated 360°. After the sample, however, precise control of the degree of rotation is needed. As stated in Sec. 5.3 the intensity of reflected light needs to be measured at a small angle δ from total extinction of the incident light. Accordingly, the degree of rotation of the polarizer must be small enough to measure the magneto-optic signal. Based on this a precision rotation mount called MTK 75.113 is used supplied by [1]. The polarizer mount is equipped with a micrometer screw yielding a quantifiable amount of rotation on a small scale. By displacing the screw $0.13mm$ the polarizer is rotated $0.1°$.

A.1.3 Detector

Detection of $632.8nm$ *HeNe* light from a high power laser is easily accomplished using any type of broadband detector. However, the signal measured when using SMOKE is near total extinction, and accordingly the final signal is low compared to the incident signal. Based on this a detector with amplification is necessary. The detector used is a PDA36A *Si* switchable gain detector from [29]. The full specifications are presented in Table A.3 and the responsivity as a function of wavelength in Figure A.3.

Model:	PDA36A
Specifications:	Value:
Photo element	*Si*
Wavelength	$350 - 1100nm$
Detector size	$3.6mm \times 3.6mm$
Gain	$8 \times 10dB$ steps

Table A.3: Table containing the specifications for the PDA36A *Si* detector. The detector is bought via [29].

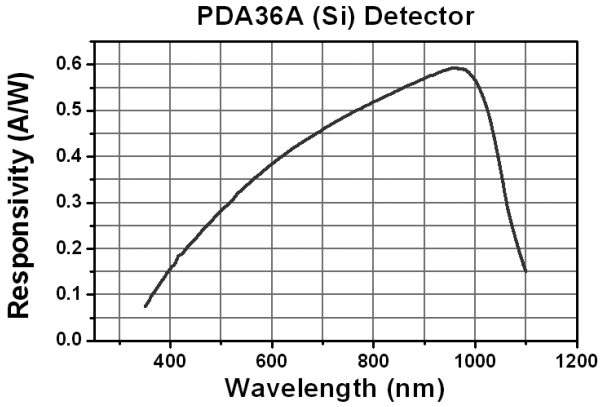

Figure A.3: Responsivity of the detector as a function of wavelength in *nm*. From [29].

A.1.4 Mirrors and Windows

The mirrors used in the SMOKE setup are ordinary broadband dielectric mirrors mounted in three point adjusteble kinematic mirror mounts. Naturally the mirrors are chosen so that they reflect the light from the HeNe source, that is 632.8nm. Both mirrors and mounts are bought via [29] as the previous components and their respective model names are BB1-E02 - Ø1" and KS1 - Ø1".

In order to impose the minimum effect upon the laser light from the windows, specialized laser viewports consisting of strain free quartz is ordered.

A.2 Electronic Components

The SMOKE system developed in Cha. 7 is controlled using electronic equipment. These are presented in detail in the following.

A.2.1 Power Supply

The power supply used for providing the current for the electromagnets is a SM1540 - D from Delta Elektronika, see [2]. This particular power supply is able to deliver a maximum current of 40A and voltage of 15V. The output voltage and current is programmable through an external analog plug in, this analog input is standardised to between 0 and 5V. The output from the power supply relates linearly to the input signal with a nonlinearity below 0.15%. To maintain this low degree of nonlinearity the analog input cable should naturally be shielded. Apart from this the power supply contains functions as: remote sensing, interlock, and protection against overload and short circuits. A detailed specification is seen in Table A.4.

Model:	SM1540
Specifications:	Value:
Efficiency	up to 91% (at full load)
Programming speed	from 3.4ms (optional from 0.2ms)
Analog programming accuracy	from 0.2%
Output voltage stability	6.10^{-5}
Output current stability	9.10^{-5}
Input type	15 pin analog input

Table A.4: Specification for the SM1540 Delta Elektronika power supply used to drive the electromagnets, see [2].

A.2.2 Data Acquisition Card

The data acquisition card applied for controlling the SMOKE system is a PCI-9111HR from NuDAQ. This model is often used for industrial or laboratory pur-

poses e.g. as: an on/off control, communication, period and pulse width measurement etc. Some of the specifications are the following:

- 16*bit* analog input resolution through a 37-pin plug
- Bipolar input signals
- Input Range: $\pm 10V$, $\pm 5V$, $\pm 2.5V$, $\pm 1.25V$, $\pm 0.625V$
- DC-to-DC converter for stable analog source
- 16 digital output channels
- 16 digital input channels
- 4 additional digital input and output channels on the 37-pins plug

Changing between unipolar and bipolar analog input is handled by switching a jumper, the input range is $0V$ to $10V$ and $-10V$ to $10V$ for unipolar and bipolar settings respectively. For further information refer to the PCI-9111HR user guide from NuDAQ [21].

Supplementary Calculations

B

In this appendix selected calculations from the theory of magnetism are presented in more detail.

B.1 Additional Mathematics for Magnetism in Reduced Dimensions

In the review of magnetism in reduced dimensions selected calculations are too tedious to include. These are instead presented in detail in the following.

B.1.1 Directional Cosines

The direction of the magnetization $\vec{m} = \dfrac{\vec{M}}{\left|\vec{M}\right|}$ is given in terms of the directional cosines α_1, α_2, and α_3 as $\vec{m} = \left(\alpha_1, \alpha_2, \alpha_3\right)$, see Figure B.1. The directional cosines

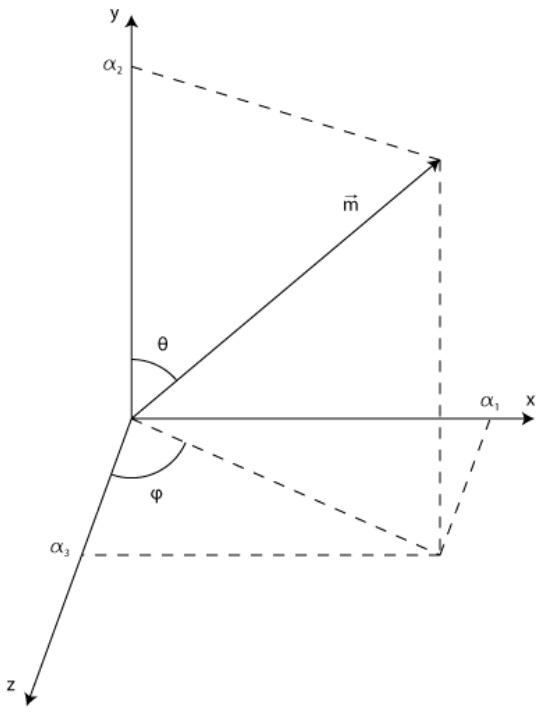

Figure B.1: The direction of the magnetization represented by the directional cosines. Inspired from [10, p. 90].

are defined as:

$$\begin{aligned}\alpha_1 &= \sin\theta\cos\phi \\ \alpha_2 &= \sin\theta\sin\phi \\ \alpha_3 &= \cos\theta,\end{aligned} \tag{B.1}$$

and obey the normalization condition:

$$\alpha_1^2+\alpha_2^2+\alpha_3^2 = 1. \tag{B.2}$$

B.1.2 Elimination of Cross Terms

As a result of Eq. (4.1) cross terms $\alpha_i\alpha_j$, with $i \neq j$, vanish in the summations from Eq. (4.2). This is shown using the second order term as an example:

$$\begin{aligned}\sum_{ij} b_{ij}\alpha_i\alpha_j &= b_{11}\alpha_1\alpha_1 + b_{12}\alpha_1\alpha_2 + b_{13}\alpha_1\alpha_3 + b_{21}\alpha_2\alpha_1 + b_{22}\alpha_2\alpha_2 \\ &\quad + b_{23}\alpha_2\alpha_3 + b_{31}\alpha_3\alpha_1 + b_{32}\alpha_3\alpha_2 + b_{33}\alpha_3\alpha_3 \\ &= b_{11}\alpha_1\alpha_1 + b_{22}\alpha_2\alpha_2 + b_{33}\alpha_3\alpha_3 + \Big(b_{12}+b_{21}\Big)\alpha_1\alpha_2 \\ &\quad + \Big(b_{13}+b_{31}\Big)\alpha_1\alpha_3 + \Big(b_{23}+b_{32}\Big)\alpha_2\alpha_3.\end{aligned} \tag{B.3}$$

The condition in Eq. (4.1) must be fulfilled, hence Eq. (B.3) yields the same result for the angles θ,ϕ and θ',ϕ', which are the directions of $\vec{M}$ and $-\vec{M}$, respectively. From Figure B.1 these are identified as:

$$\begin{aligned}\theta' &= \pi - \theta \\ \phi' &= \pi + \phi.\end{aligned}$$

Replacing the directional cosines in Eq. (B.3) and inserting θ and ϕ and θ' and ϕ', respectively, yields the two expressions:

$$\begin{aligned}E\Big(\vec{M}\Big) &= b_{11}\sin^2\theta\cos^2\phi + b_{22}\sin^2\theta\sin^2\phi + b_{33}\cos^2\theta \\ &\quad + \Big(b_{12}+b_{21}\Big)\sin^2\theta\cos\phi\sin\phi + \Big(b_{13}+b_{31}\Big)\sin\theta\cos\phi\cos\theta \\ &\quad + \Big(b_{23}+b_{32}\Big)\sin\theta\sin\phi\cos\theta \\ E\Big(-\vec{M}\Big) &= b_{11}\sin^2\Big(\pi-\theta\Big)\cos^2\Big(\pi+\phi\Big) + b_{22}\sin^2\Big(\pi-\theta\Big)\sin^2\Big(\pi+\phi\Big) \\ &\quad + b_{33}\cos^2\Big(\pi-\theta\Big) + \Big(b_{12}+b_{21}\Big)\sin^2\Big(\pi-\theta\Big)\cos\Big(\pi+\phi\Big)\sin\Big(\pi+\phi\Big) \\ &\quad + \Big(b_{13}+b_{31}\Big)\sin\Big(\pi-\theta\Big)\cos\Big(\pi+\phi\Big)\cos\Big(\pi-\theta\Big) \\ &\quad + \Big(b_{23}+b_{32}\Big)\sin\Big(\pi-\theta\Big)\sin\Big(\pi+\phi\Big)\cos\Big(\pi-\theta\Big) \\ &= b_{11}\sin^2\theta\cos^2\phi + b_{22}\sin^2\theta\sin^2\phi + b_{33}\cos^2\theta\end{aligned} \tag{B.4}$$

$$- \Big(b_{12}+b_{21}\Big)\sin^2\theta\cos\phi\sin\phi - \Big(b_{13}+b_{31}\Big)\sin\theta\cos\phi\cos\theta$$
$$- \Big(b_{23}+b_{32}\Big)\sin\theta\sin\phi\cos\theta. \tag{B.5}$$

By applying the condition of Eq. (4.1) on Eqs. (B.4) and (B.5) it is clear that all terms with $i \neq j$ vanish as they contains an uneven power of a cosine, which changes sign in a phase change of π.

B.1.3 Explicit Calculation of Eq. (4.13)

To show the validity of Eq. (4.13) it must be shown that:

$$\cos^6\phi - \sin^6\phi - 15\cos^4\phi\sin^2\phi + 15\cos^2\phi\sin^4\phi = \cos 6\phi. \tag{B.6}$$

This is done by rewriting the left side, in the following denoted by Y. Initially all sines are replaced using the following identities:

$$\begin{aligned}\sin^2 x &= -\cos^2 x + 1\\ \sin^4 x &= \cos^4 x - 2\cos^2 x + 1\\ \sin^6 x &= -\cos^6 x + 3\cos^4 x - 3\cos^2 x + 1.\end{aligned}$$

This yields:

$$\begin{aligned}Y &= 2\cos^6\phi - \Big(15\Big(1-\cos^2\phi\Big)+3\Big)\cos^4\phi\\ &\quad + \Big(15\Big(\cos^4\phi - 2\cos^2\phi + 1\Big)+3\Big)\cos^2\phi - 1\\ &= 32\cos^6\phi - 48\cos^4\phi + 18\cos^2\phi - 1.\end{aligned} \tag{B.7}$$

To reduce this further the following addition theorem is used:

$$\cos x\cos y = \frac{\cos\Big(x-y\Big)\cos\Big(x+y\Big)}{2}. \tag{B.8}$$

Setting $x = y = \phi$ in Eq. (B.8) yields:

$$\cos^2 x = \frac{1+\cos 2x}{2},$$

which is used multiple times in Eq. (B.7):

$$\begin{aligned}Y &= 32\cos^4\phi\Big(\frac{1+\cos 2\phi}{2}\Big) - 48\cos^4\phi + 18\cos^2\phi - 1\\ &= \Big(16\cos 2\phi - 32\Big)\cos^4\phi + 18\cos^2\phi - 1\\ &= \Big(16\cos 2\phi - 32\Big)\Big(\frac{1+\cos 2\phi}{2}\Big)\cos^2\phi + 18\cos^2\phi - 1\\ &= \Big(2 - 8\cos 2\phi + 8\cos^2 2\phi\Big)\frac{1+\cos 2\phi}{2} - 1\\ &= 4\cos^2 2\phi\cos 2\phi - 3\cos 2\phi\\ &= 4\frac{1+\cos 4\phi}{2}\cos 2\phi - 3\cos 2\phi\\ &= 2\cos 4\phi\cos 2\phi - \cos 2\phi.\end{aligned} \tag{B.9}$$

Setting $x = 4\phi$ and $y = 2\phi$ in Eq. (B.8) yields:

$$\cos 4\phi \cos 2\phi = \frac{\cos\Big(2\phi\Big)\cos\Big(6\phi\Big)}{2},$$

which by insertion into Eq. (B.9) results in:

$$Y = \cos 6\phi.$$

Hence the equality in Eq. (B.6) is proven.

Additional Blueprints

C

This appendix contains drawings from SolidWorks not presented in Cha. 7.

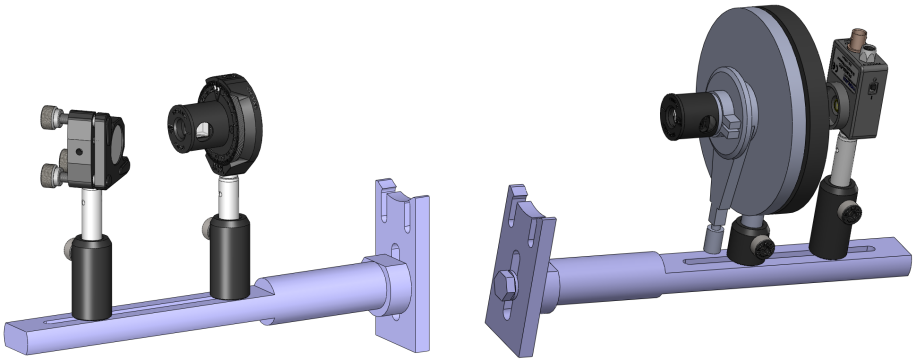

(a) A mirror in the end is used to direct the light through the first polarizer and into the chamber.

(b) After a reflection at the sample the light exits and passed the second polarizer before striking the detector.

Figure C.1: The holders are designed to fit CF40 window flanges and thereby provide the possibility of moving the optical components without a complete realignment. This is a major advantage in a three window configuration. Additionally they do not rely on the optical path to be horizontal.

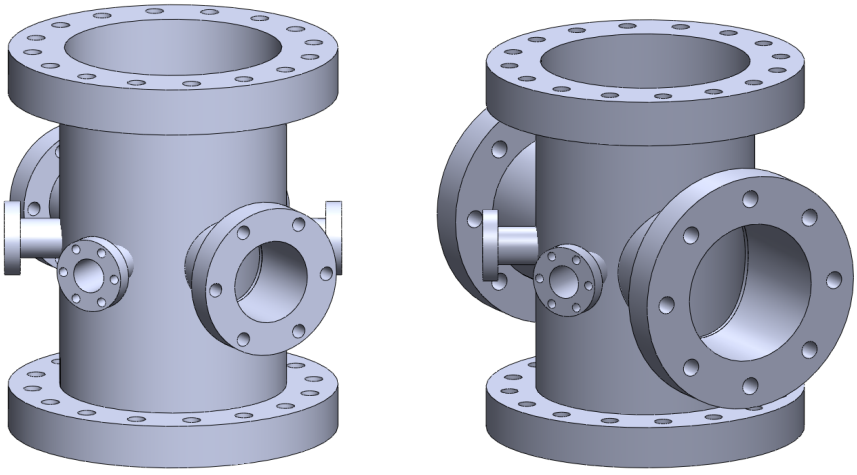

(a) CF40 flanges easily fit the central piece, but the inner diameter of the socket is limited to app. 35*mm*.

(b) CF63 flanges are found to be too large to fit next to the window flanges.

Figure C.2: The central part of the setup presented in Sec. 7.2.2 illustrated with different sizes of the flanges used for movable sockets for the magnet poles.

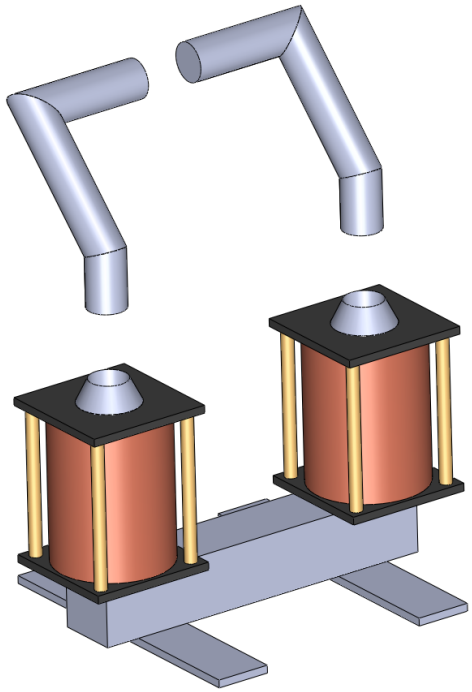

Figure C.3: An electromagnet based on the coils described in Cha. 6. The magnet is designed to stand on the main table of the setup and the poles fit into the sockets of the SMOKE chamber in Figure 7.3. The core is made separable to ease the handling and fit the poles into the sockets.

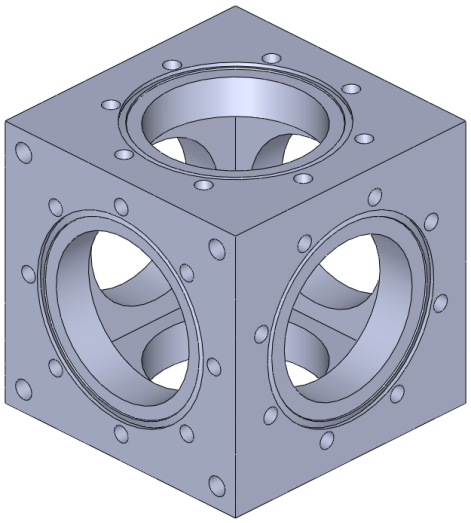

Figure C.4: The CF63 cube which is used join the SMOKE setup with the existing vacuum chamber. In addition to the tappered holes for the six flanges an additional four holes are made in the corners of one side to provide better mounting options. The inner diameter in one direction is expanded to ensure a cryostat is unable to crash into the side of the cube.

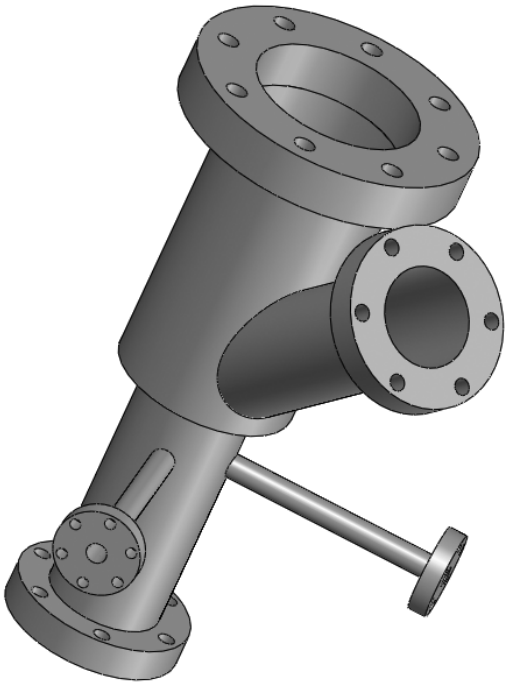

Figure C.5: The first edition of the SMOKE chamber in the final design. The chamber requires in the given setup a manipulator with a range of 250*mm*. The CF63 window is used for navigation of the cryostat to avoid crashing into the narrowing of the chamber, which fits between the magnet poles.

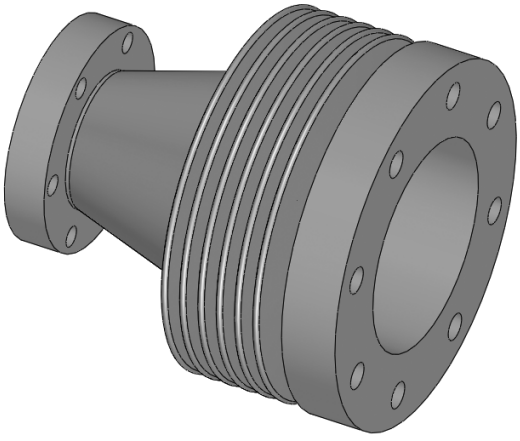

Figure C.6: The flexible coupling in the Figure is used to prevent strain on the flanges. It also provides the needed spacing between the preparation chamber and the electromagnet, and additionally it is used as an adapter between the CF40 flange on the preparation chamber and the CF63 on the cube.

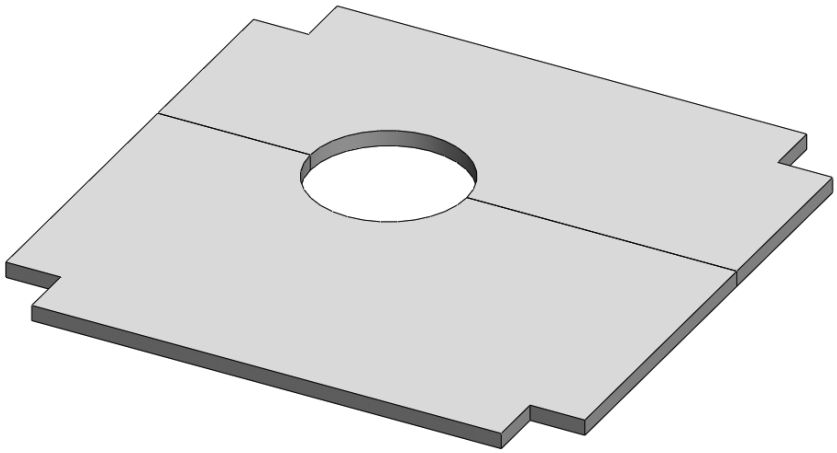

Figure C.7: A hole is cut in the *Al* plate used to support the magnet to give access to the window in the bottom of the SMOKE chamber. The plate is cut into two to allow for it to be assembled around the chamber.

C.1 Schematics for the Quadrupole Electromagnet

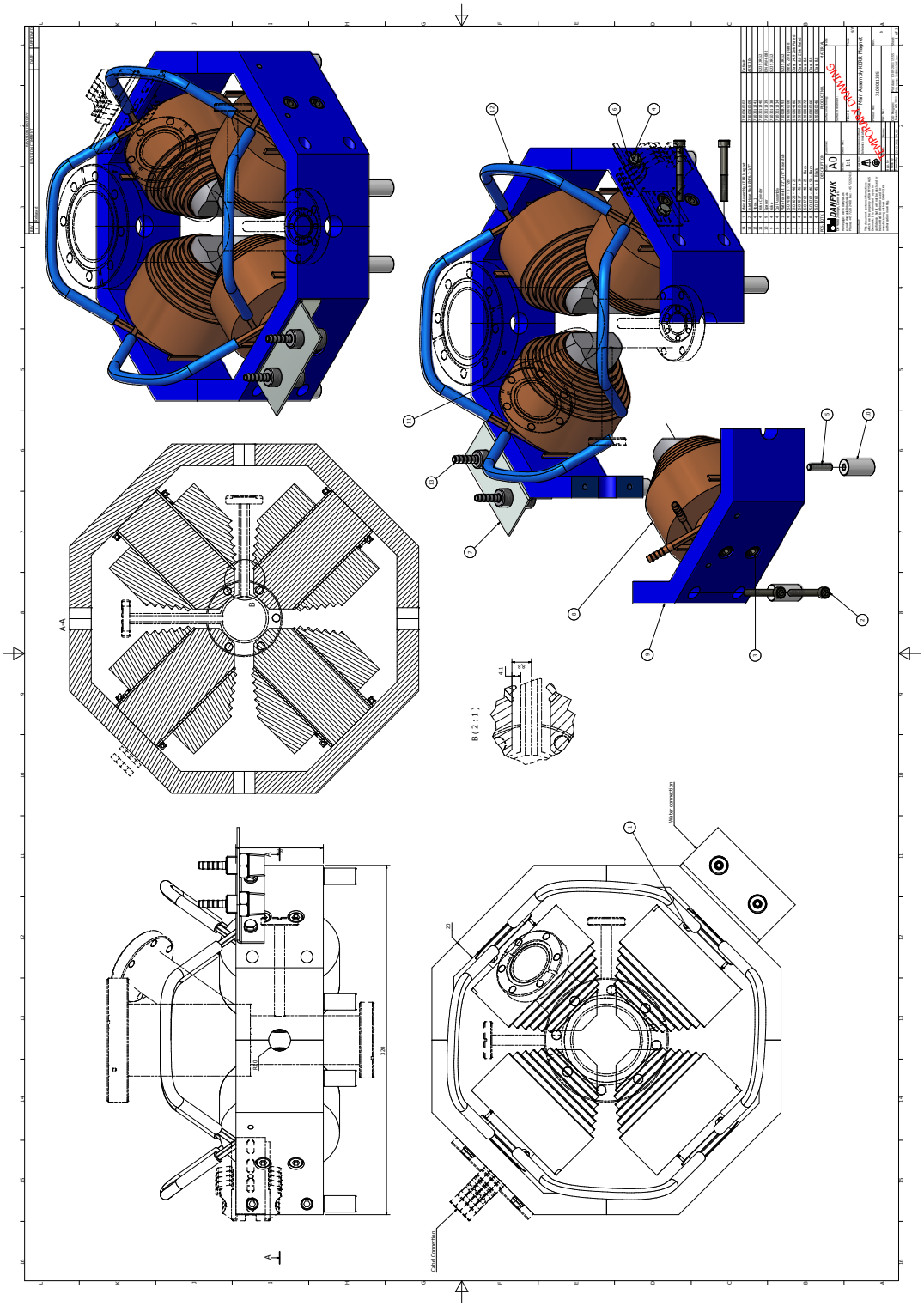

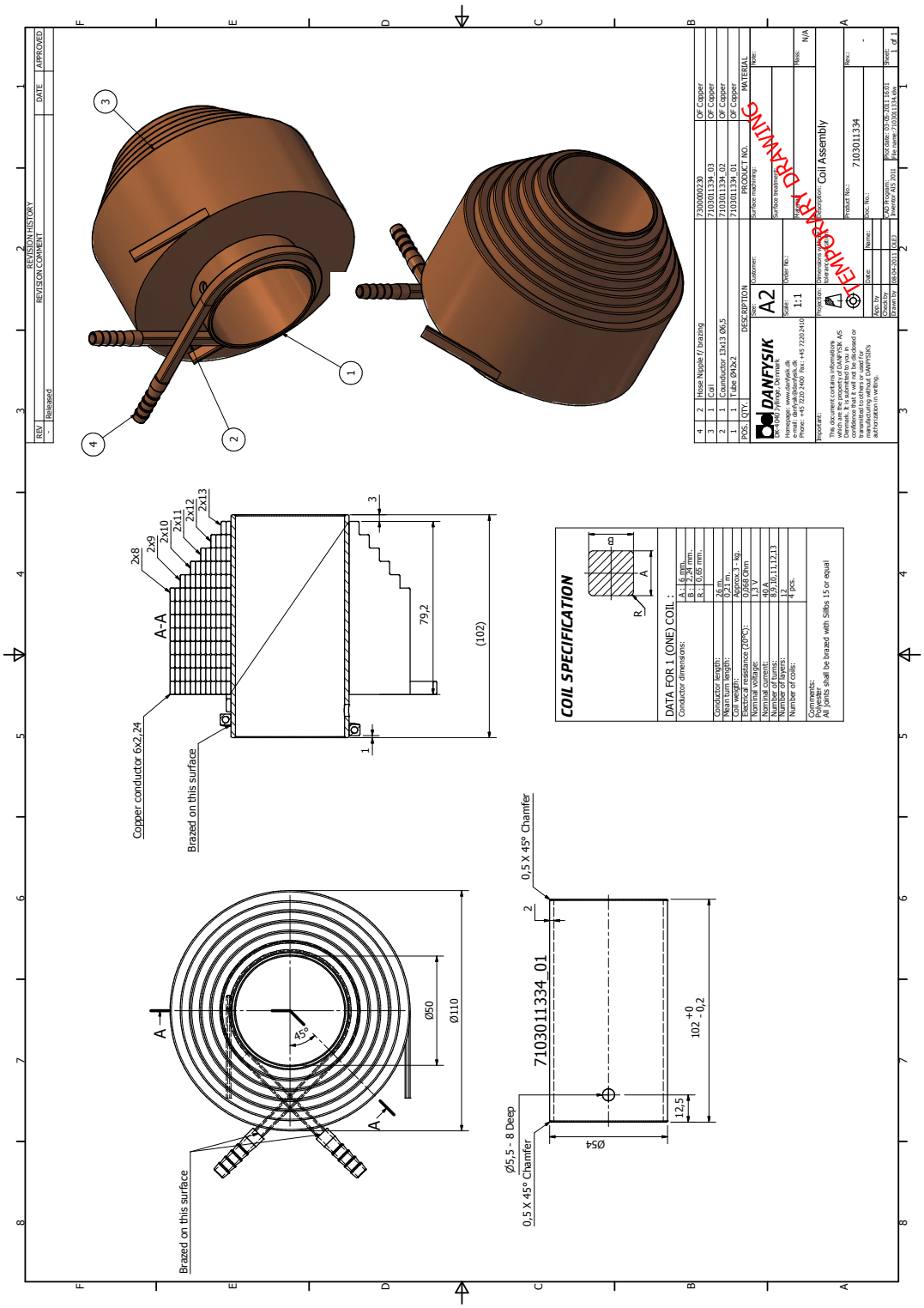
TEMPORARY DRAWING
DANFYSIK
Coil Assembly
7103011334
A2
COIL SPECIFICATION
DATA FOR 1 (ONE) COIL :
Copper conductor 6x2,24
Brazed on this surface
7103011334_01
0,5 X 45° Chamfer
Ø5,5 - 8 Deep
Ø50
Ø110
Ø54
102 +0 -0,2
12,5
79,2
(102)
45°

COMSOL Multiphysics D

This appendix includes a description of the program called COMSOL multiphysics and how it is used to simulate the magnetic fields generated by electromagnets.

D.1 Finite Element Method

Generally COMSOL Multiphysics (COMSOL) is based on the so-called finite element method (FEM). FEM is a numerical method for finding solutions to a given equation in a predefined grit. This is actually also the case in other methods than the FEM, however, in the FEM the grid is more flexible around areas of interest. [28, 423]

In order to evaluate the given equation, e.g. a partial differential equation (PDE), across and around an object of interest the geometry needs to be separated into several smaller structures. COMSOL offers several possible methods of dividing the geometry into a given structure. A concept referred to as meshing. Ordinarily meshing divides the geometry into triangular or tetrahedronic subelements if the object is either 2D or 3D respectively. However, several other possibilities exist in COMSOL, but in the present project only the before mentioned are utilized.

Naturally, the size of the elements are directly related to the precision of the simulation at hand. Accordingly the meshing should contain as small elements as possible in order to obtain the best possible result.

D.2 Applying the Physics

Before drawing the geometry, the physics needs to be specified. It needs to be decided which equation is evaluated across and around the geometry. COMSOL offers several possibilities including e.g. fluidic physics, acoustics, heat transfer, and many more. In the present only the magnetostatic behaviour of materials in the presence of DC's is considered. More precisely this means evaluating the following PDE in all the subdomains:

$$\vec{\nabla} \times \left(\frac{1}{\mu_0 \mu_r} \vec{\nabla} \times \vec{A} \right) = \vec{J}^e, \tag{D.1}$$

where $\vec{A}$ is the magnetic vector potential. The magnetic vector potential is similar to the scalar potential electric fields gives rise to, it describes the potential momentum per unit charge. Eq. (D.1) is easily derived directly from the extended Ampere's law defined in Eq. (3.31a). As all fields in the model are static the displacement

current naturally vanishes, furthermore only electrons contribute to the density of the free currents:

$$\begin{aligned}\vec{J}^e &= \vec{\nabla} \times \vec{H} \\ &= \frac{1}{\mu_0 \mu_r} \vec{\nabla} \times \vec{B} \\ &= \vec{\nabla} \times \left(\frac{1}{\mu_0 \mu_r} \vec{\nabla} \times \vec{A} \right),\end{aligned}$$

where Eq. (3.3) is introduced.

Apart from defining the PDE to be solved for the geometry all the different boundary conditions needs to be specified. Generally it follows that the complexity of the geometry and number of boundaries are connected. Luckily most boundaries are simple modelled as "*continuous*", which means that no physical properties change across the boundary. Apart from the continuous boundaries all other boundaries in the electromagnet setup are modelled as electrically insulated.

D.3 Drawing and Meshing

Sketching a given geometry in COMSOL is by all means a trivial problem. It can be constructed using COMSOL's own drawing tools or by loading schematics drawn in another program e.g. SolidWorks. The main problem of handling a geometry in COMSOL is simplifying the setup to a degree where it is solveable with a limited amount of tetrahedrons. The procedure for this goes through two steps. Initially the geometry should be simplified as much as is reasonable, e.g. by reducing the number of boundaries between components in the geometry and by reducing the size of the components the number of tetrahedrons is lowered. Secondly the meshing should be prioritized, this means that areas of interest in the geometry should be meshed using a finer mesh than other areas.

In Figure D.1 a simple 2D structure of an electromagnet is seen with a triangular mesh applied:

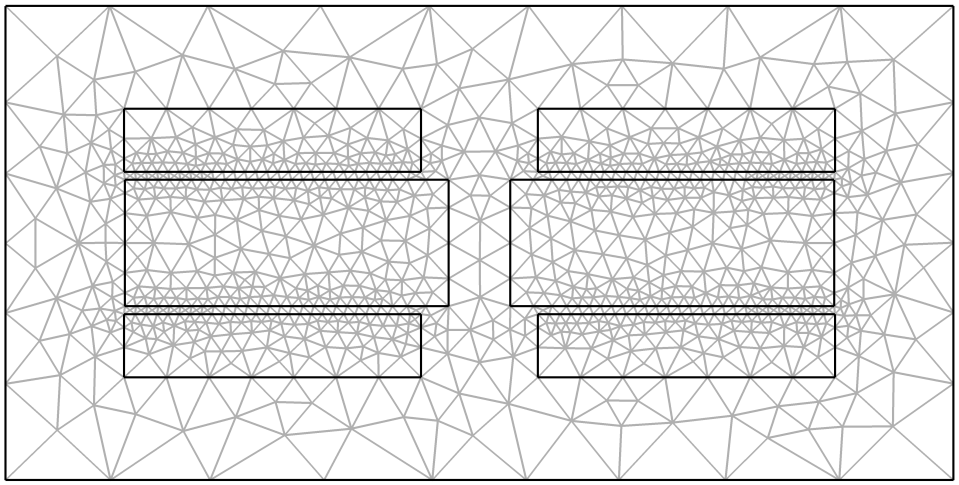

Figure D.1: Example of a 2D geometry constructed in COMSOL with a mesh of 2066 triangles applied.

The mesh illustrated in Figure D.1 consists of 2066 triangles. It is clear from the figure that around boundaries smaller triangles are needed, while in large areas without boundaries the triangle size is less crucial. An area of interest would naturally be in the center between the electromagnets and accordingly the density of triangles should be increased in this region. Furthermore it is evident from Figure D.1 that the mesh is not invariant under inversion around the x-axis even though the geometric structure is.

SMOKE on various Reference Samples

E

This appendix introduces the SMOKE results gained by measuring on various reference samples. These are included in order to validify that the Kerr response gained by measuring on ferromagnetic nanostructures is in fact generated by the structures and not the substrate. SMOKE measurements are carried out on $Si(100)$ and Sn

E.1 Si(100) Wafer

The following results were obtained by measuring on an ordinary $Si(100)$ wafer using the free air SMOKE setup presented in Sec. 6.2. These measurements were carried out in order to validate that the hysterisis loops experienced by measuring on *Fe* in Sec. 6.5 was in fact a response from the *Fe* and not the *Si* substrate. Figure E.1 display the curves for a longitudinal orientated magnetic field. The measurements in Figure E.1 were carried out at an angle $\delta = 3^\circ$ from total extinction. In the figure two sets of data is presented for incident p- and s-polarized light respectively.

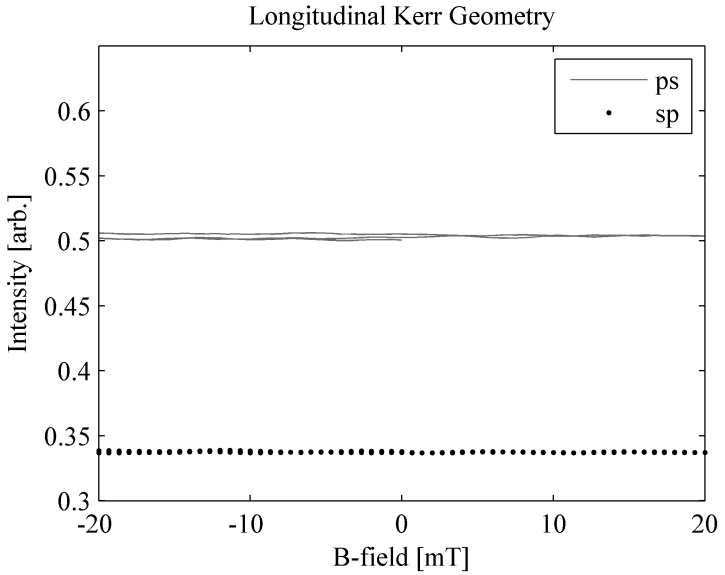

Figure E.1: Intensity of reflected light at $\delta = 3^\circ$ for incident p- and s-polarized light from a clean $Si(100)$ wafer.

The intensity curves depicted in the figure above does not display any sort of ferromagnetic response. This underlines that isolated $Si(100)$ does not give rise to a hysterisis loop through SMOKE measurements. The difference in intensity for *sp* and *ps* is simply due to the fact that the intensity of the insident light is different.

Furthermore it was investigated if $Si(100)$ displayed any response outside of the field interval depicted in the figures. In the entire field range possible, in the setup introduced in Sec. 6.2, *Si* did not display any ferromagnetic properties. This naturally is in accordance with established theory concerning the magnetic properties of *Si*.

E.2 14nm of Sn on Si(100)

In Sec. 6.5 the effect on the magneto-optic response of a ferromagnetic sample is investigated by applying a nonmagnetic capping layer. Based on this SMOKE measurements are carried out on $14nm$ of *Sn* deposited on $Si(100)$ using PVD. By comparing the results from these measurements to the results presented in Sec. 6.5 it is possible to identify the effects generated by the capping layer. In Figure E.2 the SMOKE measurements for a longitudinal Kerr geometry is presented.

The measurements were carried out at an angle $\delta = 2^\circ$ from total extinction, in the figure the data for incident p- and s-polarized light is displayed. The two

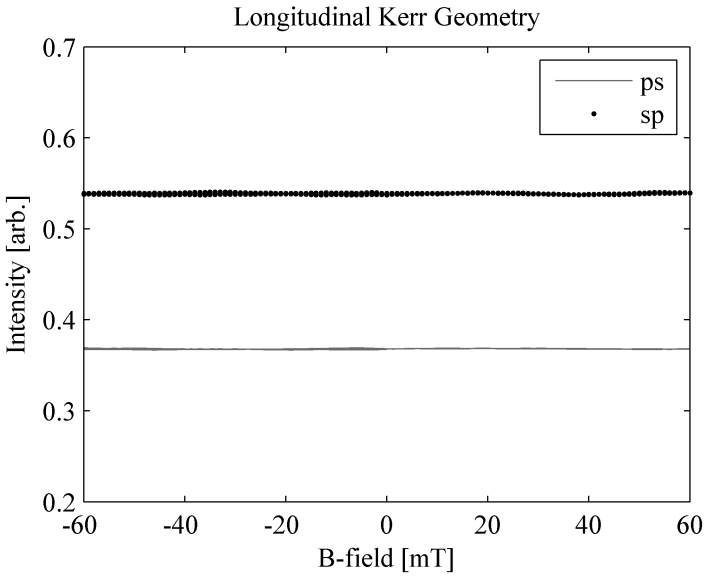

Figure E.2: Intensity of reflected light from a sample of $14nm$ of *Sn* deposited on $Si(100)$ at and angle of $\delta = 2^\circ$ from total extinction. The two sets of data represents incident p- and s-polarized light.

intensity curves in Figure E.2 does not exhibit a ferromagnetic response in the magnetic field strength interval available. Based on this it seems fair to conclude that *Sn* deposited it the way used in this project does in fact yield a nonmagnetic layer.